UNIVERSITY OF CALIFORNIA

Los Angeles

Development of Antimonide-based Energy-sensitive Radiation Detectors

A dissertation submitted in partial satisfaction of the

requirements for the degree Doctor of Philosophy

in Electrical Engineering

by

Bor-Chau Juang

2018

ABSTRACT OF THE DISSERTATION

Development of Antimonide-based Energy-sensitive Radiation Detectors

by

Bor-Chau Juang

Doctor of Philosophy in Electrical Engineering

University of California, Los Angeles, 2018

Professor Diana L. Huffaker, Chair

This dissertation is devoted to studying radiation response of the antimonide (Sb)-based detectors and investigating the energy-resolving capability of the integrated GaSb/AlAsSb device structures for X-ray and gamma-ray spectrometry. Energy-sensitive radiation detectors have been extensively employed in applications including material characterization, biomedical research, and homeland security. The unique properties of Sb-based materials could enable an increased flexibility in using the technology for versatile applications. This work attempts to take advantage of Sb-based materials and utilize the heterostructure device concept to achieve this type of radiation detectors. The device development begins with investigating the radiation response of GaSb PIN device, and the energy-sensitive detection has been demonstrated for the first time. With a measurement temperature of 140 K, the device exhibits a full-width-at-half-maximum (FWHM) of 1.238 keV and 1.789 keV at 5.9 keV and 59.5 keV, respectively. The obtained energy resolution

has been studied in detail to provide feedback on device design consideration. The heterostructure device architecture has been first approached with the GaSb/GaAs material system using the interfacial misfit (IMF) technique. While the devices show a low dark current floor at room-temperature, the potential barrier induced by the interface charges at the IMF arrays has prevented the effective collection of the carrier generated in the GaSb absorber. The lattice-matched AlAsSb alloy is then investigated as an alternative candidate to replace GaAs for the large-bandgap junction region. Digital-alloy growth of AlAsSb has been developed and gives enhanced optical and electrical characteristics in comparison to the traditional random-alloy growth. Finally, the heterostructure device for energy-sensitive radiation detection has been realized by integrating the GaSb absorber and the AlAsSb digital-alloy combined with a field-control layer to optimize the electric field profile. Well-defined X-ray and gamma-ray photopeaks are successfully obtained by the GaSb/AlAsSb devices under exposure to ^{241}Am radioactive sources. The spectroscopic characterization shows improvement in the extracted excess noise component in comparison to the PIN structure by effectively eliminating the high peak electric field and surface recombination. The minimum FWHM of 1.283 keV at 59.5 keV has been achieved, and measured energy resolution is limited by the noise from the readout electronics rather than the detector material.

This dissertation of Bor-Chau Juang is approved.

Dwight C. Streit

Benjamin S. Williams

Arion F. Chatziioannou

Diana L. Huffaker, Committee Chair

University of California, Los Angeles

2018

This dissertation is dedicated to my family.

Table of Contents

List of Figures

List of Tables

Acknowledgements

I would first like to thank my advisor, Prof. Diana L. Huffaker, for her tremendous support and guidance over the course of my Ph.D. years at UCLA. I am grateful to her for offering me numerous opportunities in research resources and mentoring particularly during difficult times of my research. I would like to express my gratitude to Prof. Arion F. Chatziioannou for sharing his expertise and precious time for discussions throughout our collaboration. I also appreciate the guidance and support from the remainder of my committee, Prof. Dwight C. Streit, and Prof. Benjamin S. Williams, as well as the help offered by their research groups.

I would like to thank Dr. Baolai Liang for providing his constant guidance and fruitful insights on many aspects of my research. I would like to thank Dr. David L. Prout for helping me understand the basics of radiation spectroscopy and giving critical comments on my publications from this work. Special thanks also go to Dr. Paul J. Simmonds, Dr. Charles J. Reyner, and Dr. Ramesh B. Laghumavarapu for teaching me the basics of MBE and sharing their invaluable experience on device fabrication and characterization. I am also very thankful for other past and present group members, Alan Farrell, Dingkun Ren, Hyunseok Kim, Mukul Debnath, and Andrew Chen for their great support as colleagues and as friends.

I am grateful to the technical support from the staff of the UCLA Nanoelectronics Research Facility and the CNSI Integrated Systems Nanofabrication Cleanroom. I would also like to thank the staff at the Office of Graduate Student Affairs, Deeona Columbia, Mandy Smith, and Ryo Arreola for always being there for students in need. I would like to acknowledge the financial support from the Defense Threat Reduction Agency (DTRA) and CNSI/HP seeding funding.

Finally, I would like to thank the selfless support from my parents and my wife for their endless love and encouragement along the way.

Vita

EDUCATION

Ph.D. candidate	University of California, Los Angeles Electrical Engineering	2012 - 2018
M.S.	University of Michigan, Ann Arbor Electrical Engineering and Computer Science	2010 - 2012
B.S.	National Chiao Tung University, Hsinchu Electronics Engineering	2005 - 2009

HONORS AND AWARDS

Doctoral Student Travel Grant, *UCLA*	2015
Best Poster Award, *Defense Threat Reduction Agency, Virginia*	2015
Research highlighted by *Semiconductor Today* (*6 April 2015)*	2015
Government Scholarships to Study Abroad, *Ministry of Education, Taiwan*	2012 - 2014
Electrical Engineering Department Fellowship, *UCLA*	2012 - 2013

PUBLICATIONS

1. B. C. Juang, B. L. Liang, D. Ren, D. L. Prout, A. F. Chatziioannou and D. L. Huffaker, "Optical characterization of AlAsSb digital alloy and random alloy on GaSb," *Crystals*, Vol. 7, pp. 313 (2017)
2. B. C. Juang, D. L. Prout, B. L. Liang, A. F. Chatziioannou and D. L. Huffaker, "Characterization of GaSb photodiode for gamma-ray detection," *Applied Physics Express*, Vol. 9, pp. 086401 (2016)
3. B. C. Juang, D. L. Prout, B. L. Liang, A. F. Chatziioannou and D. L. Huffaker, "GaSb-based photon counting gamma-ray detectors," *Device Research Conference (DRC), IEEE* (2016)
4. B. C. Juang, R. B. Laghumavarapu, P. J. Simmonds, A. Lin, B. L. Liang, and D. L. Huffaker, "GaSb thermophotovoltaic cells grown on GaAs by molecular beam epitaxy using interfacial misfit arrays," *Applied Physics Letters*, Vol. 106, pp. 111101 (2015)
5. G. T. Nelson, B. C. Juang, M. A. Slocum, Z. S. Bittner, R. B. Laghumavarapu, D. L. Huffaker, S. M. Hubbard, "GaSb solar cells grown on GaAs using interfacial misfit arrays for use in the III-Sb multi-junction cell," *Applied Physics Letters,* Vol. 111, pp. 231104 (2017)
6. A. C. Scofield, A. I. Hudson, B. L. Liang, B. C. Juang, D. L. Huffaker, W. T. Lotshaw, "Modeling and spectroscopy of carrier relaxation in semiconductor optoelectronics", *Proc. SPIE 10193, Ultrafast Bandgap Photonics II*, 101930C (2017)
7. Y. J. Ma, Y. G. Zhang, Y. Gu, X. Y. Chen, P. Wang, B. C. Juang, A. Farrell, B. L. Liang,

D. L Huffaker, Y. H. Shi, W. Y. Ji, B. Du, S. P. Xi, H. J. Tang, J. X. Fang, "Enhanced Carrier Multiplication in InAs Quantum Dots for Bulk Avalanche Photodetector Applications," *Advanced Optical Materials*, Vol. 5, pp. 1601023 (2017)

8. Y. J. Ma, Y. G. Zhang, Y. Gu, S. P. Xi, X. Y. Chen, B. L. Liang, B. C. Juang, D. L Huffaker, B. Du, X. M. Shao, J. X. Fang, "Behaviors of beryllium compensation doping in InGaAsP grown by gas source molecular beam epitaxy," *AIP Advances*, Vol. 7, pp. 075117 (2017)
9. G. Wang, B. L. Liang, B. C. Juang, A. Das, M. C. Debnath, D. L. Huffaker, Y. I. Mazur, M. E. Ware, and G. J. Salamo, "Comparative study of photoluminescence from $In_{0.3}Ga_{0.7}As$/GaAs surface and buried quantum dots," *Nanotechnology*, Vol. 27, pp. 465701 (2016)
10. H. M. Ji, B. L. Liang, P. J. Simmonds, B. C. Juang, T. Yang, R. J. Young, and D. L. Huffaker, "Hybrid type-I InAs/GaAs and type-II GaSb/GaAs quantum dot structure with enhanced photoluminescence," *Applied Physics Letters*, Vol. 106, pp. 103104 (2015)
11. S. J. Kim*, B.-C. Juang*, W. Wang, J. R. Jokisaari, C.-Y. Chen, J. D. Phillips, and X. Pan, "Evolution of Self-assembled Type-II ZnTe/ZnSe Nanostructures: Structural and Electronic Properties," *Journal of Applied Physics*, Vol. 105, pp. 093524 (2012) (*co-first author)

CONFERENCE PRESENTATIONS

1. B. C. Juang, D. L. Prout, B. L. Liang, A. F. Chatziioannou and D. L. Huffaker, "GaSb-based photon counting gamma-ray detectors," *IEEE Device Research Conference (DRC)*, Newark, Delaware (2016)
2. B. C. Juang, D. L. Prout, B. L. Liang, A. F. Chatziioannou and D. L. Huffaker, "Towards a High-Z Room Temperature GaSb/GaAs APD - Investigation of the Gamma-Ray Response of GaSb," *IEEE Nuclear Science Symposium and Medical Imaging Conference (NSS/MIC)*, Strasbourg, France (2016)
3. B. C. Juang, R. B. Laghumavarapu, P. J. Simmonds, A. Lin, B. L. Liang, and D. L. Huffaker, "Towards Low Cost Thermophotovoltaics: Growth of III-Sb Cells on GaAs Using Interfacial Misfit Arrays," *International Conference on Molecular Beam Epitaxy (ICMBE)*, Flagstaff, Arizona (2014)
4. B.-C. Juang, W. M. Wang, C.-Y. Chen, S. J. Kim, X. Pan, and J. D. Phillips, "Photoluminescence and Thermal Carrier Activation in Type-II ZnTe/ZnSe Quantum Dots," *Electronic Materials Conference (EMC)*, Santa Barbara, California (2011)

1. Introduction

Energy-sensitive radiation detectors are critical components for a wide range of technologies developed based on the interactions between various X-ray and gamma-ray photons and matter. The ionization capability of those high-energy radiations can be utilized to provide powerful tools used in the fields of material science, biomedicine research, clinical imaging, and radiological security (Fig. 1-1). The energies used in the vast majority of these applications range from the 1 keV to 200 keV. The primary role of energy-sensitive radiation detectors is to discriminate individual X-ray and gamma-ray by energy, and this unique capability provides an extra degree of freedom to utilize the information for different applications. As a result, the radiation absorption efficiency and the energy-resolving power of the detector system are of high importance to achieving the desired spectroscopic performance and are mainly determined by the choice of detector material, device architecture, and the noise performance of readout electronics.

Figure 1-1 Examples of applications utilizing energy-sensitive radiation detectors. (Reference: (Left) https://www.army.mil/e2/-images/2009/11/02/54867/; (right) https://med.nyu.edu/radiology/about-nyulmc-radiology/subspecialty-sections/nuclear-section).

Radiation detectors based on Si and Ge have been the work-horse in applications due to the maturity in their fabrication technologies and good carrier transport properties. However, they have been showing restricted performances in various applications due to their intrinsic material limitations such as relatively poor absorption efficiency to high-energy radiations and large dark current without deep cryogenic cooling. Cd(Zn)Te is another promising material candidate which provides a high absorption efficiency and the capability of room-temperature operation. However, it converts a relatively small number of electron-hole pairs per photon, which degrades the charge generation statistics. In addition, challenges remain in the uniform crystal growth, hole-tailing effect, and temporal instability that hinder widespread application. Finding a single detector material that fulfills all the desired properties and complicated trade-offs is difficult, and the investigation of other underexplored materials has long been an ongoing effort in the radiation detector community.

The focus of this dissertation is to explore and develop a new device concept using Sb-based semiconductors that have favorable material properties to achieve the high spectroscopic performance energy-sensitive detectors for gamma-rays. In comparison to conventional device configurations, i.e., PIN structure using single substances, the proposed design relies on the integration of two distinct materials for the decoupled stages in single device architecture. The absorption region will employ GaSb to offer desired radiation detection properties (i.e. high absorption efficiency, good charge generation statistics, high carrier mobilities, etc.), and the junction region is comprised of large-bandgap materials that are suited to accommodate high electric field for a reduced dark current floor. An enhanced signal strength with suppressed dark current suggests an improved energy resolution. By decoupling the absorption and the junction stages of the device structure using different materials, the approach allows us to exploit the

relative benefits of each and enables a path for flexible device design.

This dissertation begins with an overview of the background theory. Chapter 2 gives a brief introduction of the photoelectric interaction between radiation and matter, which is the primary charge generation mechanism utilized in this device research. Three main types of energy-sensitive radiation detectors are discussed along with their pros and cons in terms of intrinsic material properties and limitations. General device properties and the basic device performance metrics are also discussed. Chapter 3 introduces the evaluation of GaSb as a potential detector material for X-ray and gamma-ray spectrometry. The GaSb PIN devices are characterized to understand the electrical and optical properties, and the experimental data are compared with the device simulations. The X-ray and gamma-ray energy spectra generated by the GaSb device are demonstrated for the first time. The spectroscopic performance as well as noise characteristics are studied and discussed. In chapter 4, the potential of integrating GaSb absorber and GaAs junction region using the IMF technique to implement the proposed device architecture is investigated. The electrical properties and the radiation response of the integrated GaSb/GaAs devices are characterized. The results indicated a high degree of incomplete charge collection, likely due to the potential barriers induced by the interface charge at the IMF arrays. The lessons learned from this study lead to the next generation of material and device optimization using an alternative material system. Chapter 5 presents the material development of AlAsSb alloy as an alternative large-bandgap material to replace GaAs for the junction region. The material quality of AlAsSb grown by using digital-alloy and random-alloy methods has been evaluated. In addition, the electrical properties and the radiation response of AlAsSb devices are investigated. In Chapter 6, the proof-of-concept energy-sensitive radiation detectors using integrated GaSb/AlAsSb device structure are demonstrated. The device characteristics including electrical properties, temporal

response, and spectroscopic performance are presented. The improved energy resolution and the associated noise analysis are discussed. Finally, Chapter 7 concludes the work on the development of Sb-based energy-sensitive radiation detectors and provide the suggestions for future research directions.

2. Background of radiation detection

2.1 Detecting radiation

2.1.1 Interaction of radiation with matter

X-rays and gamma-rays are high-energy electromagnetic radiations that can be released during radioactive decays from unstable atomic nuclei. Despite a variety of interactions occur when X-ray or gamma-ray photons are passing through matters, three types of interactions are the most dominant, including the photoelectric effect, Compton scattering, and pair production. The probability of each interaction to occur depends on the photon energy and the material properties, as shown in Fig. 2-1[1]. Pair production is the process that the photon energy is converted into an electron-positron pair and usually dominates while the photon energy is in the MeV range. Since the rest mass energy of an electron is 0.511 MeV, the threshold for electron-positron pair production to become energetically possible is about 1.02 MeV[2]. As a result, the process is generally not important for studies involving X-rays and low-energy gamma-rays. In Compton scattering, only a portion of the photon energy is transferred to an electron through collision, i.e., inelastic scattering. The photon is deflected by an angle that determines the amount of transferred energy. Since all angles are possible, the Compton scattering events usually produce electrons with a wide range of energies, from zero to a fraction of the photon energy. In contrast, the photoelectric effect requires the incoming photon to transfer all of its energy to an electron, which makes it highly preferred for the X-ray and gamma-ray detectors used in spectroscopy.

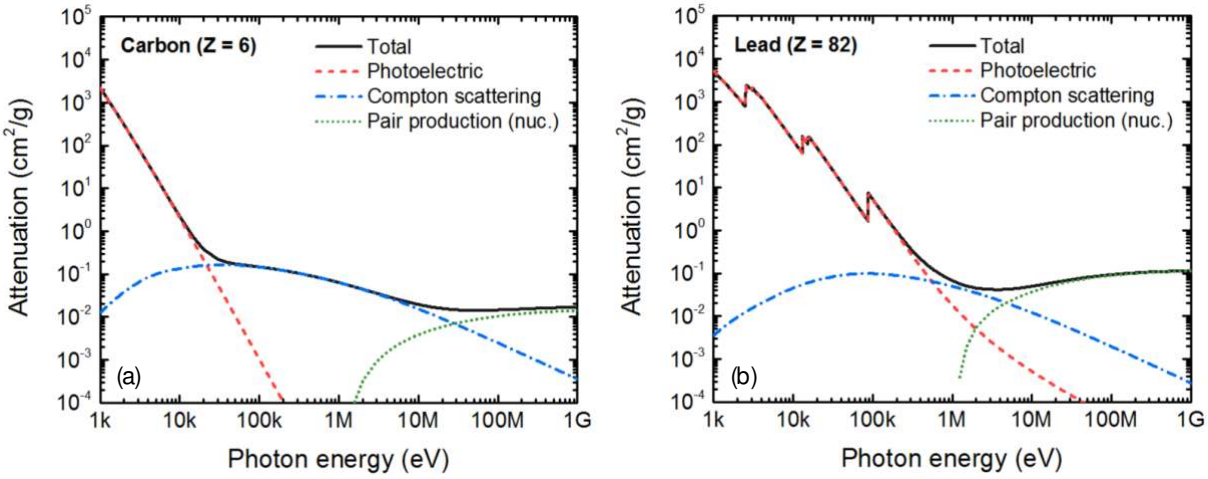

Figure 2-1 Mass attenuation coefficient of different interactions as a function of photon energy for (a) carbon and (b) lead.

2.1.2 Photoelectric effect

When a photoelectric event takes place, a bound electron from the inner atomic shell completely absorbs the incident photon energy and will be ejected with a kinetic energy of $h\upsilon - E_b$, where $h\upsilon$ is the energy of the incident photon, and E_b is the binding energy of the bound electron. Once the energetic electron is ejected (which becomes a photoelectron), it starts to undergo relaxation by ionizing the surrounding electrons. The total number of generated charges carries the energy information of the incident photon. The photoelectric effect is predominant for X-rays and gamma-rays of relatively low energies and decreases rapidly with increasing photon energy. On the other hand, the probability of photoelectric events increases dramatically with atomic number (Z) of the absorbing material. The relationship between those factors and the probability of photoelectric effect can be roughly described as $\propto Z^{4-5}/h\upsilon^{3.5}$ [2]. For example, at a given photon energy, say 10 keV, the probability of a photoelectric event is 60-fold higher in lead than in carbon (Fig. 2-1).

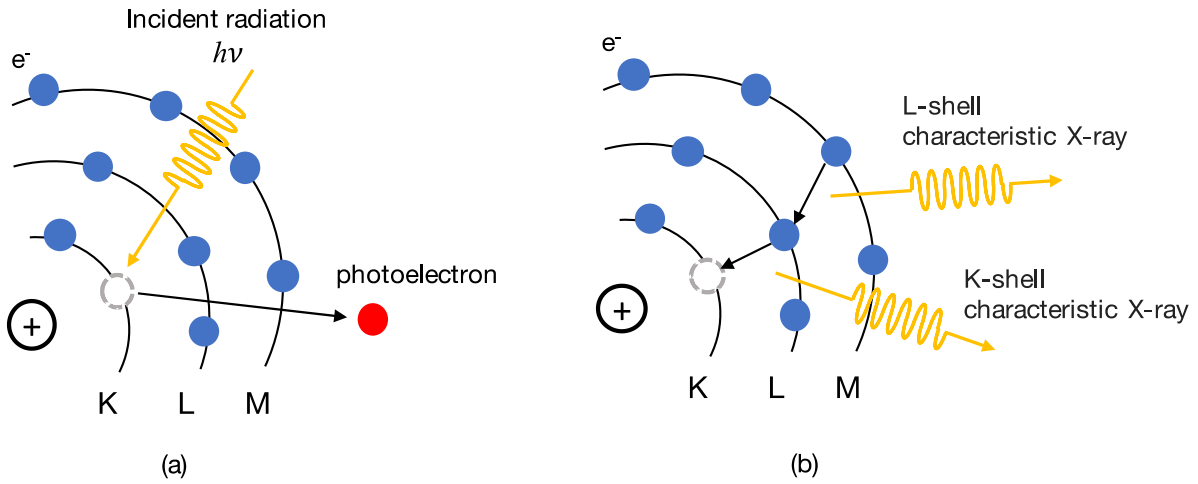

Figure 2-2 Photoelectric interaction between a photon and a bound electron, leading to (a) ejection of a photoelectron and (b) characteristic X-rays.

If the incident photon has a sufficient amount of energy to overcome the binding energy of the bound electron from the inner shell, a vacancy will be left by the ejected photoelectron (Fig. 2-2(a)). In order to return to equilibrium, the vacancy could be quickly filled by electrons from other shells of the atom, creating characteristic X-ray photons (or fluorescence) which energy is defined by the difference in binding energy between the two atomic shells (Fig. 2-2(b)). Although, in most cases, characteristic X-rays will be absorbed by subsequent photoelectric events near the original site, some secondary photons could actually escape from the surface of the detector, giving rise to an escape peak in the spectrum. The energy of the escape peaks is given by the difference between the energy of incident photon and the escaped characteristic X-ray.

2.1.3 Absorption efficiency

The linear absorption coefficient is used to describe the attenuation of the X-ray and gamma-ray photons traveling through a given thickness of the absorbing material. Assuming the original photon beam has an intensity I_0, after traveling a distance t into the material the remaining intensity can be expressed as

$$I = I_0 e^{-\mu_0 t}\,, \tag{2.1}$$

where μ_0 is the linear attenuation coefficient, i.e., the sum of probability per unit path length of possible interactions[2]. The linear attenuation coefficient is often expressed as the product of mass attenuation coefficient and the density of the absorbing material, in order to consider the variation in density of a compound or mixture of elements. The mass attenuation coefficient can be calculated from

$$\left(\frac{\mu_0}{\rho}\right)_{total} = \sum_i w_i \left(\frac{\mu_0}{\rho}\right)_i\,, \tag{2.2}$$

where w_i is the corresponding weight fraction of the element.

2.2 Radiation detectors

2.2.1 Gas-filled detectors

A gas-filled detector consists of an ionization chamber filled with gases in a cylindrical container, and the positive and negative electrodes are located along the center axis and perimeter surfaces, respectively. There is no restriction to the choice of gases since they all permit the ionization process to occur. However, the detector performance does depend on some of the gas properties, such as the average energy to produce an electron-ion pair (i.e. W-value), ion drift mobility, gas density, etc. When X-ray or gamma-ray photons passing through the gas-filled detector, there is a certain probability that the gas molecule will get ionized as long as the photon has a sufficient energy. In this case, electron-ion pairs will be created inside the ionization chamber. If an external voltage is applied to the electrodes, an electric field exists inside the gas medium will push the electrons and ions to opposite radial direction until they reach respective

electrodes and give rise to a current signal to the readout electronics. Depending on the applied voltages, the operation mode of a gas-filled detector can be categorized into the ionization chamber, proportional counter, and Geiger-Muller counter (Fig. 2-3).

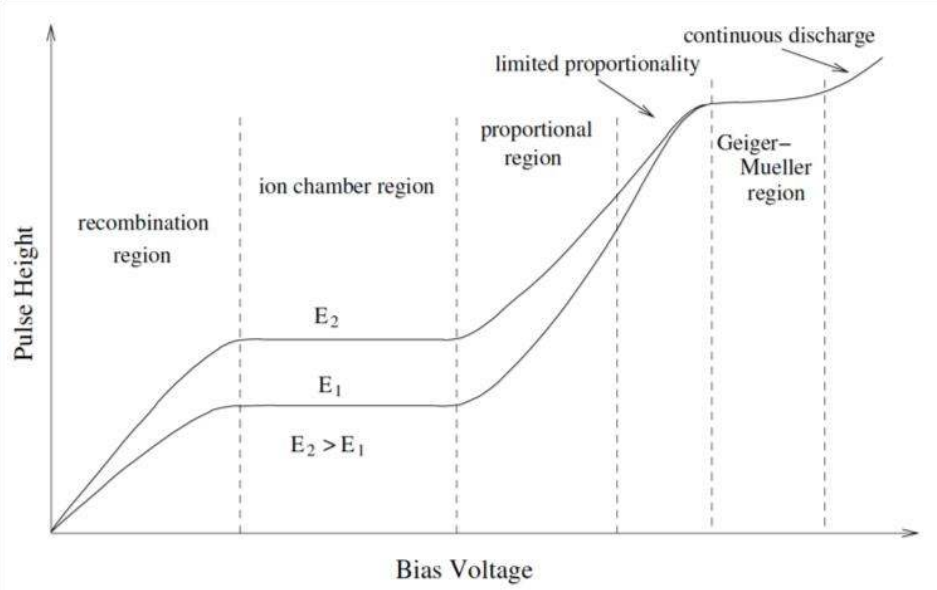

Figure 2-3 Example of different operation modes of a gas-filled detector as a function of bias voltage[3]. E_1 and E_2 indicate different energy of incident photons.

In the ionization chamber mode, the number of electron-ion pairs collected does not depend on the applied bias, indicating pulse height remains unchanged for a given photon energy. Gas-filled detectors operated under ionization chamber mode have been widely used in applications such as monitoring high-dose-rate radiation and smoke detectors. With increasing bias voltage, the electric field strength in the gas also increases and starts to introduce avalanche process to the ionized electron-ion pairs. When a gas-filled detector operates in this regime, it is considered as the proportional counter mode. The ionized electron-ion pairs experience the high electric field and gain sufficient energy to initiate subsequent ionization of secondary charges, i.e. charge multiplication, and finally resulting in greater number of electron-ion pairs. Thus, the output pulse height is amplified and can be controlled by the bias voltage.

The Geiger-Muller counter mode will take place when the bias voltage is increased further. With a substantially higher electric field, the probability of avalanche process initiated by primary electron-ion pairs becomes significant. The output pulse height no longer shows the same dependence on the bias voltage as in the proportional counter mode. The relaxation of atoms followed by avalanche event usually associated with the emission of UV photons and the emitted UV photons can liberate new electron-ion pairs and trigger more avalanche events under high electric field (Fig. 2-4). The avalanche processes will eventually saturate after the cloud of positive ions reaches a considerable size and begins to reduce the magnitude of the electric field. The collective effect of ions essentially terminates the positive feedback of avalanche processes. As a result, in Geiger-Muller counter mode, the detector will output the same pulse height regardless of the incident photon energy. The lack of energy resolving capability makes Geiger-Muller counter not suitable for applications requiring energy resolving capability. However, the significantly amplified output signal makes it an ideal candidate for the portable instrument to monitor ionizing radiations since the subsequent electronics can be greatly simplified.

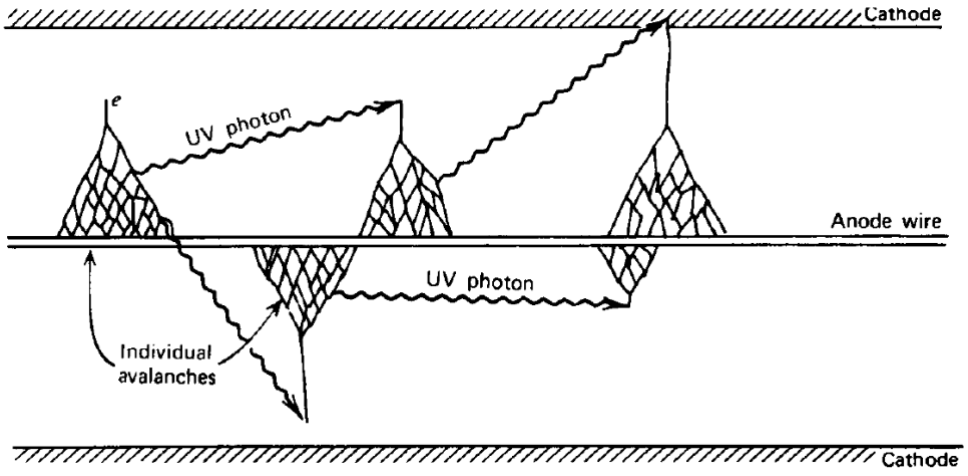

Figure 2-4 Example of a series of avalanche events caused by UV photons[2].

2.2.2 Scintillation detectors

A common method to perform gamma-ray detection is by scintillation detectors, which normally consist of a scintillation material coupled to a photomultiplier tube (PMT) or APD. The basic function of the scintillation materials is emitting optical wavelengths photons in response to the incident radiation. The radiation will excite valence electrons to populate higher electronic levels and produce luminescence during the de-excitation process. The excited states are usually determined by the activator impurities so that the emitted photon energy is in the range of near-UV or visible spectrum where the photosensors are most sensitive. The light intensity, i.e. number of emitted photons, is in proportion to the amount of energy deposited by the incident radiation. A subsequent PMT or APD is used to amplify the emission form scintillators and generate a measurable electrical signal to be processed by the readout electronics, as shown in Fig. 2-5. Commonly used scintillation materials can be divided into organic scintillators, e.g., anthracene ($C_{14}H_{10}$), p-terphenyl ($C_{18}H_{14}$), etc., and inorganic scintillators, e.g. CsI(Na), NaI(Tl), BGO

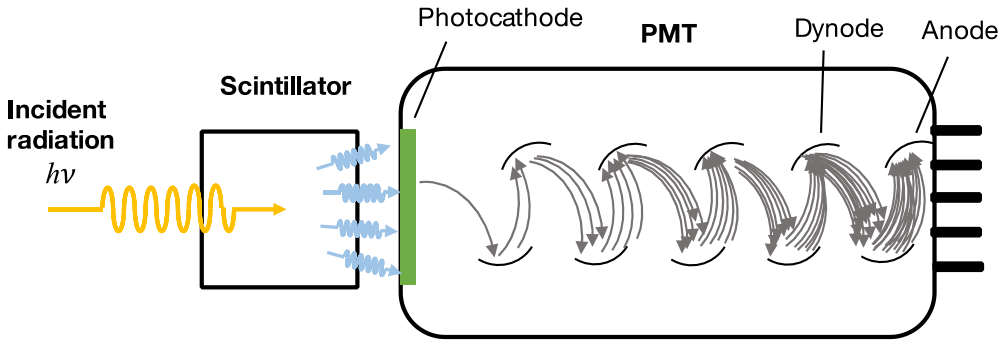

Figure 2-5 Scintillation detectors with a scintillator crystal and a PMT. Photocathode emits electrons in response to the luminescence from the scintillator, and the electrons undergo a series of avalanche multiplications via dynodes. At the end of the dynode chain is an anode to collection electrons and produces electrical signals.

(bismuth germanate), etc. The emission decay time of inorganic scintillators is much longer than that of organic materials, however, inorganic materials have higher stopping power and density that offer higher detection efficiency, especially for high-energy gamma-rays. In addition, the light yield from an inorganic scintillator is typically more near proportional to the deposited radiation energy than the typical linearity observed in organic scintillators.

The scintillation detectors offer a relatively inexpensive choice for energy-sensitive detection for nuclear and radiological applications. However, the radiation detection in scintillation detectors involves multiple inefficient steps, from the generation of optical photons to the subsequent electrical signals. One of the major limitation is the relatively poor energy resolution since the charge generation statistics is limited by Poisson process[4]. Although recent work has reported that sub-Poisson behavior from such detectors is possible[5], the relatively large energy required to create useful carriers has also placed an inherent limitation on the energy resolution.

2.2.3 Semiconductor detectors

Unlike scintillation detectors, semiconductor-based radiation detectors utilize direct detection of X-rays and gamma-rays. The incident gamma-ray energy is transferred in the detector material and creates a finite number of charges carrying the energy information. The process is analogous to that in the gas-filled detectors, except that the charge carriers are electron-hole pairs instead of electron-ion pairs. For semiconductor detectors, the amount of energy required to generate an electron-hole pair is typically 1-5 eV, much smaller than that in the gas-filled detector (about 25-35 eV) and scintillators (between 20 to 500 eV). The ability to create more charges for a given photon energy promises an enhanced signal strength. Furthermore, the charge generation in semiconductor detectors follows Fano-limited statistics, much less variation than with the

Poisson-limited statistics produced by scintillation detectors, leading to an improved spectroscopic performance (Fig.2-6).

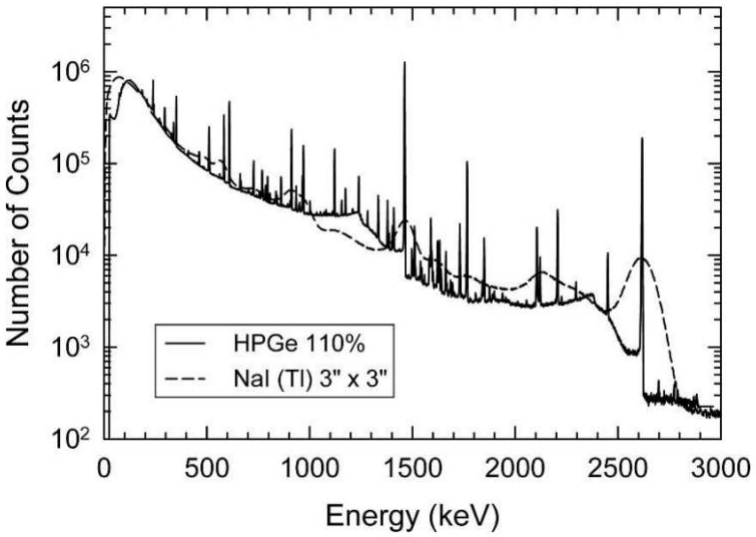

Figure 2-6 Comparison of gamma-ray spectra acquired with high energy resolution (HPGe) and low energy resolution (NaI) detectors[6].

An ideal semiconductor for high-resolution energy-sensitive gamma-ray detection shall possess high stopping power, low pair creation energy (PCE), low background noise, good carrier transport properties, and the capability of room-temperature operation. In practice, there are trade-offs between those desired properties and thus various detector materials have been evaluated for their usefulness for different applications. The stopping power of the semiconductors determined by their atomic numbers Z (absorption efficiency $\propto Z^{4-5})^2$ and crystal density, as shown in Fig. 2-7. Detectors based on Si have long been a dominant technology for soft X-ray detection (<30 keV) due to the well-developed fabrication process and compatibility with CMOS technology. Even though the development of Si-based detectors has almost approached the Fano-limited energy resolution (with cooling at -55°C)[7], its low Z (Si=14) prevents it from efficiently stopping gamma-rays. High-purity Ge (HPGe) detectors present the state-of-the-art energy resolution for gamma-

rays[2,8]. However, the device operation demands deep cooling at cryogenic temperature to reduce dark current because of its small bandgap (0.66 eV at 300 K), which has greatly limited the flexibility of applications. In addition, a large detector thickness is often required for an efficient detection due to its relatively low Z (Ge=32)[9].

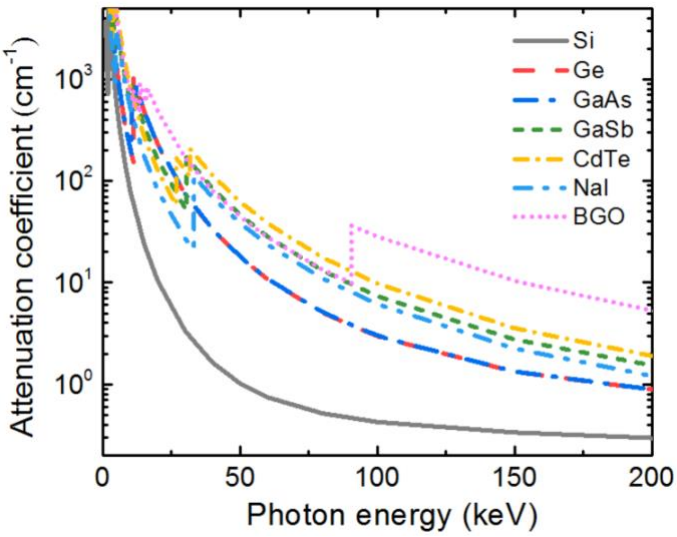

Figure 2-7 Linear attenuation coefficient for absorbing materials decomposed into different interactions against photon energy. Material data adapted from the NIST standard reference database.

Although Si and Ge still dominate the radiation detector market, many efforts have been made to develop detector materials based on compound semiconductors. Large-bandgap compound semiconductors, such as GaAs, AlGaAs, InP, and AlInP, have been intensively studied recently due to their potentials to offer near room-temperature operation[10–13]. Likewise though, their relatively low Z (Ga=31, As=33, Al=13) inevitably limits on the sensitive energy range. Another large-bandgap material Cd(Zn)Te has also been considered as a promising detector material because it has a much higher Z (Cd=48, Te=52) than other candidates. However, uniformity of crystal growth remains challenging, and its poor hole mobility (<100 $cm^2V^{-1}s^{-1}$) has been known to produce a low-energy tail degrading the measured energy resolution[14,15]. On the

other hand, small-bandgap semiconductors, such as InAs and InSb, offer high Z (In=49, Sb=51) and high carrier mobilities, providing attractive properties for detectors with high spectroscopic performance[16–18]. However, the small-bandgap materials are often associated with large dark current due to high intrinsic carrier concentration. In addition, the field-assisted process is found to have profound impact on the their dark current with increasing bias.

Atomic number Z	Absorption coefficient	Dark current	Bandgap (or PCE)	Best for…
High	Large	High	Small	Absorber
Low	Small	Low	Large	High-field junction

Table 2-1 Summary of material parameters illustrating the relative merits of a radiation detector. Desired properties are highlighted in red and unfavorable properties are highlighted in blue.

In summary, small-bandgap semiconductors are usually associated with high stopping power and small PCE, which dictates improved charge generation statistics. However, small-bandgap materials also suffer from a large dark current that compromises the anticipated performance. On the other hand, the dark current is considerably reduced as the bandgap increases, but large-bandgap materials commonly exhibit relatively poor stopping power. Table 2-1 presents some of these pros and cons of compound semiconductors, effectively illustrating the difficulty of finding a single material that fulfills all the requirements for energy-sensitive detection.

The need exists for a gamma-ray detector architecture that addresses all of these deficiencies. The research in this work attempts to explore an alternative solution to this complicated material trade-off by utilizing decoupled absorption and junction stages in a single device to achieve energy-sensitive gamma-ray detectors with high spectroscopic performance.

2.3 General properties of radiation measurement

2.3.1 Energy resolution

The X-ray and gamma-ray spectra are created based on various sizes of electronic pulse produced at the output of the detector, and the size of electronic pulse is determined by the energy deposited by the incident radiation. In the ideal case, photons with the same energy will create a fixed number of carriers and thus generate a train of pulses with identical amplitude, resulting in a photopeak with delta-like distribution in the energy spectrum. However, in practice, the photopeak widths are wider and produce a Gaussian-like distribution due to fluctuations in the measured pulse heights. Energy resolution is used to describe the ability of detectors to accurately determine the energy of the incoming radiation, and it is quantified by the ratio of the photopeak full-width-at-half-maximum (FWHM) and the corresponding photon energy (Fig. 2-8). The variation in height

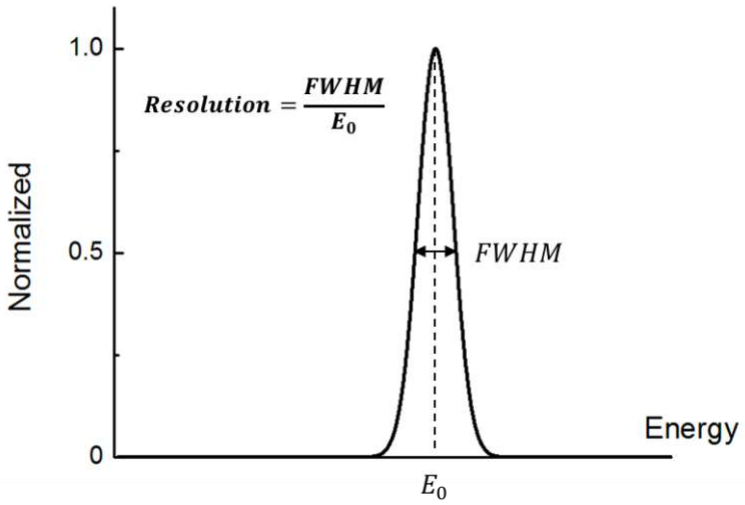

Figure 2-8 Example of a photopeak in the energy spectrum and the measurement of its energy resolution.

measured from pulse to pulse causes broadening in the photopeak and degrades the energy resolution. If the standard deviation of the Gaussian distribution is σ, its FWHM of a Gaussian peak is equal to 2.355σ. As a result, the FWHM of a photopeak can be described as

$$FWHM = 2.355 \cdot \Delta E_{rms} \,, \tag{2.3}$$

and ΔE_{rms} is the standard deviation in energy and comprised of different components

$$\Delta E_{rms} = \sqrt{\Delta E_{Fano}^2 + \Delta E_{elec}^2 + \Delta E_{ex}^2} \,, \tag{2.4}$$

where ΔE_{Fano}, ΔE_{elec}, and ΔE_{ex} are the fluctuation in energy due to Fano noise, electronic noise, and excess noise.

2.3.2 Pair creation energy

Pair creation energy (PCE) is a material dependent property that indicates the amount of average energy spent to create an electron-hole pair by X-rays or gamma-rays. In semiconductors, semi-empirical models have been used to describe the pair creation energy ε of a material based on the bandgap energy[19],

$$\varepsilon = \left(\frac{14}{5}\right) \cdot E_g + r \,, \tag{2.5}$$

where r is a free fitting parameter lies in the range between 0 to 1. The "main branch" of the model with $r = 0.606$ agrees with an extensive range of materials, as shown in Fig. 2-9. However, some of the compound semiconductors show deviation from the main branch and the model is currently unsatisfactory. Bertuccio et al. has proposed a new empirical model to fit the pair creation energy of GaAs along with Si and Ge and shows excellent agreement with the measured data[20]. Throughout the progress of developing new III-V materials as radiation detectors[21–23], the formula

has been further revised to improve accuracy. Fig. 2-10 shows the pair creation energy as a function of bandgap energy of the common group IV and group III-V materials along with the most recent empirical model,

$$\varepsilon = (1.52 \pm 0.08)E_g + (1.90 \pm 0.12)\,. \tag{2.6}$$

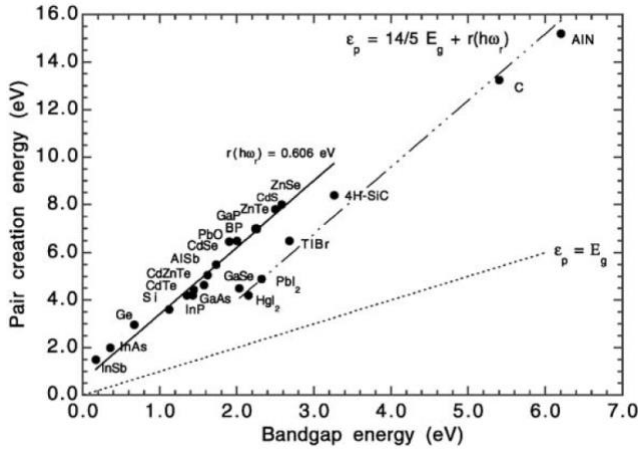

Figure 2-9 Average energy required to create an electron-hole pair as a function of semiconductor bandgap energy[9].

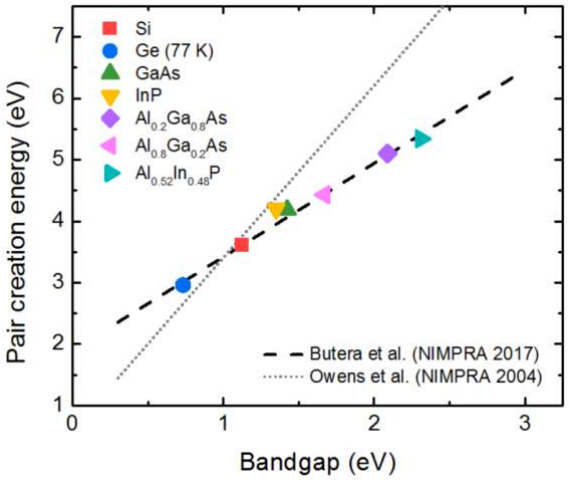

Figure 2-10 Empirical formula of pair creation energy as a function of bandgap energy based on group IV elements and III-V compounds[9,23].

2.3.3 Fano factor

The Fano factor (F) is another material dependent property that indicates the deviation in the number of electron-hole pairs generated at a given photon energy from pure Poisson statistics. For radiation absorbed in semiconductors, the majority of the photon energy is lost due to lattice vibration (i.e. phonon scattering), and only a fraction of the energy results in ionization. Thus, the statistical fluctuation in the number of electron-hole-pairs was anticipated to follow Poisson distribution due to the uncertainty of the energy loss. The Poisson distribution predicts a variance

$\sigma^2 = N$, where σ is the standard deviation and N is the total number of electron-hole-pairs produced by an incident photon

$$N = \frac{E}{\varepsilon}. \tag{2.7}$$

However, it has been found that the variance of the number of electron-hole-pairs is actually much smaller than that from the Poisson distribution, indicating the ionization events are not completely independent. The Fano factor has been introduced to characterize the difference between the experimentally observed variance and the variance of Poisson distribution[24],

$$F = \frac{measured\ variance}{expected\ variance} = \frac{measured\ variance}{E/\varepsilon}, \tag{2.8}$$

and the expected F for the most semiconductors is between 0.05-0.15. As a result, ΔE_{Fano} can be expressed as

$$\Delta E_{Fano} = \varepsilon \cdot \sqrt{\frac{FE}{\varepsilon}} = \sqrt{FE\varepsilon}\,, \tag{2.9}$$

which sets a fundamental limit to the attainable energy resolution of the detector material.

2.3.4 Electronic noise

In X-ray and gamma-ray spectroscopy, readout electronics is a crucial component to extract accurate information from the pulse signals produced by the detector. However, readout electronics also introduces additional noise during signal processing, which gives rise to baseline fluctuations that superimposes on the detected signal (Fig. 2-11). The additional fluctuation results in increased uncertainty of measured pulse height, adding an extra degree of broadening (ΔE_{elec}) to the measured photopeak in energy spectrum. The main noise sources include leakage current of the detector and the field-effect transistor (FET) in the charge-sensitive amplifier, capacitive

components at the preamplifier input, cabling of the measurement system, and intrinsic noise of the subsequent amplifiers.

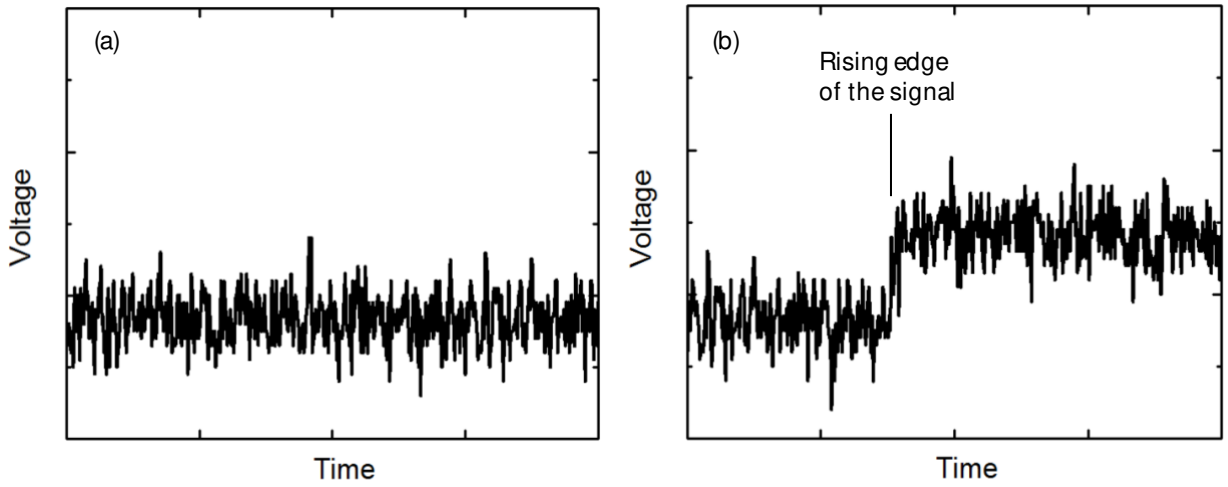

Figure 2-11 Output signal of the charge-sensitive amplifier connected to a detector. (a) Baseline fluctuation due to noise induced by readout electronics, and (b) its effect on the detected signal.

The equivalent noise charge (ENC) is a convenient way to describe the electronic noise, defined as the number of electron charges required to produce the equivalent fluctuation in pulse height, and can be expressed as

$$\Delta E_{elec} = \varepsilon \cdot ENC_{elec} \, . \tag{2.10}$$

The use of ENC analysis allows further investigation of the electronic noise in the measurement system. The sources of electronic noise can be attributed to current noise (parallel noise), voltage noise (series noise), and $1/f$ noise (or dielectric noise) that present at the vicinity of the input of the charge-sensitive amplifier. A pulse-shaping amplifier is usually connected to the output of the charge-sensitive amplifier to provide further pulse transformation to facilitate the pulse-height measurement. The shaping time constant associated with the transfer function in pulse-shaping amplifier provides a way to alter the frequency response of different electronic noise components.

By studying the ENC as a function of shaping time constant, the contribution of the abovementioned noise sources can be characterized (Fig. 2-12).

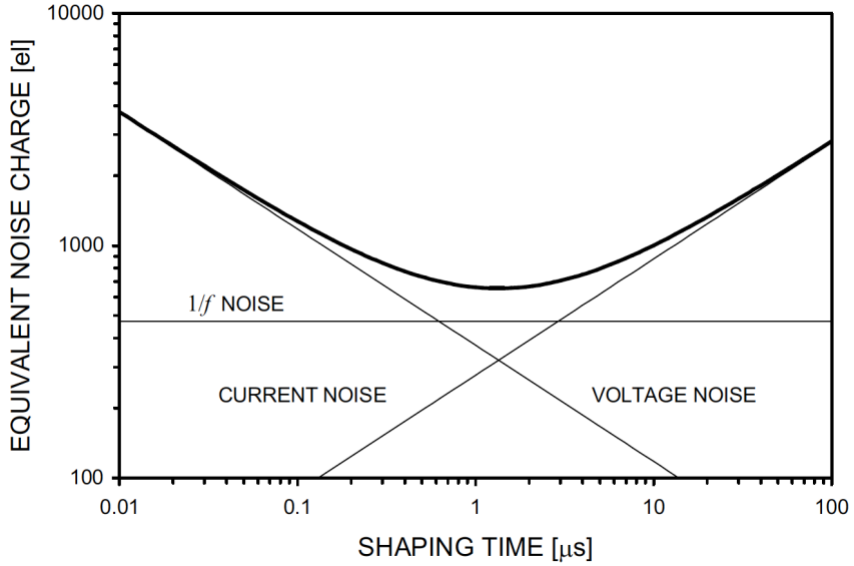

Figure 2-12 Equivalent noise charge as a function of the shaping time constant[25].

2.3.5 Excess noise

Excess noise (ΔE_{ex}) is often used to account for the excess broadening factor present in the measured photopeak FWHM in an energy spectrum. Ideally, the photopeak broadening obtained by a radiation detector can be fully described by the statistical fluctuation due to Fano noise and the electronic noise in the measurement system. For a given detector material, its spectroscopic performance will only be improved by minimizing the contribution of the electronic noise. Furthermore, since the electronic noise can be readily measured using a test signal provided by pulse generator, determination of the Fano factor of a detector material is possible provided that the pair creation energy is known. However, in practice, excess broadening is commonly observed in addition to those components resulting from Fano noise and electronic noise, especially for compound semiconductors (Fig. 2-13).

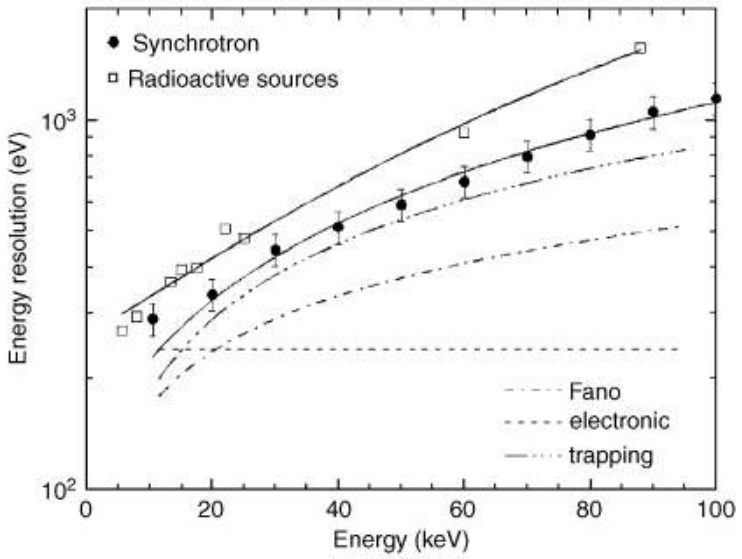

Figure 2-13 Example of a separated Fano noise, electronic noise, and trapping noise as a function of photon energy for a CdTe detector[27].

The excess noise is usually referred as trapping noise, namely the charge fluctuation is attributed to the uncertainty of carrier loss via charge trapping. When the carriers are traveling across the absorbing medium, there is a finite probability for trapping to occur at crystalline defects before they reach the respective electrodes, resulting in incomplete carrier collection. The excess charge is found to show energy dependence and often described by an empirical model[2,9,11,26],

$$\Delta E_{ex} = a_1 E^{a_2} , \tag{2.11}$$

where a_1 and a_2 are the empirical parameters derived by best fitting. If the trapping effect becomes significant, it usually appears as a spread of photopeak toward lower energy against the photopeak created by complete collection.

2.4 Reference

1. Berger Hubbell, J.H., Seltzer, S.M., Chang, J., Coursey, J.S., Sukumar, R., Zucker, D.S., and Olsen, K., M. J. XCOM: Photon Cross Section Database (version 1.5) Available: http://physics.nist.gov/xcom.

2. Knoll, G. F. *Radiation detection and measurement*. (John Wiley & Sons, 2010).

3. Ahmed, S. N. *Physics and engineering of radiation detection*. (Academic Press, 2007).

4. Derenzo, S. E., Bourret-Courshesne, E., Bizarri, G. & Canning, A. Bright and ultra-fast scintillation from a semiconductor? *Nucl. Instruments Methods Phys. Res. Sect. A Accel. Spectrometers, Detect. Assoc. Equip.* **805,** 36–40 (2016).

5. Bora, V. *et al.* Estimation of Fano factor in inorganic scintillators. *Nucl. Instruments Methods Phys. Res. Sect. A Accel. Spectrometers, Detect. Assoc. Equip.* **805,** 72–86 (2016).

6. Milbrath, B. D., Peurrung, A. J., Bliss, M. & Weber, W. J. Radiation detector materials: An overview. *J. Mater. Res.* **23,** 2561–2581 (2008).

7. Ametek. http://www.amptek.com/products/xr-100sdd-silicon-drift-detector/.

8. Luke, P. N. & Amman, M. Room-Temperature Replacement for Ge Detectors - Are We There Yet? *IEEE Trans. Nucl. Sci.* **54,** 834–842 (2007).

9. Owens, A. & Peacock, A. Compound semiconductor radiation detectors. *Nucl. Instruments Methods Phys. Res. Sect. A Accel. Spectrometers, Detect. Assoc. Equip.* **531,** 18–37 (2004).

10. Bertuccio, G., Pullia, A., Lauter, J., Forster, A. & Luth, H. Pixel X-ray detectors in epitaxial gallium arsenide with high-energy resolution capabilities (Fano factor experimental determination). *Nucl. Sci. IEEE Trans.* **44,** 1–5 (1997).

11. Barnett, A. M. Characterization of GaAs mesa photodiodes with X-ray and γ-ray photons. *Nucl. Instruments Methods Phys. Res. Sect. A Accel. Spectrometers, Detect. Assoc. Equip.* **756,** 39–44 (2014).

12. Lees, J. E. *et al.* Development of high temperature AlGaAs soft X-ray photon counting detectors. *J. Instrum.* **6,** C12007 (2011).

13. Butera, S., Lioliou, G., Krysa, A. B. & Barnett, A. M. Characterisation of $Al_{0.52}In_{0.48}P$ mesa p-i-n photodiodes for X-ray photon counting spectroscopy. *J. Appl. Phys.* **120,** 24502 (2016).

14. Takahashi, T. & Watanabe, S. Recent progress in CdTe and CdZnTe detectors. *Nucl. Sci. IEEE Trans.* **48,** 950–959 (2001).

15. Schlesinger, T. E. *et al.* Cadmium zinc telluride and its use as a nuclear radiation detector material. *Mater. Sci. Eng. R Reports* **32,** 103–189 (2001).

16. Säynätjoki, A. *et al.* InAs pixel matrix detectors fabricated by diffusion of Zn in a metal-organic vapour-phase epitaxy reactor. *Nucl. Instruments Methods Phys. Res. Sect. A Accel. Spectrometers, Detect. Assoc. Equip.* **563,** 24–26 (2006).

17. Meng, X. *et al.* InAs avalanche photodiodes as X-ray detectors. *J. Instrum.* **10,** P10030 (2015).

18. Sato, Y., Morita, Y. & Kanno, I. Performance estimation of InSb compound semiconductor detectors as a function of active area using alpha particles. *Nucl. Instruments Methods Phys. Res. Sect. A Accel. Spectrometers, Detect. Assoc. Equip.* **737,** 1–4 (2014).

19. Klein, C. A. Bandgap Dependence and Related Features of Radiation Ionization Energies in Semiconductors. *J. Appl. Phys.* **39,** 2029–2038 (1968).

20. Bertuccio, G. & Maiocchi, D. Electron-hole pair generation energy in gallium arsenide by

x and γ photons. *J. Appl. Phys.* **92,** 1248–1255 (2002).

21. Barnett, A. M., Lees, J. E., Bassford, D. J. & Ng, J. S. A varied shaping time noise analysis of $Al_{0.8}Ga_{0.2}As$ and GaAs soft X-ray photodiodes coupled to a low-noise charge sensitive preamplifier. *Nucl. Instruments Methods Phys. Res. Sect. A Accel. Spectrometers, Detect. Assoc. Equip.* **673,** 10–15 (2012).

22. Whitaker, M. D. C., Butera, S., Lioliou, G. & Barnett, A. M. Temperature dependence of $Al_{0.2}Ga_{0.8}As$ X-ray photodiodes for X-ray spectroscopy. *J. Appl. Phys.* **122,** 34501 (2017).

23. Butera, S., Lioliou, G., Krysa, A. B. & Barnett, A. M. Measurement of the electron–hole pair creation energy in $Al_{0.52}In_{0.48}P$ using X-ray radiation. *Nucl. Instruments Methods Phys. Res. Sect. A Accel. Spectrometers, Detect. Assoc. Equip.* (2017). doi:https://doi.org/10.1016/j.nima.2017.10.027

24. Fano, U. Ionization yield of radiations. II. The fluctuations of the number of ions. *Phys. Rev.* **72,** 26 (1947).

25. Spieler, H. *Semiconductor detector systems*. (Oxford University Press, 2008).

26. Zakharchenko, A. A. *et al.* Transport properties and spectrometric performances of CdZnTe gamma-ray detectors. in **8507,** 85071I–85071I–7 (2012).

27. Owens, A. *et al.* Hard X- and γ-ray measurements with a 3×3×2 mm^3 CdZnTe detector. *Nucl. Instruments Methods Phys. Res. Sect. A Accel. Spectrometers, Detect. Assoc. Equip.* **563,** 268–273 (2006).

3. GaSb PIN devices

3.1 Background

The III-Sb compound semiconductors offer a great flexibility in material and device engineering, due to a wide range of available bandgaps, band offsets, and high carrier mobility. Devices based on a variety of III-Sb material combinations have produced promising candidates for applications spanning from military to civil sectors, including high-speed electronic devices (FETs, HEMTs, and HBTs)[1–3], near infrared (NIR) laser sources[4,5] to mid- and long-wave IR photodetectors as well as focal plane arrays (FPAs)[6–9]. In addition, Sb-based materials possess a great potential to offer high spectroscopic performance for radiation detection. However, there has only been limited effort studying their X-ray and gamma-ray response[10,11].

GaSb, as one of the popular III-Sb materials for optoelectronics[12–16], has a high Z and high crystal density (5.61 g/cm^3) that are favorable for efficient radiation absorption for the energies of interest (1-200 keV)[17,18]. Its relatively small bandgap predicts a low PCE that can be beneficial to produce improved charge generation statistics for an enhanced spectroscopic resolution. Furthermore, the high carrier mobilities (approximately 3300 cm^{2}V^{-1}s^{-1} for electrons and 1000 cm^{2}V^{-1}s^{-1} for holes) and the long intrinsic carrier lifetime (~500 ns) reported recently[19] provide a great advantage in carrier transport and efficient collection. The mature growth and fabrication technologies of III-V materials in comparison to other detector material candidates, such as Cd(Zn)Te and HgI_2, make GaSb a promising platform for developing energy-sensitive X-ray and gamma-ray detectors. However, the small bandgap of GaSb also inevitably leads to large dark current, primarily due to thermal generation and field-assisted tunneling current components. As

a result, moderate cooling and proper biasing would be required during device operation.

In this chapter, we present electrical and optical characterizations of the GaSb PIN devices. The analysis of dark current mechanisms and carrier transport properties were studied for future device design consideration. X-ray and gamma-ray energy spectra obtained by the GaSb PIN device using ^{55}Fe and ^{241}Am radioactive sources are demonstrated. In addition, the noise characteristics and the material parameters are experimentally extracted and analyzed.

3.2 Device fabrication

3.2.1 Device design and growth

The GaSb PIN device structure consisting of a 2 μm i-region was grown by molecular beam epitaxy (MBE) on an un-intentionally doped GaSb (001) substrate. The use of a relatively thin absorption region is intended for device research purpose. After removing the native oxide at 560°C, the device layers were grown at 500°C with a Sb/Ga beam equivalent pressure (BEP) ratio of 6. Te and Be were used as the n-type and p-type dopants for GaSb, respectively. Compensational doping by Te was used to minimize the background doping level in the i-region since the intrinsic acceptor concentration of GaSb is typically p-type at 7×10^{16} cm^{-3}. The reduced i-region doping level also helps lower the contribution of device capacitance in electronic noise that occurs in the radiation measurement. The minimum achieved background doping level is about 3×10^{16} cm^{-3}, as measured via room-temperature Hall effect measurement.

3.2.2 Surface passivation

The device wafer was fabricated into circular mesas, as shown in Fig. 3-1, with various sizes using standard photolithographic techniques, and the fabrication details can be found in

Appendix A. The sidewall surface of device mesas was exposed during multiple fabrication steps, indicating contaminations and oxidations could take place and cause undesired paths for leakage current. To reduce the surface leakage current[20], the mesa sidewall surfaces were polished by HCl-based wet-etchant after device fabrication, followed by $(NH_4)_2S$ passivation. The representative dark current-voltage (I-V) curves are shown in Fig. 3-2(a), suggesting a significant improvement after surface passivation.

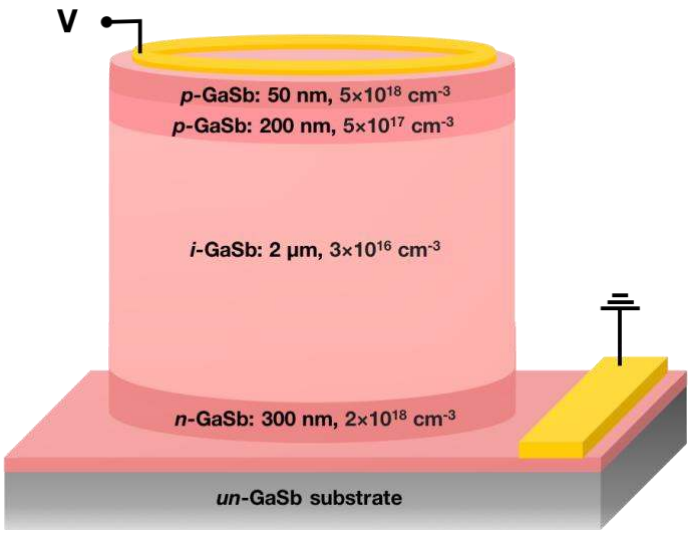

Figure 3-1 GaSb PIN device structure with a 2-μm-thick absorption region.

The effect of $(NH_4)_2S$ passivation can be evaluated using the inverse of the zero-bias dynamic resistance-area product $1/(R_0A)$ as a function of perimeter-to-area ratio P/A among devices with various active areas, given by

$$\frac{1}{R_0A} = \left(\frac{1}{R_0A}\right)_{bulk} + \left(\frac{1}{r_{surf}}\right)\frac{P}{A}, \tag{3.1}$$

where r_{surf} represents the resistivity of surface shunt paths. A small value of r_{surf} indicates a strong dependence of the leakage current on the surface effects, as shown in Fig. 3-2(b), and the desired r_{surf} value should be as large as possible. The $1/(R_0A)$ values of the as-fabricated devices

were found to have a strong linear dependence to the P/A with a r_{surf} of 39.1 Ω•cm. After $(NH_4)_2S$ treatment, the r_{surf} value has been improved by more than three orders of magnitude to 41.4 kΩ•cm, suggesting an effective elimination of the surface leakage paths.

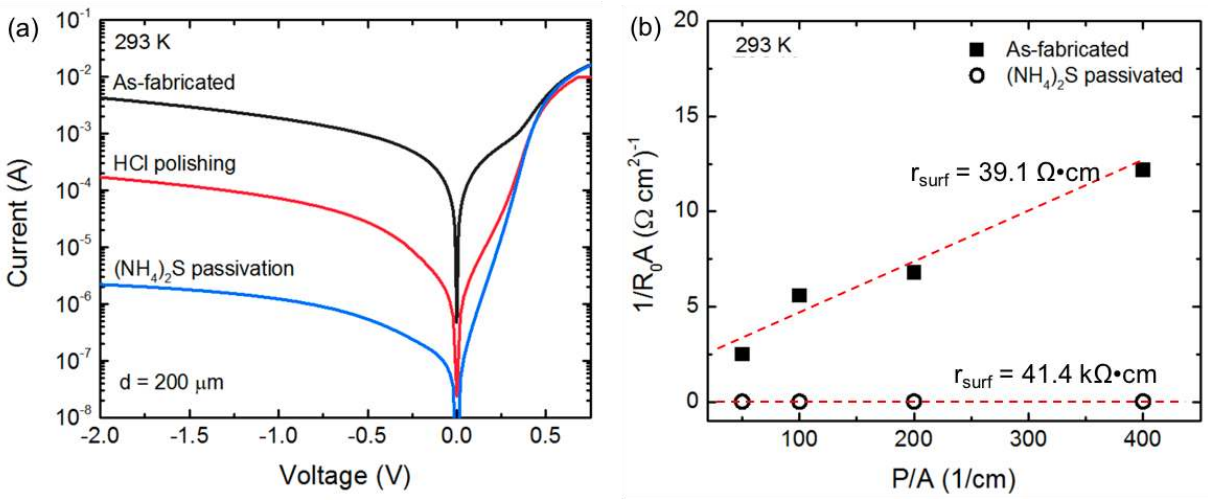

Figure 3-2 (a) Dark I-V curves of a 200-μm-diameter GaSb PIN device mesa after different surface treatments. (b) The inverse of the zero-bias dynamic resistance-area product against perimeter-to-area ratios of different mesa sizes.

3.3 Electrical characterization

3.3.1 Device capacitance

The measured device capacitance shows good agreement with the modeled curve against different temperatures (Fig. 3-3), confirming the designed device structure. The minimal change in these curves also suggests that the electric field profiles maintain approximately the same across temperatures. All of the measured capacitance curves are also scalable to different size mesas, indicating a good accuracy of the measurement. The i-region doping concentration has been extracted to be about 2.6×10^{16} cm^{-3} based on the slope of the $1/C^2$-V analysis. The simulated device

capacitance with and without Te-compensation are also shown in Fig. 3-3, suggesting a nearly 33% reduction in detector capacitance. It is worth noting that the device capacitance continues decreasing with increased reverse bias until breakdown, indicating that the i-region is not yet fully depleted even at breakdown voltage.

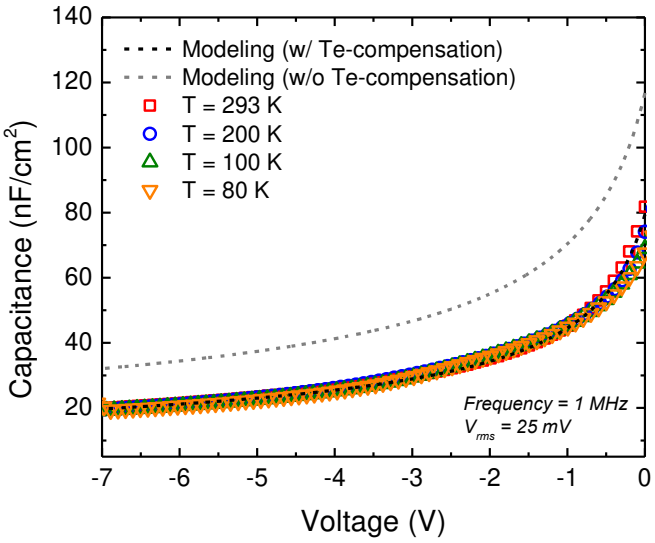

Figure 3-3 Capacitance per unit area against reverse bias of the GaSb PIN devices at different temperatures.

3.3.2 Dark current and $\mu\tau$ products

Room-temperature current density-voltage (J-V) curves of the GaSb PIN devices with different size mesas are shown in Fig. 3-4. At forward bias, the GaSb devices exhibit an ideality factor of approximately 1.4, indicating a combination of diffusion current and generation-recombination current. At reverse bias, it can be clearly seen that the dark current still has minor surface leakage component since the current density does not scale with device active area and tends to have a larger magnitude for a smaller mesa size. In general, the reverse bias current can be separated into three regimes. From 0 V to 6 V, the primary dark current in the device is produced by the generation-recombination current, as the current plateau suggests a relatively weak

dependence on the electric field. From 6 V to 9.5 V, the dark current increases considerably with reverse bias, and the devices start to exhibit bulk-limited behavior as the current densities of different size mesas begin to overlap. In this regime, the dark current varies strongly with electric filed, suggesting that the dominant current component is likely due to tunneling. Beyond 9.5 V, the device breakdown takes place to all size mesas, as indicated by a sharp increase in dark current and which eventually becomes limited by the series resistance.

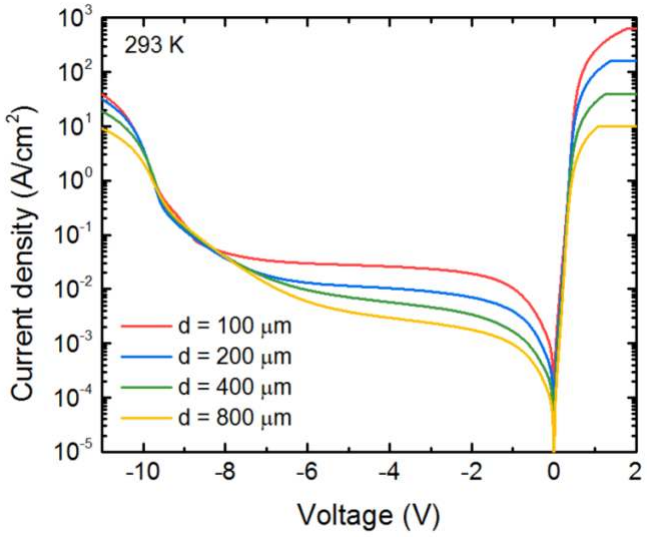

Figure 3-4 Room temperature current density of the GaSb PIN devices detectors with various size mesas.

A more detailed analysis is performed to obtain a further understanding of the GaSb device dark current and build a reliable device model. This can be achieved by using the equation

$$I(T,r) = J_{bulk}(T,r) \cdot \pi r^2 + J_{surf}(T,r) \cdot 2\pi r \,, \tag{3.2}$$

which allows the bulk current component $J_{bulk}(T,r)$ and the surface current component $J_{surf}(T,r)$ to be separated by fitting Eq. 3.2 to total dark current $I(T,r)$ measured from different size mesas with radius r at temperature T. In Fig. 3-5(a), the dark current at forward bias can be fitted using a double-diode model, as given by

$$J_{bulk} = J_{diff} + J_{gr} + \frac{V'}{R_{sh}}, \tag{3.3}$$

where V' is the applied bias including the effect from series resistance, R_{sh} is the shunt resistance, J_{diff} is the diffusion current, and J_{gr} represents the generation-recombination current within the space charge region in forward bias. R_{sh} is assumed to be infinity for a negligible surface effect, since the bulk current is used. The diffusion current J_{diff} can be described by[21]

$$J_{diff} = J_0(\exp\left(\frac{qV'}{kT}\right) - 1), \tag{3.4}$$

and the generation-recombination current J_{gr} is given by[22]

$$J_{gr} = \frac{qn_iW}{\tau_{gr}} \frac{sinh\left(-\frac{qV'}{2k_BT}\right)}{q(V_{bi} - V')/k_BT} f(b), \tag{3.5}$$

where n_i is the intrinsic carrier concentration (= 1.22×10^{12} cm^{-3} at 293 K), W is the width of the space charge region, τ_{gr} is the carrier lifetime, V_{bi} is the built-in potential, and $f(b) = \int_0^\infty \frac{du}{u^2-2bu+1}$ with $b = \exp(-\frac{qV'}{2k_BT})$. As a result, the carrier lifetime can be extracted using the J_{gr} model with the assumption that the primary carrier recombination is governed by Shockley-Read-Hall (SRH) statistics, and the dominant trap states are located at mid-gap. The carrier lifetime τ_{gr} of 8.0±0.3 ns has thus been extracted for electrons and holes by the best fit using Eq. 3.5, similar to the previously reported experimental value for GaSb diodes[23–25]. In addition, the carrier mobilities were obtained previously from Hall effect measurements, and were 3200 cm^{2}V^{-1}s^{-1} for electrons and 580 cm^{2}V^{-1}s^{-1} for holes. As a result, the $\mu\tau$ of GaSb could be calculated as ~3×10^{-5} cm^{2}V^{-1} for electrons, and ~5×10^{-6} cm^{2}V^{-1} for holes. These values are comparable to the

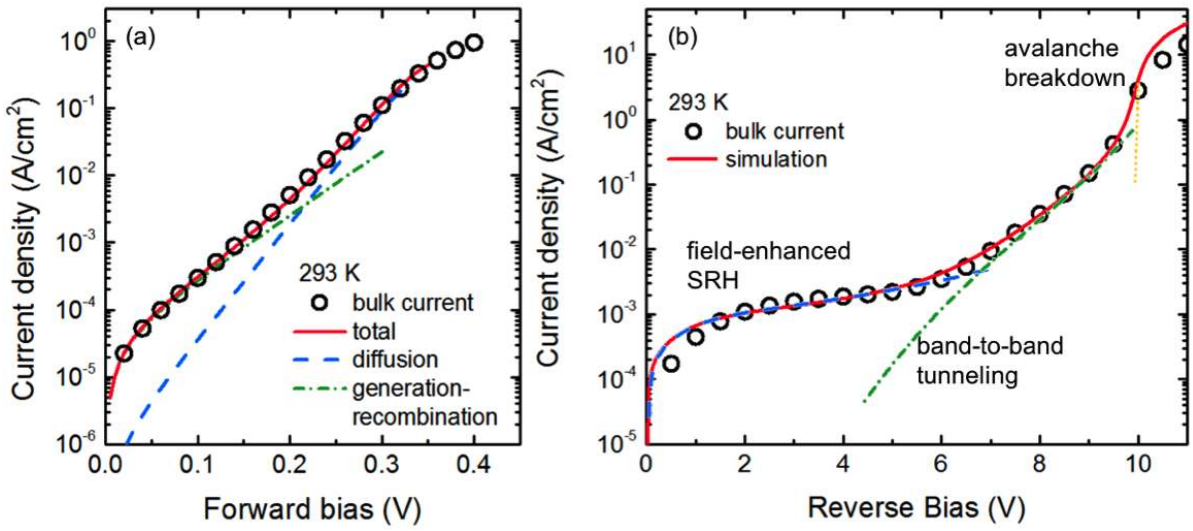

Figure 3-5 (a) Room-temperature bulk-limited dark current at forward bias, associated with simulated double-diode model composed by diffusion current and recombination current. (b) Bulk-limited dark current at reverse bias, associated with simulated current components using Sentaurus TCAD tool.

experimental $\mu\tau$ for GaAs[26], but still nearly two orders of magnitude lower than CdTe[17,27]. However, a much longer intrinsic carrier lifetime of 500 ns has been reported for GaSb at room temperature by minimizing the effect of surface/interface recombinations[19]. This indicates that $\mu\tau$ products of 1×10^{-3} cm^{2}V^{-1} for electrons, and 5×10^{-4} cm^{2}V^{-1} for holes are possible, and GaSb could be a promising candidate that suffers less signal distortion due to hole tailing effect.

At reverse bias, the analytical models no longer easily describe the observed dark current in the GaSb device. As a result, Sentaurus TCAD has been used to provide numerical modeling to understand the observed characteristics, as shown in Fig. 3-5(b). Three major current mechanisms are found to account for the bulk current in the GaSb PIN devices. At small bias range, the dark current is primarily due to the generation-recombination current with field-enhanced SRH lifetimes described by the Hurkx et al.[28]. The field-enhanced SRH process illustrates the increased electron-hole pair generation rate under strong field before band-to-band tunneling (BTBT) or avalanche process becomes dominant. The soft breakdown characteristics with increasing reverse

bias from 6 V to 9.5 V is due to the BTBT (>100 kV/cm), which has also been supported by a relatively small temperature dependence as will be discussed in the later section. The BTBT current has been commonly observed in small-bandgap materials, such as InAs, Ge, and HgCdTe, and here it is initiated by the strong band-bending with the peaking electric field in the GaSb devices (Fig. 3-6). Finally, the current dramatically increases due to the avalanche process, and device breakdown occurs at around 10 V.

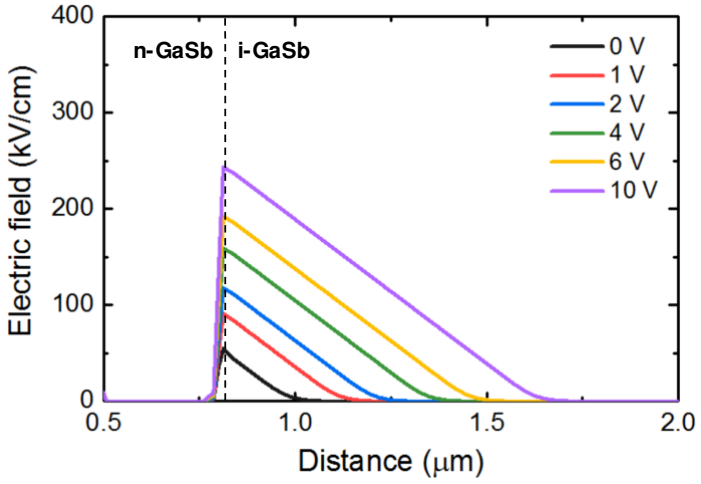

Figure 3-6 Simulated electric field profile in the GaSb PIN device as a function of reverse bias. The peak electric field is present at the junction which grows with increasing bias and leads to the BTBT current.

3.3.3 Activation energy

Temperature-dependent dark I-V measurement is shown in Fig. 3-7(a). The generation-recombination current has shown a strong temperature dependence as expected. On the other hand, the BTBT current component is almost independent of the variation in temperature, but it depends strongly on the reverse bias. Finally, the breakdown voltage (V_{BD}) suggests a temperature coefficient of -10.7 mV/K, suggesting the avalanche generation behavior. The dark current activation energies of possible defects were extracted by fitting the semilog plot of J-$V^{3/2}$, as shown

in Fig. 3-6(b). The activation energy at high-temperature range was extracted to be 0.252±0.008 eV, which is likely due to the intrinsic doubly ionizable complex of $V_{Ga}Ga_{Sb}$[29–31]. This type of defect is formed by the Ga self-diffusion into Sb vacancy V_{Sb}, and further transformed into the energetically favorable complex of $V_{Ga}Ga_{Sb}$ that has been widely considered as the cause of the background doping in GaSb. In addition, an activation energy of 0.075±0.003 eV was obtained at a temperature below 200 K, likely due to the small separation between the surface states.

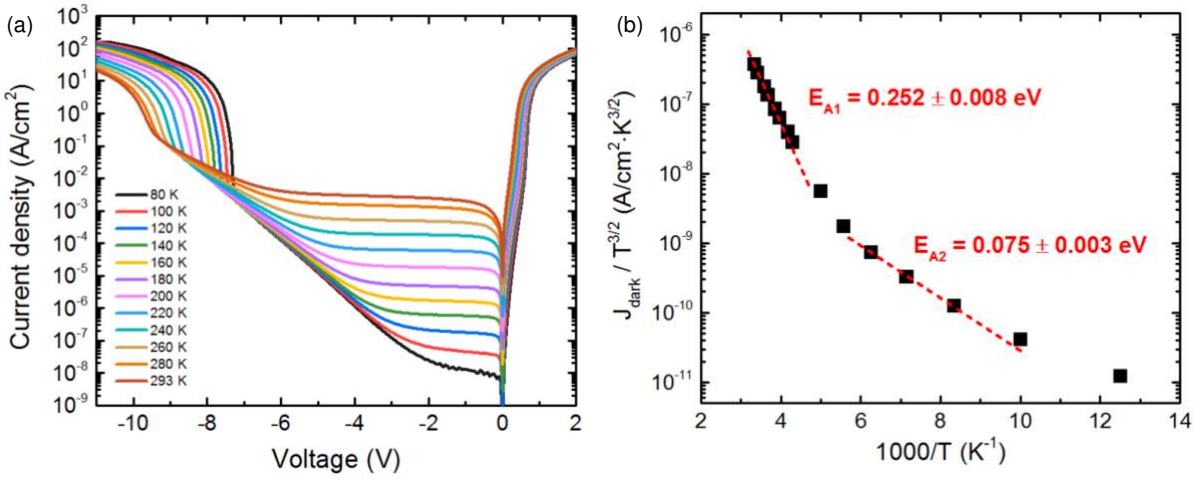

Figure 3-7 (a) Current density of the GaSb PIN device at different temperatures, and (b) Arrhenius plot of the current density at 0.5 V against inverse temperatures.

3.4 Optical characterization

3.4.1 Quantum efficiency

The optical response of the GaSb PIN devices is measured to verify that the devices are optically active and to extract the carrier collection efficiency. The continuous wave (CW) laser emitting at 1310 nm is used to limit optical excitation in GaSb. More than 98% of the photons are calculated to be absorbed within the nominal device structure, as shown in Fig. 3-8.

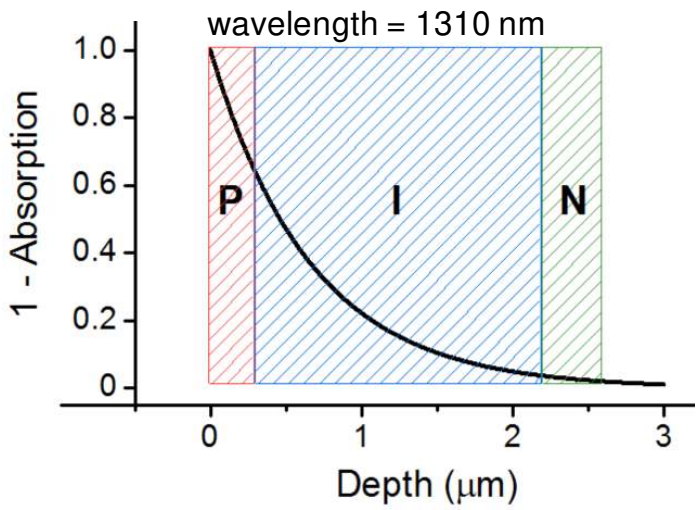

Figure 3-8 Absorption profile of the photons at the wavelength of 1310 nm incident on the GaSb PIN device.

The photocurrents with varying excitation power density ranging from 20 to 115 W/cm^2 were used to measure external quantum efficiency (EQE). The laser excitation powers were calibrated prior to all measurements using a commercial Ge detector, and extra cares were taken to make sure the device active area was underfilled with the coupled light spot. The responsivity at unity gain is 0.455 A/W at room temperature, which corresponds to an EQE of 43%. However, this does not present the true collection efficiency. In the application such as gamma-ray detectors, the measure of internal quantum efficiency (IQE) could offer more useful insight since it considers the conversion of the absorbed photons to collected electrons by excluding the effects of photon reflection and transmission. The IQE could usually be derived directly from EQE by using the following equation:

$$IQE = \frac{EQE}{1 - R - T}\ , \tag{3.6}$$

where R and T are the reflectance and transmittance of the device. The reflectance of the top surface of the GaSb PIN device has been measured to be approximately 44% using FTIR and

Continuum FTIR microscope. With an estimated transmittance of 2%, the IQE can be calculated to be 80% at room temperature. The value could easily be underestimated since the actual transmittance may be larger than the theoretical calculation. In addition, the loss of carrier is likely due to undesired recombination occurring at the surfaces or through bulk defects.

3.5 X-ray and gamma-ray measurement

After electrical and optical characterizations, the devices were packaged onto a TO-header (Fig. 3-9) for radiation measurements. The best performing (and representative) 200-μm-diameter GaSb PIN device was cooled down to 140 K exhibiting a dark current of ~0.2 nA, and the device was also biased at -2 V to obtain a detector capacitance of 11.1 pF without causing avalanche multiplication. Further reducing the temperature shows little improvement in electronic noise, since it begins to be limited by the measurement system, i.e. the leakage current from the FET in the charge sensitive preamplifier and the total capacitance, rather than the device properties. The device temperature was controlled by a Lakeshore Model 331 cryogenic temperature controller, and the fluctuation was less than ±0.02 K throughout the measurement. The count rate was maintained to be less than 200 counts per second to eliminate pulse pile-up. The optimum shaping time ranging from 0.25 μs to 6 μs was determined by measuring the FWHM of a long tail pulse signal (time constant = 100 μs) from a Berkeley Nucleonics pulse generator. This pulse was sent to the test input of the preamplifier and coupled to the main input of the preamplifier through a test capacitor of 0.5 pF. Test pulses were sent to the preamplifier while the GaSb device remained connected to the main input, allowing the noise measurements to include the contribution from the device. The optimum shaping time (lowest FWHM obtained) of 1 μs was chosen, as shown in Fig. 3-10, for all the spectroscopy measurement discussed later if not mentioned otherwise.

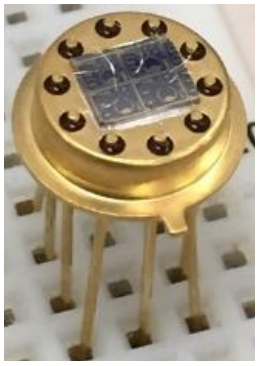

Figure 3-9 The selected detectors are wire-bonded onto a TO-header.

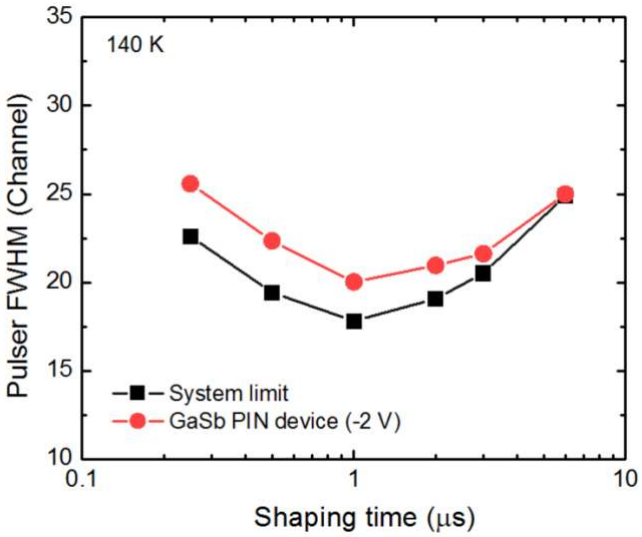

Figure 3-10 Pulser FWHM at the MCA output as a function of shaping time. The system limit is also shown, which measurement includes the cryostat (without the device connected), preamplifier, and shaping amplifier.

3.5.1 ^{55}Fe spectrum

The soft X-ray response of the 200-μm-diameter GaSb PIN device to a 44 kBq ^{55}Fe radioactive source at 140 K is shown in Fig. 3-11. The device exhibits a noise floor at approximately 3.5 keV, and the ^{55}Fe source gives characteristic Mn Kα and Kβ X-rays at 5.89 keV and 6.49 keV deduced by two Gaussian distributions from the observed photopeak. The obtained photopeak FWHM is 1.238±0.028 keV at 5.89 keV, whereas the pulser FWHM is 1.231±0.014 keV. We also found that the pulser FWHM was greatly limited by the electronic noise generated by the measurement system, e.g. preamplifier, cabling, etc., rather than the GaSb PIN device. The pulser FWHM without the device was measured to be 1.078±0.004 keV (157 electron rms) and increased to 1.231±0.014 keV (179 electron rms) when the device was connected (assuming a PCE of 2.92 eV at 140 K)[4,21]. As a result, we expect a substantial improvement in energy resolution and

reduction in noise floor, i.e. minimum attainable photopeak energy, if the noise from the measurement system can be improved, as will be discussed in the later section.

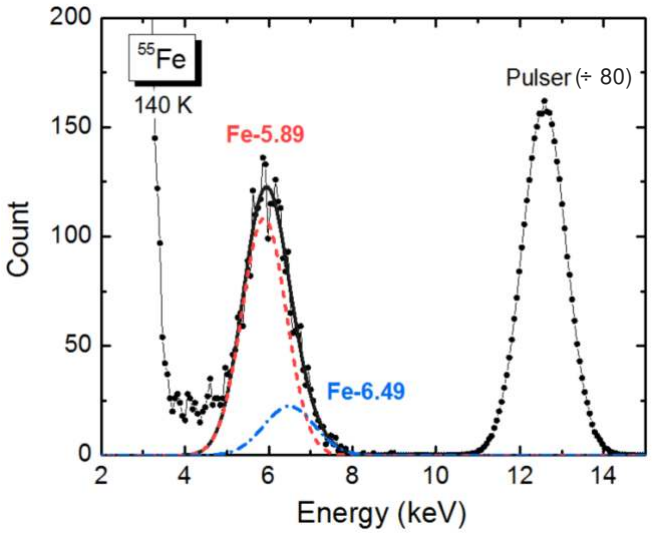

Figure 3-11 Soft X-ray response of the GaSb device with a 44 kBq ^{55}Fe source acquired in 1.5 hours at 140 K. The dashed lines represent the Gaussian distributions fittings of monoenergetic lines at 5.89 keV and 6.49 keV.

3.5.2 ^{241}Am spectrum

The energy spectrum with high-energy photons was also studied using a 1.55 GBq ^{241}Am source (Fig. 3-12) to allow better statistics for gamma-ray detection within the thin absorption region. We observe only the 59.5 keV photons directly from the source since the packaging of the source has effectively attenuated the other photons with lower energies. The principle line at 59.5 keV could be clearly identified and exhibited a FWHM of 1.789±0.057 keV. In addition, two strong photopeaks were also observed at 33.2 keV and 26.3 keV. Because the emission probability of 33.2 keV (0.13%) from ^{241}Am is significantly lower than that of 59.5 keV (35.9%), the relatively strong photopeak observed is not likely originating from ^{241}Am but could be attributed to Sb Kα escape peak from 59.5 keV. On the other hand, the 26.3 keV peak could be explained by the

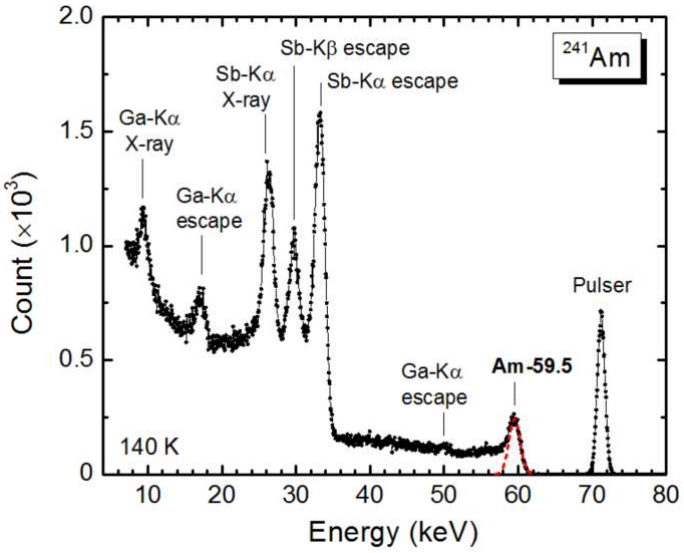

Figure 3-12 Gamma-ray response of the GaSb device with a 1.55 GBq ^{241}Am source acquired in 1 hour at 140 K. The test pulse, measured under the same condition, is also shown in the energy spectrum.

backscattered Sb Kα characteristic X-rays generated from 59.5 keV photons stopped outside the active region of the detector, similar to the Ga Kα characteristic X-rays at 9.25 keV. The remaining photopeaks near 29.8 keV and 17.1 keV could be assigned accordingly as the Sb Kβ escape peak from 59.5 keV and the Ga Kα escape peak from the 26.3 keV Sb Kβ characteristic X-rays, respectively. A 0.74 MBq ^{241}Am source has also been used to assist the identification of photopeaks and the detector's spectroscopic response, as shown in Fig. 3-13. The effect of the avalanche gain to the photogenerated carriers can be characterized using the photopeak positions as a function of reverse bias, as shown in Fig. 3-14. Albeit with a relatively small range of avalanche gain, the photopeaks obtained by 59.5 keV form the ^{241}Am source are shown to be in good agreement with the gain curve measured using the 1310 nm laser.

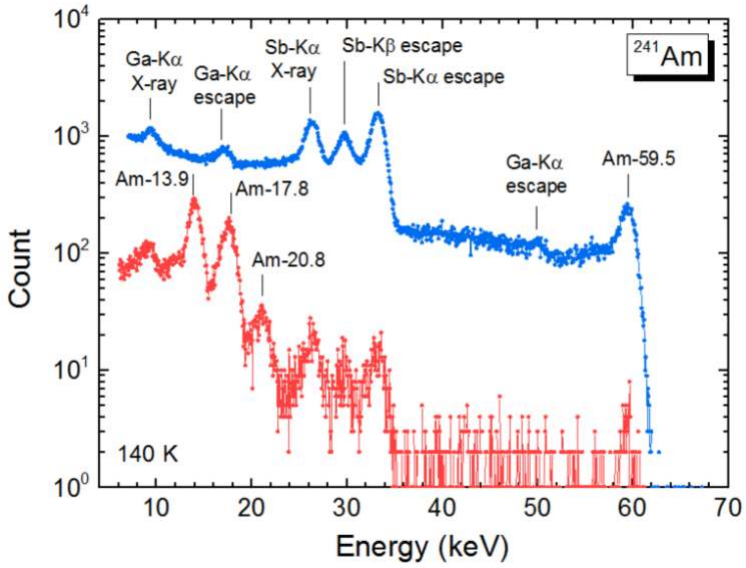

Figure 3-13 Comparison of spectra acquired by the GaSb device with a 1.55 GBq (blue) and a 0.74 MBq (red) ^{241}Am sources at 140 K.

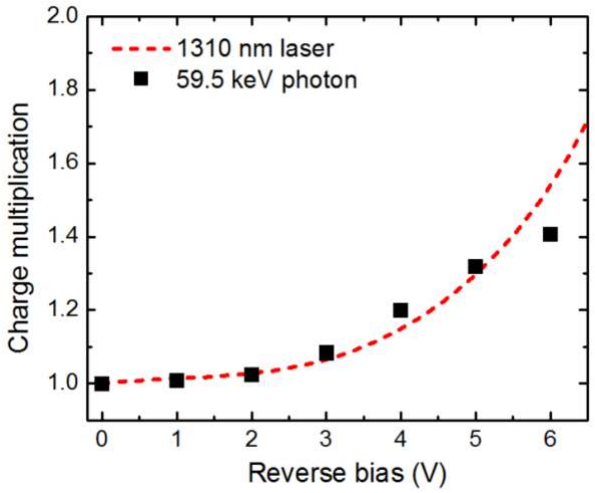

Figure 3-14 Charge multiplication of the GaSb PIN device obtained using the 59.5 keV photopeaks which shows good agreement with the 1310 nm laser measurement at 140 K.

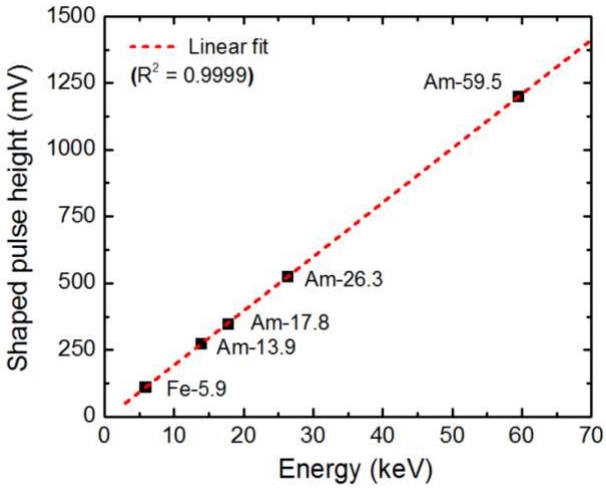

Figure 3-15 Measured pulse height after shaping amplifier recorded by MCA with the corresponding photon energies from 5.9 keV to 59.5 keV using the GaSb PIN device at 140 K.

3.5.3 Detection linearity

The detection linearity of the GaSb PIN device has been characterized using energy lines from 5.89 to 59.5 keV from the sources discussed above. The shaped pulse heights (or the signals registered as the MCA channel numbers) show good agreement with corresponding photon energies. A linear fitting shows the coefficient of determination $R^2 = 0.9999$, indicating good detection linearity of the GaSb PIN device (Fig. 3-15).

3.5.4 Pair creation energy

The number of generated charges, i.e., electron-hole pairs, can be calculated based on the comparison between the ^{241}Am spectra obtained by the GaSb PIN device and a GaAs PIN reference device, as shown in Fig. 3-16. A GaAs PIN device with an identical absorber thickness has been fabricated along with the GaSb devices except for contact metallization. The representative 200-μm-diameter GaAs PIN device was wire-bonded onto TO-header for radiation measurement, which exhibits a dark current about 1 nA at 140 K and a device capacitance of 2.1 pF under reach-through condition at -10 V. It should be noted that the difference in detector capacitances can possibly result in a slight variation in amplification factor of the preamplifier, leading to errors in PCE estimation. The ideal way to conduct the PCE measurement is by measuring both devices in parallel and connecting them to the same input of the electronic chain[32]; however, this would require a significant modification to the detector-preamplifier circuitry in our measurement system. Alternatively, this issue is solved via a simplified approach. Since the change in amplification factor is common to all signals at the input of the preamplifier, the effect can be calibrated using the difference in pulser peak channels when different devices are connected.

The room-temperature GaAs PCE has been reported to be 4.184±0.025 eV with a temperature coefficient of -0.00122 eV/K[32]. As a result, the calculation of GaAs PCE at 140 K is

relatively straightforward as well as the conversion between photon energy and the number of charges created. By comparing the energy spectra using known photopeaks for both device materials, the pair creation energy of GaSb can be estimated by using the equation,

$$\varepsilon_{GaSb} = \varepsilon_{GaAs} \cdot \left(\frac{Q_{GaSb} N_{GaAs}}{Q_{GaAs} N_{GaSb}}\right), \tag{3.7}$$

where ε is the pair creation energy, Q is the charge collection efficiency, N is the apparent generated charges and the underlined notation indicates the material of interest. Q_{GaAs} is assumed to be 1, since the device was measured under the reach-through condition and there is negligible change in photopeak position with a further increase in reverse bias. The ε_{GaSb} is hence estimated experimentally to be 2.884±0.012 eV at 140 K. Noted that a complete carrier collection ($Q_{GaSb} = 1$) has been assumed, whereas this value can be overestimated and a smaller ε_{GaSb} value will be obtained if Q_{GaSb}<1.

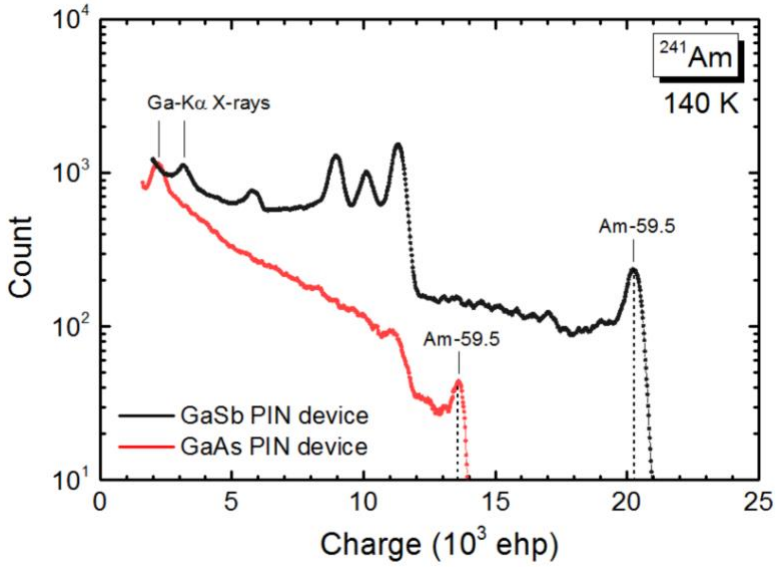

Figure 3-16 Spectra of ^{241}Am generated by the GaSb PIN device and the GaAs reference device. The number of charges is calibrated by the known GaAs PCE value.

3.6 Noise analysis

The noise analysis of the radiation measurement can be carried out by characterizing the obtained photopeak FWHM using the formula

$$FWHM\ (eV) = 2.355 \cdot \varepsilon \cdot \sqrt{\left(\frac{FE}{\varepsilon}\right) + A^2 + R^2}\ , \tag{3.8}$$

where ε is the pair creation energy, F is the Fano factor (assumed to be 0.12), A is the electronic noise, and R is the excess noise (or sometimes referred as trapping noise). The electronic noise can be further expressed in a shaping time-dependent form,

$$A^2 = K_1 \cdot \frac{1}{\tau_{sh}} + K_2 + K_3 \cdot \tau_{sh}\ , \tag{3.9}$$

where K_1, K_2, and K_3 represent the analytical formula of series noise, parallel noise, and the dielectric noise, respectively (more details can be found in Appendix B). The excess noise is taking

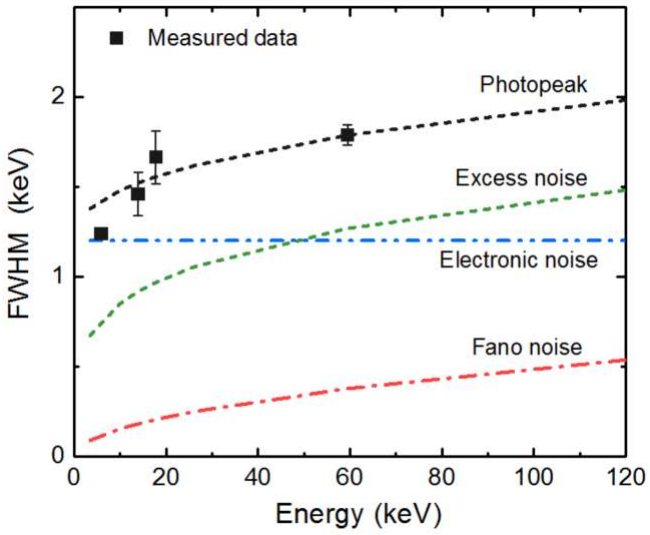

Figure 3-17 FWHM of photopeaks and the separated noise components as a function of photon energy measured by the GaSb PIN device.

account of the extra fluctuation in the total number of generated carriers that is not based on Fano statistics or generated by the electronic noise, and it is often considered as a result of incomplete carrier collection due to charge trapping. The measured photopeak FWHM values against incident photon energies are plotted in Fig. 3-17. It is shown that the spectroscopic performance of the GaSb PIN device is primarily limited by the electronic noise at low energies, and the effect of excess noise becomes more dominant toward higher energies.

3.6.1 Electronic noise

The obtained X-ray and gamma-ray energy resolution using the GaSb PIN device has been shown to be largely limited by the electronic noise in the measurement system. Fig. 3-18 shows the FWHM of the 59.5 keV photopeaks and the associated noise components as a function of temperature. The FWHM decreases dramatically with temperature, owing to a reduced dark

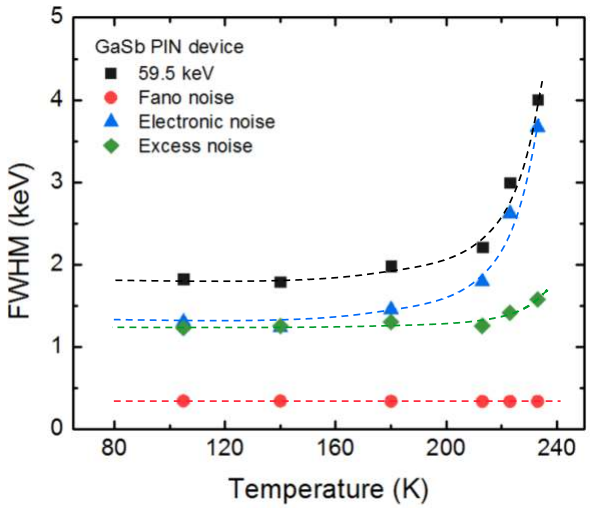

Figure 3-18 Temperature-dependent FWHM values of the 59.5 keV photopeaks with different noise components decoupled using Eq. 3-7. The dashed lines are used as a guide to the eyes.

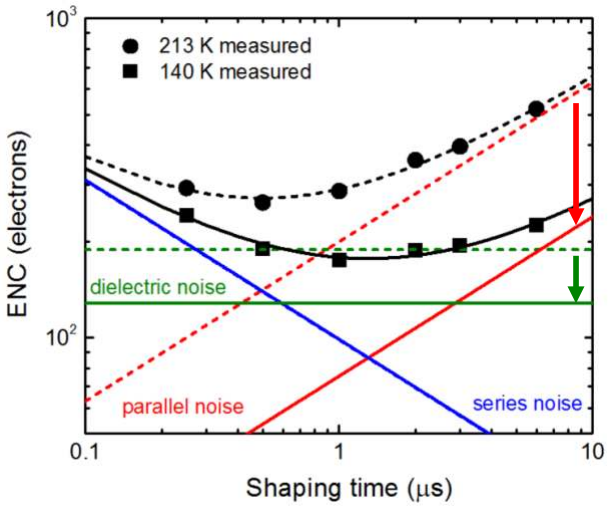

Figure 3-19 ENC analysis of the electronic noise at 213 K (dashed) and 140 K (solid) with the GaSb PIN device at a reverse bias of 2 V.

current in the GaSb PIN device. The rate of change is decreased below 180 K because the device dark current becomes sufficiently low and the other effects such as series noise and dielectric noise emerged. Fig. 3-19 illustrates the separated electronic noise components in terms of equivalent noise charge (ENC) of the GaSb device at 213 K and 140 K. The parallel noise accounts for dark current from the device and the FET of the preamplifier, and the series noise is directly related to the total input capacitance. It can be seen that the change in measured electronic noise is primarily determined by the parallel noise, whereas the series noise is almost unchanged with decreased temperature since the device capacitance is kept constant.

On the other hand, series noise is a strong function of total input capacitance ($\propto C_{tot}^2$), composed of device capacitance, preamplifier capacitance, and stray capacitance. The stray capacitance is likely produced by the cables between the device and input of the preamplifier. Since the device capacitance is bias-dependent, with a known preamplifier capacitance, the stray

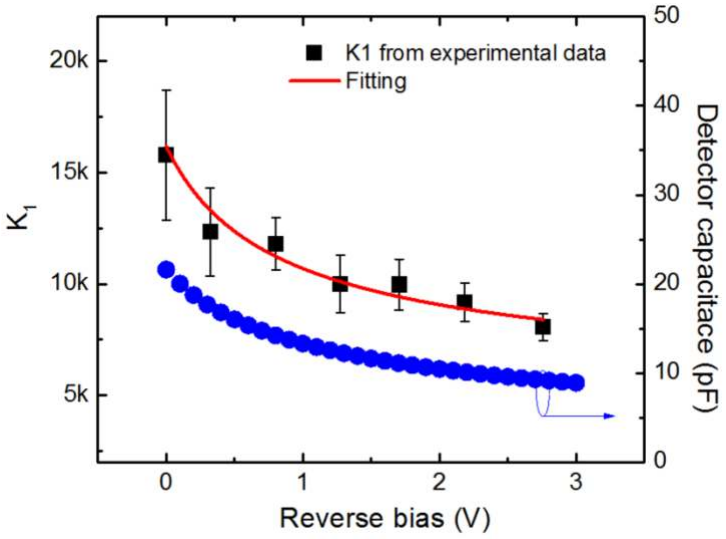

Figure 3-20 Fitting to parallel noise factor using the bias-dependent ENC analysis of the GaSb PIN device at 140 K.

capacitance can be extracted to be 14±4 pF, as shown in Fig. 3-20. An improvement in spectroscopic resolution is expected if the electronic noise from the preamplifier stage could be minimized. The ultra-low noise of ~42 electron rms reported by Bertuccio et al. was using a customized preamplifier without the feedback resistor[33], and Owens et al. also reported electronic noise of 19 electron rms with GaAs detectors using an upgraded preamplifier with the same design[34]. Those values are much lower than measured electronic noise (157 electron rms), indicating that an enhanced energy resolution using the GaSb devices could be attained.

3.6.2 Excess noise

The decoupled excess noise components as a function of temperature are also shown in Fig. 3-18. Interestingly, the excess noise shows a relatively weak temperature dependence and maintains at approximately 1.25 keV below 213 K. This indicates that the carrier loss process is likely limited by surface recombination or mechanisms other than bulk defect-related trapping, which is normally regarded as a strong function of temperature. Fig. 3-21 shows noise components at 59.5 keV as a function of reverse bias at 140 K. The initial decrease in the electronic noise is due to a reduced device capacitance, and the following increase beyond 4 V is due to the increased dark current. On the other hand, the excess noise exhibits a dissimilar trend, which maintains approximately the same up to reverse bias of 2 V and starts to increase with increasing reverse bias. The field-dependent excess noise is hypothesized as a result of additional charge fluctuation introduced by the impact ionization in the early avalanche process (Fig. 3-14). This suggests that, in order to reduce excess noise, the electric field strength in the GaSb absorber is also a critical parameter in the device design consideration. Furthermore, the excess noise is expected to be improved by adding surface barriers to eliminate undesired carrier loss via surface recombination.

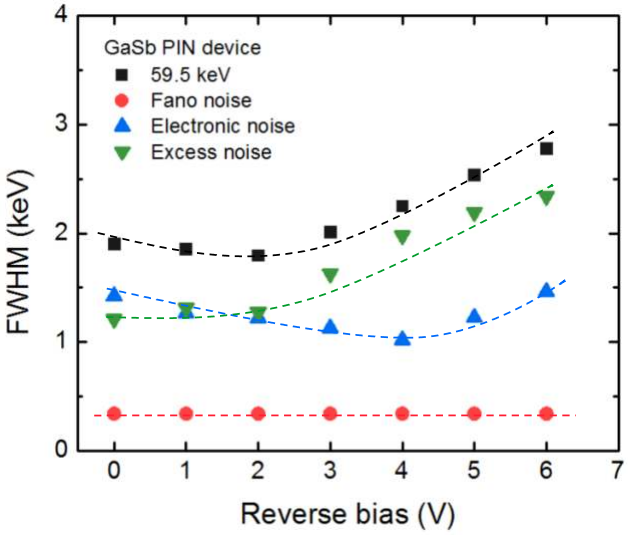

Figure 3-21 Different noise components obtained by the GaSb PIN device as a function of reverse bias at 140 K. The dashed lines are used as a guide to the eyes.

3.7 Discussion

In conclusion, GaSb can offer high stopping power, good carrier transport, and low PCE characteristics that are advantageous for the gamma-ray detection. We have studied the electrical characteristics of homojunction GaSb PIN devices. The $\mu\tau$ values of electrons and holes at room-temperature have been extracted as 3×10^{-5} cm^2V^{-1} and 5×10^{-6} cm^2V^{-1}, respectively, and the attainable $\mu\tau$ values of 1×10^{-3} cm^2V^{-1} for electrons and 5×10^{-4} cm^2V^{-1} for holes are suggested using the structure with eliminated surface recombination. At 140K, we have demonstrated a range of energy-sensitive radiation responses from 5.89 keV to 59.5 keV using ^{55}Fe and ^{241}Am radioactive sources, and the GaSb PIN device showed good detection linearity. The energy resolution at 5.89 keV photopeak is found to be strongly limited by the electronic noise presented in the measurement system. The 59.5 keV photopeak is well-defined, exhibiting a minimum FWHM of 1.789±0.057 keV. The contribution of the electronic noise and the excess noise components are investigated

and analyzed with varying reverse bias and temperature, and the results show that an enhanced spectroscopic performance can be achieved by improving the device structure to optimize the electric field profile and minimize the effects of surface recombination.

3.8 Reference

1. Bennett, B. R., Magno, R., Boos, J. B., Kruppa, W. & Ancona, M. G. Antimonide-based compound semiconductors for electronic devices: A review. *Solid. State. Electron.* **49,** 1875–1895 (2005).

2. Guo, L. W. *et al.* Enhancing p-channel InGaSb QW-FETs via process-induced compressive uniaxial strain. *IEEE Electron Device Lett.* **35,** 1088–1090 (2014).

3. Lu, W., Kim, J. K., Klem, J. F., Hawkins, S. D. & del Alamo, J. A. An InGaSb p-channel FinFET. in *Electron Devices Meeting (IEDM), 2015 IEEE International* 31–36 (IEEE, 2015).

4. Chastanet, D. *et al.* High temperature, single mode, long infrared (λ= 17.8 μ m) InAs-based quantum cascade lasers. *Appl. Phys. Lett.* **105,** 111118 (2014).

5. Yu, L., Zhong, Y., Dev, S. & Wasserman, D. Engineering carrier lifetimes in type-II In(Ga)Sb/InAs mid-IR emitters. *J. Vac. Sci. Technol. B, Nanotechnol. Microelectron. Mater. Process. Meas. Phenom.* **35,** 02B101 (2016).

6. Rogalski, A., Antoszewski, J. & Faraone, L. Third-generation infrared photodetector arrays. *J. Appl. Phys.* **105,** 4 (2009).

7. Rogalski, A., Kopytko, M. & Martyniuk, P. InAs/GaSb type-II superlattice infrared detectors: three decades of development. in **10177,** 1017713–1017715 (2017).

8. Plis, E. A. InAs/GaSb type-II superlattice detectors. *Adv. Electron.* **2014,** (2014).

9. Downs, C. & Vandervelde, T. E. Progress in infrared photodetectors since 2000. *Sensors* **13,** 5054–5098 (2013).

10. Vaughan, E. I., Rahimi, N., Balakrishnan, G. & Hecht, A. A. Thin-Film Gallium Antimonide for Room-Temperature Radiation Detection. *J. Electron. Mater.* **44,** 3288–3293 (2015).

11. Sato, Y., Morita, Y. & Kanno, I. Performance estimation of InSb compound semiconductor detectors as a function of active area using alpha particles. *Nucl. Instruments Methods Phys. Res. Sect. A Accel. Spectrometers, Detect. Assoc. Equip.* **737,** 1–4 (2014).

12. Dutta, P. S., Bhat, H. L. & Kumar, V. The physics and technology of gallium antimonide: An emerging optoelectronic material. *J. Appl. Phys.* **81,** 5821–5870 (1997).

13. Coutts, T. J. A review of progress in thermophotovoltaic generation of electricity. *Renew. Sustain. Energy Rev.* **3,** 77–184 (1999).

14. Huang, J. L. *et al.* Narrow-Band Type II Superlattice Photodetector With Detection Wavelength Shorter Than 2 mu m. *Ieee Photonics Technol. Lett.* **27,** 2276–2279 (2015).

15. Rodriguez, J. B. *et al.* nBn structure based on InAs/GaSb type-II strained layer superlattices. *Appl. Phys. Lett.* **91,** 43514 (2007).

16. Craig, A. P., Reyner, C. J., Marshall, A. R. J. & Huffaker, D. L. Excess noise in GaAs and AlGaAs avalanche photodiodes with GaSb absorption regions-composite structures grown using interfacial misfit arrays. *Appl. Phys. Lett.* **104,** (2014).

17. Owens, A. & Peacock, A. Compound semiconductor radiation detectors. *Nucl. Instruments Methods Phys. Res. Sect. A Accel. Spectrometers, Detect. Assoc. Equip.* **531,** 18–37 (2004).

18. Barnett, A. M., Lees, J. E. & Bassford, D. J. Temperature dependence of the average electron-hole pair creation energy in Al0.8Ga0.2As. *Appl. Phys. Lett.* **102,** (2013).

19. Scofield, A. C. *et al.* Modeling and spectroscopy of carrier relaxation in semiconductor

optoelectronics. in *Proceedings of SPIE - The International Society for Optical Engineering* **10193,** (2017).

20. Juang, B.-C. *et al.* GaSb thermophotovoltaic cells grown on GaAs by molecular beam epitaxy using interfacial misfit arrays. *Appl. Phys. Lett.* **106,** (2015).

21. Sze, S. M. & Ng, K. K. *Physics of semiconductor devices*. (John Wiley & Sons, 2006).

22. Chih-Tang, S., Noyce, R. N. & Shockley, W. Carrier Generation and Recombination in P-N Junctions and P-N Junction Characteristics. *Proc. IRE* **45,** 1228–1243 (1957).

23. Polyakov, A. Y., Stam, M., Milnes, A. G. & Schlesinger, T. E. Electrical properties of GaSb Schottky diodes and p-n junctions. *Mater. Sci. Eng. B* **12,** 337–343 (1992).

24. Stollwerck, G., Sulima, O. V & Bett, A. W. Characterization and simulation of GaSb device-related properties. *Electron Devices, IEEE Trans.* **47,** 448–457 (2000).

25. Titkov, A. N., Iluridze, G. N., Mironov, I. F. & Cheban, V. A. INTERBAND AUGER RECOMBINATION INVOLVING A SPIN ORBIT SPLIT-OFF VALENCE BAND IN P-TYPE GASB CRYSTALS. *Sov. Phys. Semicond.* **20,** 14–19 (1986).

26. Sun, G. C., Zazoui, M., Talbi, N., Khirouni, K. & Bourgoin, J. C. Mobility-lifetime product in epitaxial GaAs X-ray detectors. *Nucl. Instruments Methods Phys. Res. Sect. A Accel. Spectrometers, Detect. Assoc. Equip.* **573,** 228–231 (2007).

27. Takahashi, T. & Watanabe, S. Recent progress in CdTe and CdZnTe detectors. *Nucl. Sci. IEEE Trans.* **48,** 950–959 (2001).

28. Hurkx, G. A. M., Klaassen, D. B. M. & Knuvers, M. P. G. A new recombination model for device simulation including tunneling. *IEEE Transactions on Electron Devices* **39,** 331–338 (1992).

29. Hakala, M., Puska, M. J. & Nieminen, R. M. Native defects and self-diffusion in GaSb. *J. Appl. Phys.* **91,** 4988–4994 (2002).

30. Bracht, H. *et al.* Large disparity between gallium and antimony self-diffusion in gallium antimonide. *Nature* **408,** 69–72 (2000).

31. Kuramochi, E., Kondo, N., Takanashi, Y. & Fujimoto, M. Observation of deep levels in undoped GaSb grown by molecular beam epitaxy. *Appl. Phys. Lett.* **63,** 2664–2666 (1993).

32. Bertuccio, G. & Maiocchi, D. Electron-hole pair generation energy in gallium arsenide by x and γ photons. *J. Appl. Phys.* **92,** 1248–1255 (2002).

33. Bertuccio, G., Rehak, P. & Xi, D. A novel charge sensitive preamplifier without the feedback resistor. *Nucl. Instruments Methods Phys. Res. Sect. A Accel. Spectrometers, Detect. Assoc. Equip.* **326,** 71–76 (1993).

34. Owens, A. *et al.* High resolution x-ray spectroscopy using GaAs arrays. *J. Appl. Phys.* **90,** 5376–5381 (2001).

4. GaSb/GaAs heterostructure devices

4.1 Background

Detectors with decoupled absorption and junction stages are commonly referred to the separate absorption and multiplication (SAM) structure that has been extensively studied for InGaAs/InP[1,2], InGaAs/InAlAs[3–5], and Ge/Si[6–8] in the field of high-speed telecommunication and infrared single photon detectors. Similar device based on mismatched III-V material systems such as GaSb/GaAs became possible since the optimized material growth using interfacial misfit (IMF) technique by MBE was reported[9,10]. In addition, efforts have been made to initialize the development of such SAM structure with a target working wavelength around 1.7 μm and beyond[11]. The proposed radiation detector structure that consists of the high-Z, small-bandgap absorber with the low-Z, large-bandgap junction region is firstly approached using the GaSb/GaAs material system by taking advantages of their attractive material properties. GaAs is one of the most developed III-V materials that has mature fabrication technologies for semiconductor devices. The large bandgap (1.42 eV at 300 K) directly suggests a low intrinsic carrier concentration and promises low dark current at room-temperature. Most importantly, epitaxy of high quality and fully relaxed GaSb on GaAs is possible using the IMF technique, which has been reported to show detector-grade material quality[12–15]. As a result, GaSb/GaAs material system is considered as an ideal platform to realize the integrated device architecture.

In this chapter, the optical and electrical properties of the GaSb/GaAs devices are reported, and the avalanche multiplication behavior as well as the excess noise measurement are characterized at large reverse bias. The results of radiation response obtained by the packaged

devices are investigated and studied, providing useful information for the carrier transport behavior in the heterostructure and next-generation device design.

4.2 Device fabrication

4.2.1 GaSb grown on GaAs using IMF arrays

It is widely considered that for heteroepitaxial growth, the large strain between the mismatched materials seeds threading dislocations that dramatically reduce material quality and thus device performance. The normal epitaxial growth of GaSb on GaAs may introduce a large number of threading dislocations due to slow relaxation of the strain induced by the 7.8% lattice mismatch[16]. However, it has been demonstrated that nearly strain-free bulk GaSb could be grown directly on GaAs substrates using IMF arrays by MBE[9]. The IMF array is created by carefully controlling the substrate temperature and the timing for switching sequence between As and Sb atomic fluxes during the transition of the heterointerface, allowing periodic arrangement of the 90º misfit dislocations. For a typical IMF-based growth, strain relief of >99% can be achieved sharply at the heterointerface, and the threading dislocation density in the GaSb epitaxial layer is significantly reduced by three orders of magnitude[16,17]. Fig. 4-1(a) shows the cross-section transmission electron microscopy (TEM) image at the heterointerface, suggesting an abrupt, periodic IMF array. Furthermore, the absence of shoulders near the GaAs substrate peak in the high-resolution X-ray diffraction (HRXRD) scan confirms that GaSb layers do not undergo a slow relaxation process (Fig. 4-1(b)).

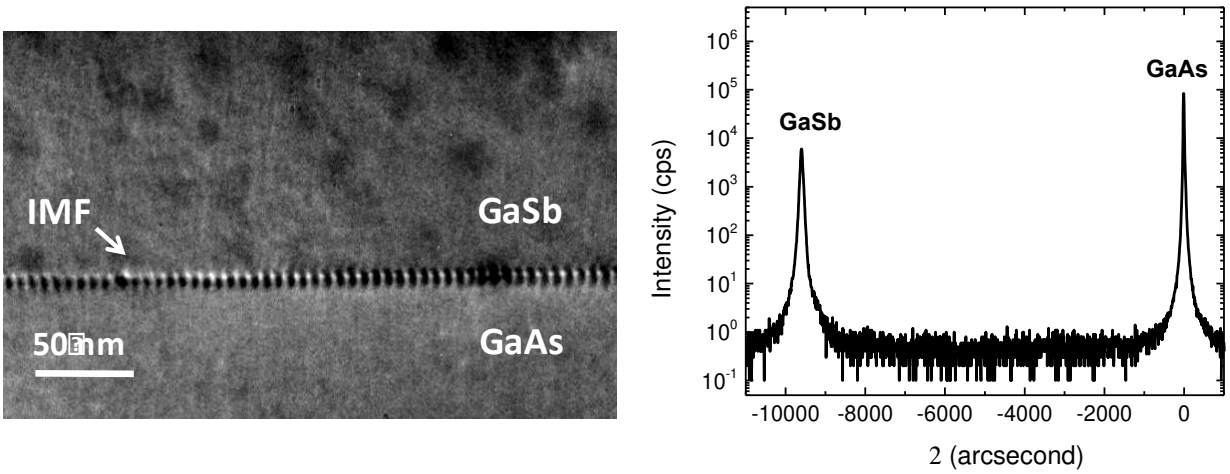

Figure 4-1 (a) Cross-section TEM along [110] of GaSb grown on GaAs using IMF arrays. The dark spots at the interface indicate the periodic locations of the misfit dislocations. (b) HRXRD ω-2θ scan of a 1.5-μm-thick GaSb, which FWHM is 58". The Bragg angle of the GaSb peak" is almost identical to that of bulk (i.e. unstrained) GaSb.

4.2.2 Device design

For an energy-sensitive radiation detector, different design rules are required to be taken in to account in comparison to the detectors used in telecommunications. There are several considerations for the proposed design using heterostructure devices. First of all, a large difference in absorption efficiency between absorption and junction regions is desirable. With a much larger stopping power of GaSb, the detector would not only have a high absorption efficiency but also minimize the probability of signals created outside the absorption region. Besides, a large layer thickness ratio of the GaSb absorption region to the GaAs junction region is favorable. This can be achieved by either increasing the thickness of the absorption region or reducing that of the junction region. However, the junction region cannot be too thin since it would in turn increase the device capacitance, leading to undesired electronic noise. Furthermore, to obtain a high spectroscopic performance, the device requires a good charge collection efficiency. This includes

the charge transport within the absorption region and across the heterointerface between GaSb and GaAs, i.e. the IMF array. Finally, the electric field strength in the GaSb region needs to be maintained sufficiently low to minimize the field-assisted processes (e.g. field-enhanced SRH process, BTBT process, and impact ionization) to produce a low electronic noise and excess noise.

The schematics of the integrated device structure are shown in Fig. 4-2. The ratio of the active layer thickness of GaSb to GaAs is about 12, consisting of a 3.5 μm absorption region and a 300 nm junction region. The fabrication process of the GaSb/GaAs devices follows the similar steps as used in fabricating the GaSb PIN devices in chapter 3, except that the Ge/Ni/Ge/Au metal contact was deposited on the n-GaAs layer to form the ohmic contact after annealing. The identical photomask was used to create electrically isolated circular mesas. Since sulfuration has been reported to show effectively passivation to GaAs surfaces[18], the same sidewall surface passivation based on $(NH_4)_2S$ treatment was also employed.

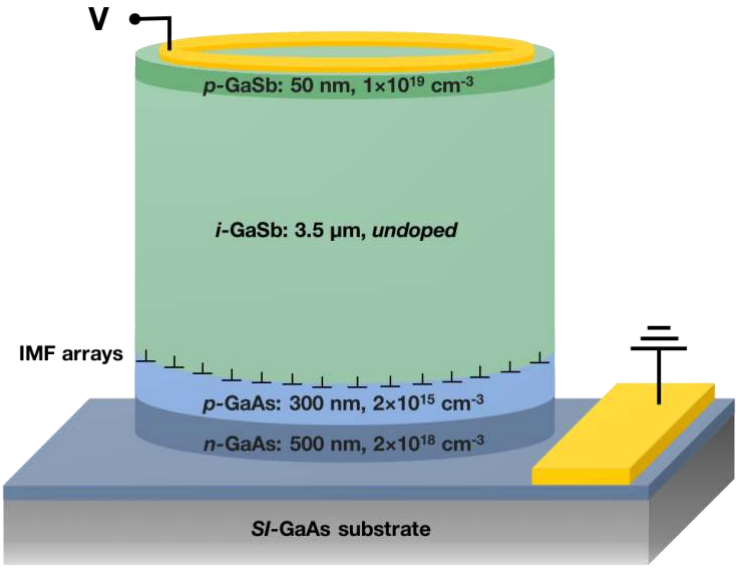

Figure 4-2 The GaSb/GaAs device structure with a 3.5 μm GaSb absorption region.

4.3 Electrical characterization

4.3.1 Device capacitance

The capacitance-voltage (C-V) measurement of the GaSb/GaAs devices with different size mesas are shown in Fig. 4-3. The scalable device capacitance indicates a good accuracy of the measurement. The device capacitance exhibits a minimal variation with increasing reverse bias, suggesting the GaAs junction region is already fully depleted at zero bias. In addition, the capacitance is expected to decrease continuously if the edge of the depletion region is located within the GaSb region. Thus, the trend of C-V curves reflects that the depletion width has maintained almost unaffected by the increasing reverse bias, suggesting that the electric fields are fully confined to the GaAs region.

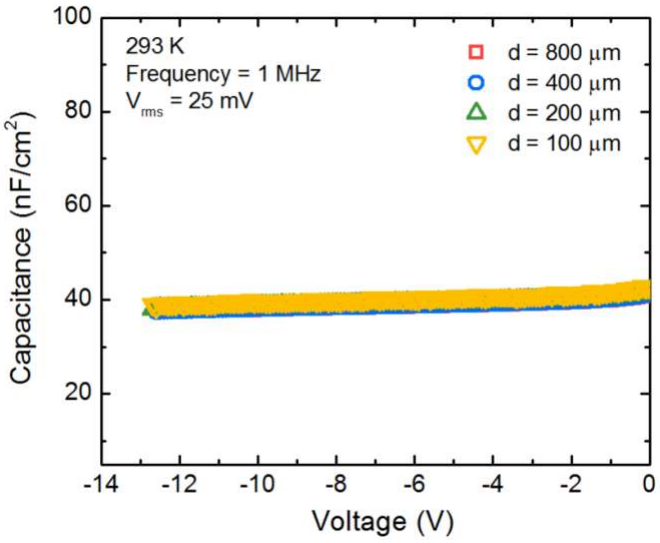

Figure 4-3 Room-temperature capacitance measurements of the GaSb/GaAs device structure with difference size mesas.

4.3.2 Dark current

The room-temperature dark current densities of the GaSb/GaAs devices with different size mesas are shown in Fig. 4-4. It is shown that the dark current has been improved by 2-3 orders of

magnitude after sidewall surface passivation using the $(NH_4)_2S$ solutions. In addition, the devices exhibit bulk-limited dark current for nearly the entire measurement range. At forward bias regime, the devices show an ideality factor of approximately 1.01 from 0.3 V to 0.4 V, suggesting a diffusion-limited current characteristic. At reverse bias, the dark currents are initially limited by the generation-recombination currents under reverse bias from 0 V to -5 V, followed by a gradual increase with increasing biases. The avalanche breakdown is established sharply around -12.8 V with little variation in breakdown voltages (V_{BD}) across devices with different sizes. The dark current density exhibits 15 $\mu A/cm^2$ at reverse bias of 90% V_{BD}, suggesting a 37-fold improvement in comparison to the previous reported value[11].

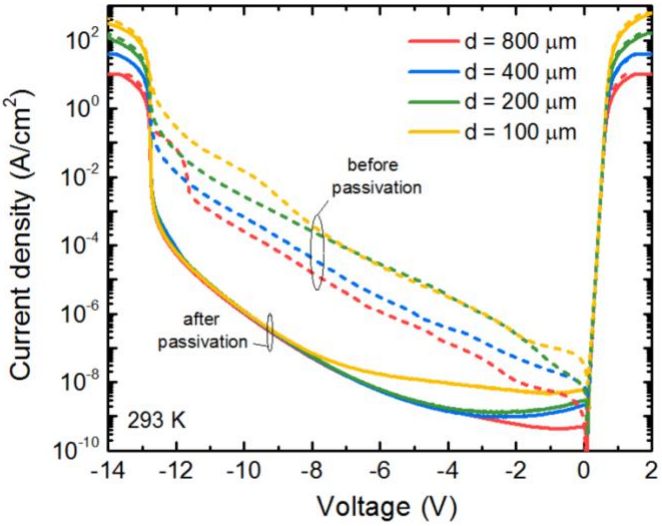

Figure 4-4 Room-temperature dark current measurements of the GaSb/GaAs detector structure with difference size mesas.

4.3.3 Activation energy

Fig. 4-5 shows the temperature-dependent measurement of a representative GaSb/GaAs device. The increased V_{BD} with increasing temperature, as shown in Fig. 4-5(a), indicates that the device breakdown is due to avalanche process instead of BTBT process, i.e., Zener breakdown.

The dark current at 90% V_{BD} was extracted and plotted with the Arrhenius equation as shown in Fig. 4-5(b). The activation energy extracted is approximately 230 meV, fairly close to the activation energy obtained previously with the GaSb PIN devices. The comparable activation energies of the GaSb/GaAs device and the GaSb PIN device suggest a likelihood that they are both resulting from the same mechanism, which is the $V_{Ga}Ga_{Sb}$ trap states in GaSb as discussed in chapter 3.

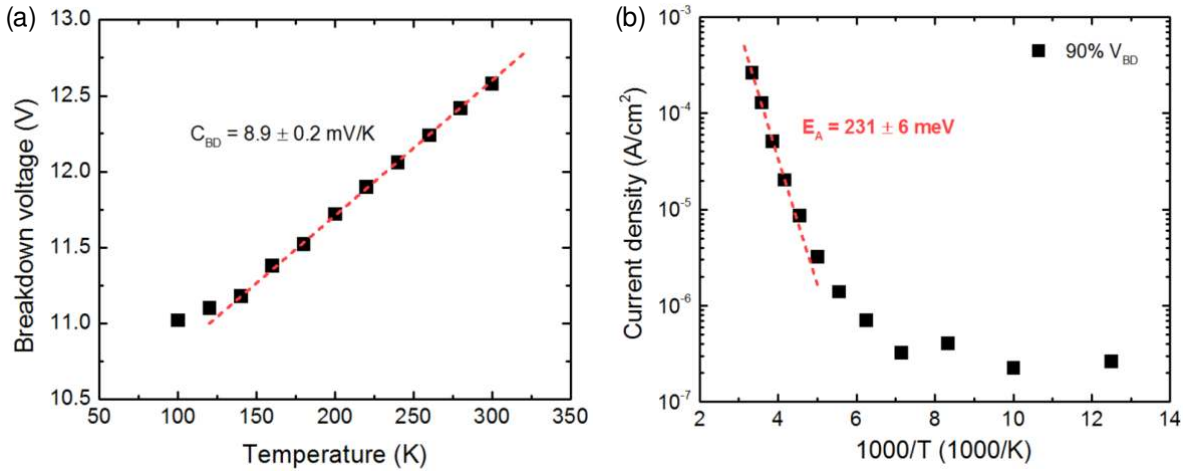

Figure 4-5 (a) Temperature-dependence of the breakdown behavior suggests the avalanche process with a coefficient of 8.9±0.2 mV/K, and (b) Arrhenius plot of dark current densities at 90% V_{BD}.

4.4 Optical characterization

4.4.1 Photocurrent and avalanche gain

The optical excitation using a laser emitted at 1064 μm is used for photocurrent measurement in order to exclude the optical absorption in the GaAs region. The GaSb/GaAs device shows a continuous increase in photocurrent with increasing reverse bias, whereas the photocurrent plateau commonly used as an indication for primary photocurrent at unity gain has not been observed. As a result, the primary photocurrent is decoupled from the total current, and it can be

best described using an empirical model based on an exponential function with reverse bias, as shown in Fig. 4-6. The exponential function is often used to describe the carrier transport behavior when a finite potential barrier is present and associated with an activation energy, e.g. Schottky barriers. The extracted avalanche gain curve is shown in Fig. 4-6, and the multiplication factor is also supported by the excess noise measurements as will be discussed in a later section. The device begins to exhibit avalanche gain from the reverse bias of about 5 V, and obtains a maximum gain of about 25 before V_{BD}.

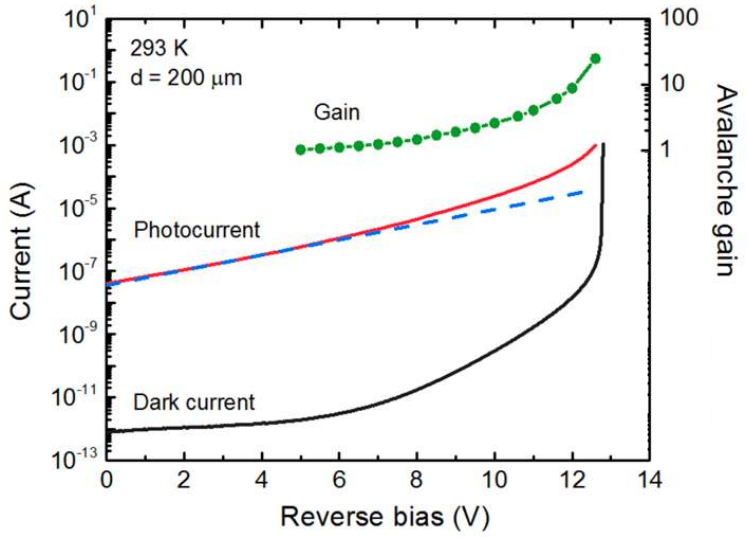

Figure 4-6 Measured photocurrent and fitted primary photocurrent (blue dotted line) of the 200-μm-diameter GaSb/GaAs device. The avalanche gain curve extrapolated by the excess noise measurement is also shown in the plot.

Combined with the observation of the device photoresponse and the C-V characteristics discussed in the previous section, we could conclude that there exists a potential barrier at the heterointerface that effectively limits the spreading of the electric field into the GaSb region to assist carrier collection. The exponential increase in primary photocurrent with reverse bias is likely due to the increased probability of the photogenerated carriers overcoming the potential barrier near the GaSb-GaAs interface induced by the IMF arrays.

4.4.2 Quantum efficiency

The device responsivity has been further measured using a 1.55 µm laser to achieve optical absorption of 93% in the 3.5-µm GaSb absorption region, and the calculated optical absorption efficiency is shown in Fig. 4-7. In addition, the 43% reflectance of the photon impinging on the device front surface was measured using FTIR, similar to that of the GaSb PIN devices. The internal quantum efficiency (IQE) of the GaSb/GaAs device can thus be calculated with the knowledge of the device EQE, reflectance and transmittance. Since there is a continuous increase in primary photocurrent, indicating the full carrier collection is not obtained before V_{BD}, the IQE is estimated as 2.8% based on the reverse bias at 90% V_{BD}.

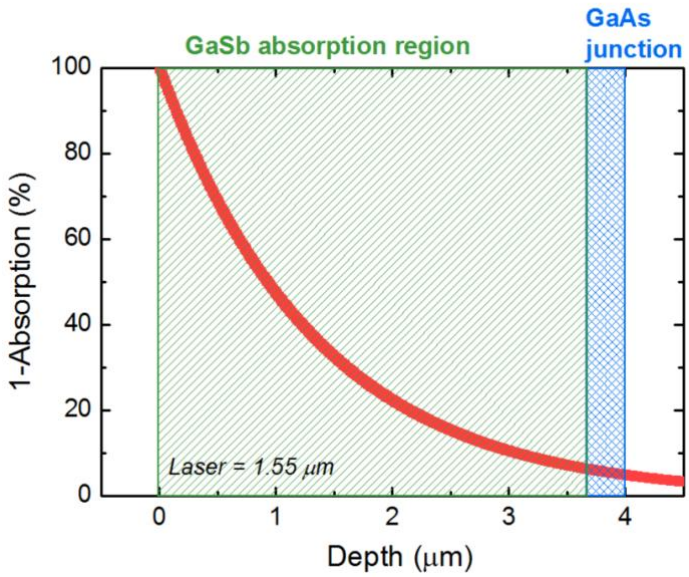

Figure 4-7 Absorption efficiency of photons at a wavelength of 1.55 µm penetrating into the GaSb/GaAs device structure.

4.4.3 APD excess noise

The APD excess noise measurement was performed in order to reliably extract the avalanche gain behavior of the GaSb/GaAs device and understand the device noise performance while operating in APD mode. It should be not confused with the excess noise component used in

describing the photopeak FWHM for the X-ray and gamma-ray spectroscopy. The 1064 nm laser is used for excitation with an optical power of 10 mW, and the readout circuit includes a DHPCA-100 variable gain transimpedance amplifier and a spectrum analyzer. Prior to measuring the GaSb/GaAs devices, the noise measurement setup was calibrated by measuring the noise power of an un-biased commercial InGaAs PIN device (at unity gain) by varying the optical excitation power as shown in Fig. 4-8(a). Three main noise current regimes can be clearly identified,

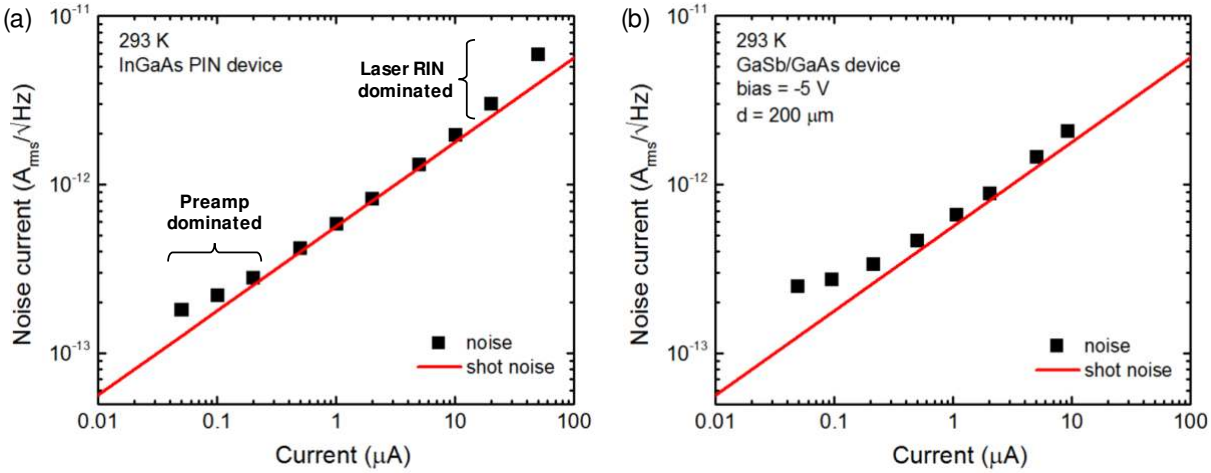

Figure 4-8 Noise current measurement of (a) an InGaAs PIN device and (b) a GaSb/GaAs device with varying excitation optical power.

including the preamplifier noise floor, device shot noise, and the laser relative intensity noise (RIN). The bandwidth-normalized shot noise of a semiconductor detector can be generally expressed as

$$i_{shot}^2 = 2qI_{bulk}M^2f + 2qI_{surf} \ , \tag{3.1}$$

where q is electric charge and I_{bulk} is the device bulk current including photogenerated current, M is the avalanche gain, f is the APD excess noise factor, and I_{surf} is the device surface current which is not to be multiplied. An accurate excess noise measurement can then be performed by carefully isolating the undesired noise sources and limiting the devices with the shot noise-limited

regime. Fig. 4-8(b) shows the repeated calibration measurement performed with a 200-µm-diameter GaSb/GaAs device, which is reverse biased at 5 V to ensure a negligible avalanche gain. The result of excess noise measurement as a function of avalanche gain is shown in Fig. 4-9, which follows the McIntyre formula[19],

$$f = k_{eff} \cdot M + \left(1 - k_{eff}\right)\left(2 - \frac{1}{M}\right), \tag{3.2}$$

where k_{eff} represents the effective ionization rate ratio of holes to electrons. The excess noise

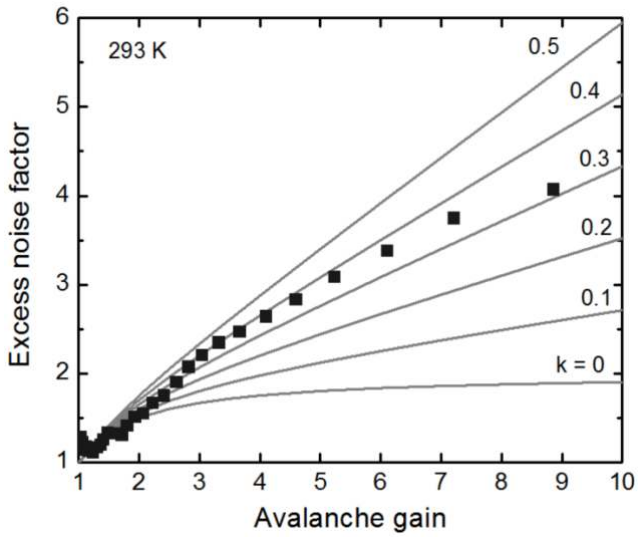

Figure 4-9 Excess noise factor as a function of avalanchve gain obtained by the GaSb/GaAs device.

factor of the GaSb/GaAs device fits in the trend of k_{eff} = 0.3-0.4, which agrees well to the previously reported GaAs PIN devices of similar multiplication thickness reported by Hu et al.[12]. This also indicates that the electric field distribution is the same as designed within the 300-nm-thick GaAs region.

For energy-sensitive radiation detectors, the effect of APD excess noise factor f can also be included as[20–22]

$$FWHM\ (eV) = 2.355 \cdot \varepsilon \cdot \sqrt{\frac{E}{\varepsilon}(f + F - 1) + \Delta E_{elec}^2 + \Delta E_{ex}^2}\ , \tag{3.3}$$

considering the additional fluctuation caused by the distribution of APD gain statistics. While the avalanche gain provided by the detector is shown to offer internal charge amplification with enhanced signal strength, the side-effect of APD excess noise could also introduce additional carrier fluctuation leading to a potentially compromised signal-to-noise (SNR) ratio. However, Tan et al. have reported the results of a series of simulations using a modified Monte Carlo-based random path length (RPL) model[22] and suggested that an APD with low k_{eff} could still be beneficial for radiation detectors. Since high-energy radiations create more than one carrier per photon, the increased number of carriers has been predicted to produce a narrower distribution of gain statistics, which effectively generates less carrier fluctuation as predicted by Eq. 3.2.

4.5 X-ray and gamma-ray response

4.5.1 Electronic noise calibration

The selected GaSb/GaAs devices were wire-bonded onto a TO-header to perform the radiation measurement. The measurement was carried out at room-temperature with a representative 200-µm-diameter device, and the readout electronics includes the A250CF preamplifier (JFET C_i = 8 pF), the shaping amplifier, and the multichannel analyzer. Fig. 4-10 shows the electronic noise as a function of reverse bias, measured by the pulser with a shaping time of 1 µs. The noise floor of the measurement system limit (i.e. electronic noise without the

device connected) is also shown. The pulser FWHM maintains relatively unchanged from the reverse bias of 0 V to 10 V since the dark current of the device is sufficiently low in comparison to the noise current of the preamplifier. With increasing reverse bias beyond 10 V, the dark current increases significantly leading to excess broadening of the pulser FWHM.

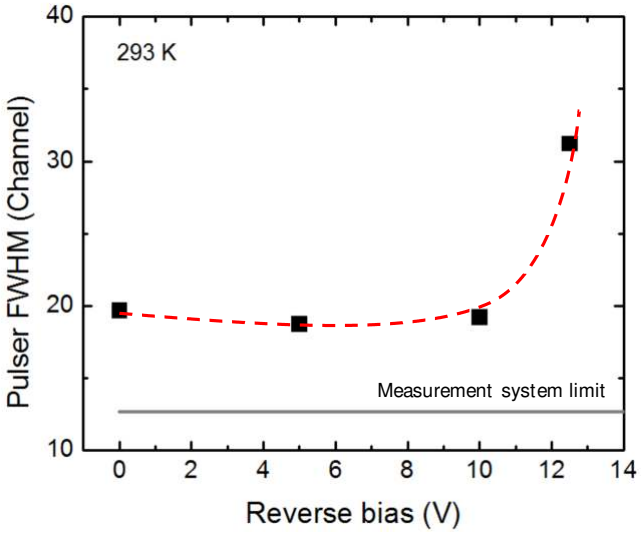

Figure 4-10 Pulser FWHM at the MCA output as a function of reverse bias. The dashed line shows the measurement system limit at a shaping time of 1 μs.

4.5.2 ^{241}Am spectra

Fig. 4-11 shows the ^{241}Am spectra obtained using the 200-um-diameter GaSb/GaAs heterostructure device and the reference GaAs PIN device as used in chapter 3. Both devices were carefully reverse biased to ensure the absence of avalanche gain. The spectrum obtained using the GaSb/GaAs device shows signature energy lines from the 1.44 MBq ^{241}Am source, and the photopeaks at 13.9 keV, 17.8 keV, and 20.8 keV can be identified albeit with a relatively poor resolution, as shown in Fig. 4-11(a). Same energy lines can be clearly observed in the spectrum generated by the reference GaAs PIN device. The high similarity between the two spectra suggests that the measured photopeaks are created by the same material, i.e., the GaAs region, rather than

the intended GaSb absorption region for the GaSb/GaAs device. This could be due to a relatively small carrier collection efficiency at low reverse bias. To further increased the carrier collection efficiency, the ^{241}Am spectrum was also recorded with an increased reverse bias of 12.6 V, where an avalanche gain of 25 is anticipated based on the laser measurement. Indeed, the obtained

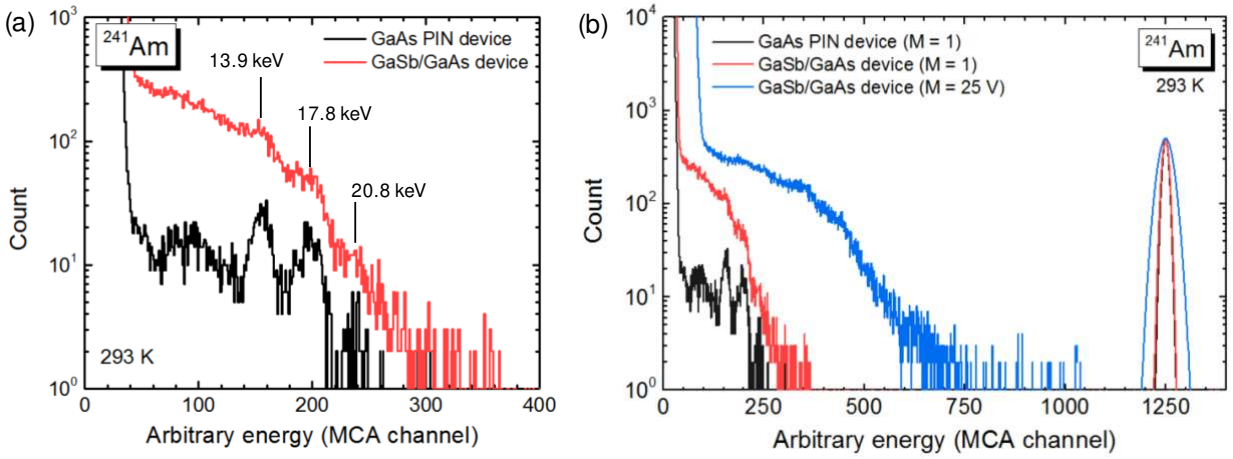

Figure 4-11 (a) ^{241}Am spectra obtained by the reference GaAs PIN device and the GaSb/GaAs device at unity device gain, and (b) the spectra generated by the GaSb/GaAs device at a reverse bias of 12.6 V.

spectrum exhibits signals appeared at much larger channels, as shown in Fig. 4-11(b). However, the combined effect of enhanced carrier collection and increased avalanche gain from 5 V to 12.6 V is expected to produce a more significant increase (by orders of magnitude) if the signals are generated from the GaSb region (Fig. 4-6). It can be seen in Fig. 4-11(b) that the measured channel offsets suggest an improvement much smaller than expected. This could indicate that the obtained signals are irrelevant to the GaSb region, and the increased signal strength is likely due to avalanche process of carriers generated in the GaAs region.

4.6 Discussion

4.6.1 Absence of signals from GaSb

The photopeaks created by the GaSb region, if any, were expected to take place at larger MCA channels with a greater number of counts in comparison to those form the GaAs region, owing to the large difference in PCE and stopping power between two materials. However, the radiation response from the GaSb region was not observed. The absence of signals generated in the GaSb region could be primarily due to two possibilities: (1) significant carrier loss occurred in the GaSb region, and (2) ineffective carrier transport at the GaSb-GaAs interface.

The loss of photogenerated carriers can be a result of large density of defects existed in the GaSb region. The defects could effectively lead to rapid SRH recombination or carrier trapping. The GaSb devices grown on GaAs substrates using IMF arrays have been reported to show a relatively high SRH recombination rate (i.e. short carrier lifetime) than that on GaSb substrates due to a finite number of threading dislocations; however, the IMF-based devices also exhibit a reasonable carrier collection efficiency and are capable of producing detector-grade performance[12,13]. As a result, we would still anticipate to observe photopeaks from signals created by the GaSb region that registered at larger MCA channels. In addition, the GaSb/GaAs device is expected to have an enhanced carrier transport in the GaSb region with increasing reverse bias, resulting in an improved carrier collection efficiency. However, the above discussion is not supported by the experimental results, suggesting that (1) is not likely the dominant factors responsible for the absence of photopeaks generated in the GaSb region.

Another possibility is the potential barrier presented at the GaSb-GaAs interface, which can effectively hinder the collection of carriers generated in the GaSb region. The 90º misfit

dislocation arrays are associated with a finite density of acceptor states due to Ga dangling bonds (on the order of 10^{12} cm^{-2})[9], and the formation of the potential barrier is likely due to the Fermi level pinning at the GaSb-GaAs interface[23]. Similar charged states have been observed in other mismatched material systems, such as Si/SiGe, GaAs/Si, InGaP/GaAs, and InGaAs/InP, which interface charges have somewhat affected the carrier transport to various degrees[24–27]. Nonetheless, the carrier transport properties in the aforementioned heterostructure devices are commonly observed to show effective improvement once the interface charges have been depleted with increasing voltage potential. Even though we have observed a continuous improvement in the carrier collection, as indicated by the primary photocurrent in Fig. 4-6, the depletion of interface charges may not be sufficient to completely eliminate the effect of the potential barrier. This can be supported by the experimental C-V curves as shown in Fig. 4-3, where the depletion region maintains almost fully confined to the GaAs region until V_{BD}.

4.6.2 Photopeak offset with reverse bias

The deviation of obtained photopeak offsets at a large reverse bias from the expected avalanche gain can be interpreted as follows. The gain curve in Fig. 4-6 is characterized based on carriers purely generated in the GaSb region. As a result, the observed avalanche behavior represents the average impact ionization of carriers experiencing nearly the same electric field profile, starting from the GaSb-GaAs interface. On the other hand, if the carriers were generated inside the GaAs region, they would undergo very different impact ionization processes depending on the locations in which they were generated[28]. The average gain factor would then be determined by those impact ionization events taking place inside the GaAs region, which effectively produces a wider spread of gain statistics. In this case, the measured gain factor becomes an average value of a relatively broad distribution in comparison to the case that carriers are injecting from the GaSb

region. As a result, the relatively small degree of photopeak offset is considered as a result of the modified (i.e. reduced) avalanche gain factors. In addition, the degraded spectroscopic performance is likely due to the increased fluctuation in the number of collected carriers[28].

4.6.3 Alternative solutions

The potential barrier induced by the IMF arrays has been concluded as a main cause of the ineffective carrier collection in the GaSb/GaAs device structures. The use of the delta-doping technique has been studied to provide a way to compensate the acceptor states at the GaSb-GaAs interface[23,29]. Reyner et al. have shown that the collection efficiency of the IMF-based devices using compensational delta-doping technique can be considerably improved but at the expense of a proportional increase in dark current level. The trade-off between two performance metrics inevitably places a stringent limit to the attainable SNR in radiation detection since the energy-sensitive radiation detectors are operating in DC mode.

On the other hand, using a different large-bandgap material to replace GaAs could provide an alternative solution. AlAsSb alloy is found to be a promising candidate in the III-Sb material family. It can be grown lattice-matched to GaSb, and the alloy possesses a low effective Z to minimize the undesired absorption outside the intended absorption region. AlAsSb alloy also has the largest bandgap available in Sb-based semiconductors. In the following chapters, the development of the integrated device architecture will be focused on using the GaSb/AlAsSb material system.

4.7 Reference

1. Mingguo, L. *et al.* Low Dark Count Rate and High Single-Photon Detection Efficiency Avalanche Photodiode in Geiger-Mode Operation. *Photonics Technol. Lett. IEEE* **19,** 378–380 (2007).

2. Namekata, N., Sasamori, S. & Inoue, S. 800 MHz Single-photon detection at 1550-nm using an InGaAs/InP avalanche photodiode operated with a sine wave gating. *Opt. Express* **14,** 10043–10049 (2006).

3. Ong, D. S. G., Hayat, M. M., David, J. P. R. & Ng, J. S. Sensitivity of High-Speed Lightwave System Receivers Using InAlAs Avalanche Photodiodes. *Ieee Photonics Technol. Lett.* **23,** 233–235 (2011).

4. Meng, X., Tan, C. H., Dimler, S., David, J. P. R. & Ng, J. S. 1550 nm InGaAs/InAlAs single photon avalanche diode at room temperature. *Opt. Express* **22,** 22608–22615 (2014).

5. Campbell, J. C. Recent Advances in Telecommunications Avalanche Photodiodes. *J. Light. Technol.* **25,** 109–121 (2007).

6. Carroll, M. S., Childs, K., Jarecki, R., Bauer, T. & Saiz, K. Ge–Si separate absorption and multiplication avalanche photodiode for Geiger mode single photon detection. *Appl. Phys. Lett.* **93,** 183511 (2008).

7. Warburton, R. E. *et al.* Ge-on-Si Single-Photon Avalanche Diode Detectors: Design, Modeling, Fabrication, and Characterization at Wavelengths 1310 and 1550 nm. *IEEE Trans. Electron Devices* **60,** 3807–3813 (2013).

8. Kang, Y. *et al.* Epitaxially-grown Ge/Si avalanche photodiodes for 1.3μm light detection. *Opt. Express* **16,** 9365–9371 (2008).

9. Huang, S. H. *et al.* Strain relief by periodic misfit arrays for low defect density GaSb on GaAs. *Appl. Phys. Lett.* **88,** (2006).

10. Jallipalli, A. *et al.* Atomistic modeling of strain distribution in self-assembled interfacial misfit dislocation (IMF) arrays in highly mismatched III–V semiconductor materials. *J. Cryst. Growth* **303,** 449–455 (2007).

11. Craig, A. P., Reyner, C. J., Marshall, A. R. J. & Huffaker, D. L. Excess noise in GaAs and AlGaAs avalanche photodiodes with GaSb absorption regions-composite structures grown using interfacial misfit arrays. *Appl. Phys. Lett.* **104,** (2014).

12. Nunna, K. C. *et al.* Short-Wave Infrared GaInAsSb Photodiodes Grown on GaAs Substrate by Interfacial Misfit Array Technique. *Photonics Technol. Lett. IEEE* **24,** 218–220 (2012).

13. Juang, B.-C. *et al.* GaSb thermophotovoltaic cells grown on GaAs by molecular beam epitaxy using interfacial misfit arrays. *Appl. Phys. Lett.* **106,** 111101 (2015).

14. Plis, E. *et al.* Mid-infrared InAs/GaSb strained layer superlattice detectors with nBn design grown on a GaAs substrate. *Semicond. Sci. Technol.* **25,** 85010 (2010).

15. Craig, A. P., Marshall, A. R. J., Tian, Z. B. & Krishna, S. Mid-infrared InAsSb-based nBn photodetectors with AlGaAsSb barrier layers – Grown on GaAs, using an interfacial misfit array, and on native GaSb. *Infrared Phys. Technol.* **67,** 210–213 (2014).

16. Jallipalli, A. *et al.* Structural Analysis of Highly Relaxed GaSb Grown on GaAs Substrates with Periodic Interfacial Array of 90degrees Misfit Dislocations. *Nanoscale Res. Lett.* **4,** 1458–1462 (2009).

17. Reyner, C. J. *et al.* Characterization of GaSb/GaAs interfacial misfit arrays using x-ray diffraction. *Appl. Phys. Lett.* **99,** (2011).

18. Carpenter, M. S., Melloch, M. R., Cowans, B. A., Dardas, Z. & Delgass, W. N. Investigations of ammonium sulfide surface treatments on GaAs. *J. Vac. Sci. Technol. B Microelectron. Process. Phenom.* **7,** 845–850 (1989).

19. McIntyre, R. J. Multiplication noise in uniform avalanche diodes. *IEEE Trans. Electron Devices* **ED-13,** 164–168 (1966).

20. Knoll, G. F. *Radiation detection and measurement*. (John Wiley & Sons, 2010).

21. Fernandes, L. M. P. *et al.* Characterization of large area avalanche photodiodes in X-ray and VUV-light detection. *J. Instrum.* **2,** P08005 (2007).

22. Chee Hing Tan *et al.* Avalanche Gain and Energy Resolution of Semiconductor X-ray Detectors. *IEEE Trans. Electron Devices* **58,** 1696–1701 (2011).

23. Jallipalli, A. *et al.* Compensation of interfacial states located inside the 'buffer-free' GaSb/GaAs (001) heterojunction via δ-doping. *Appl. Phys. Lett.* **95,** (2009).

24. Nauka, K. *et al.* Admittance spectroscopy measurements of band offsets in Si/Si1−xGex/Si heterostructures. *Appl. Phys. Lett.* **60,** 195–197 (1992).

25. Won, T., Munns, G., Houdré, R. & Morkoç, H. Interface charge polarity of a polar on nonpolar semiconductor GaAs/Si with Ga and As prelayers. *Appl. Phys. Lett.* **49,** 1257–1259 (1986).

26. Cai, C., Nathan, M. I. & Lim, T. H. Characterization of the inverted Ga0.52In0.48P/GaAs (001) junctions using current–voltage and capacitance–voltage measurements. *Appl. Phys. Lett.* **74,** 720–722 (1999).

27. Lang, D. V *et al.* Measurement of heterojunction band offsets by admittance spectroscopy: InP/$Ga_{0.47}In_{0.53}As$. *Appl. Phys. Lett.* **50,** 736–738 (1987).

28. Gomes, R. B., Chee Hing, T., Lees, J. E., David, J. P. R. & Jo Shien, N. Effects of Dead Space on Avalanche Gain Distribution of X-Ray Avalanche Photodiodes. *Electron Devices, IEEE Trans.* **59,** 1063–1067 (2012).

29. Reyner, C. GaSb-based Infrared Detectors on GaAs Substrates using an Interfacial Misfit Array. (2013).

5. Development of AlAsSb alloy

5.1 Background

The key technical merit of the proposed research lies in the integration of high-Z, small-bandgap GaSb that is ideally suited for gamma-ray absorption region, with a low–Z, large-bandgap material that is better suited for the high electric field region in a single device architecture. The GaSb/GaAs material system was first developed and studied using such device design, because of their relatively mature material and fabrication knowledge. However, the device characterization has suggested that the challenges remain in ineffective carrier collection due to the potential barrier created by the charge sheet at the mismatched GaSb-GaAs interface. An alternative solution is proposed to adopt another large-bandgap material that can be grown lattice-matched to GaSb to replace GaAs for the junction region.

The AlAsSb alloy has been considered as a promising material candidate, which has the largest bandgap available in the AlGaAsSb family that can be grown lattice-matched to GaSb (Fig. 5-1). In addition, the availability of various ternary and quaternary alloys in the same material family could enable flexible bandgap engineering in the future device design. AlAsSb alloy has also drawn considerable attention recently to the infrared detector communities. For example, AlAsSb has been discovered to exhibit superior electrical properties as the multiplication region in comparison to InP in the InGaAs/InP APDs[1,2]. The APD excess noise of the AlAsSb introduced by the avalanche process has been reported to be as low as Si[2–4]. In addition, the large indirect bandgap of AlAsSb (>1.5 eV at room temperature) also suggests a reduce dark current floor, which holds a great potential for realizing the concept of proposed energy-sensitive radiation detectors.

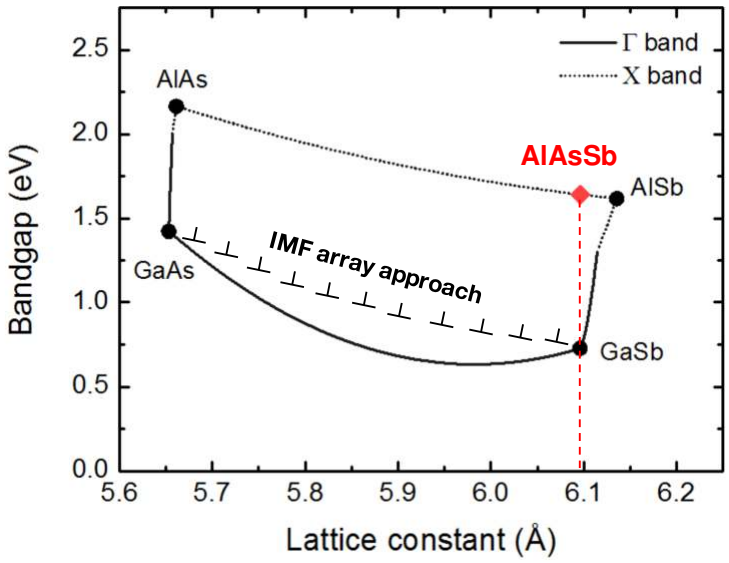

Figure 5-1 Diagram of semiconductor bandgap and lattice-constant for the GaSb/GaAs and GaSb/AlAsSb systems.

To produce such mixed-anion alloys, the epitaxy traditionally relies on random-alloy (RA) growth, which utilizes direct deposition of different elements on the sample surface with carefully tuned growth parameters, such as substrate temperature, growth rate, group V flux ratio, etc., to achieve the targeted alloy composition. Unfortunately, due to non-unity incorporation coefficient of volatile group V elements, the epitaxy of mixed-anion alloys is much more complicated than that of alloys with only one group V element. The wide miscibility gap of these alloys can easily create undesired crystalline disorders, e.g., As/Sb clusters and phase separation[5,6]. As an alternative, Zhang has proposed modulated molecular beam epitaxy (MMBE)[7], as known as the digital-alloy (DA) growth, for III-(As, Sb) ordered alloys. The DA growth has been shown to offer a precise control over alloy composition and reproducibility against RA growth[8,9]. This technique has also been widely implemented in facilitating growths of different III-(As, Sb) alloys in device applications[10–13].

This chapter is dedicated to providing a detailed analysis of the lattice-matched $AlAs_{0.08}Sb_{0.92}$ (AlAsSb hereafter) DA and RA grown on GaSb. The material characterization of the DA and the RA samples is studied by comparing their heterointerfaces, optical characteristics, and minority carrier lifetimes. In addition, the AlAsSb PIN devices are fabricated to measure their electrical and optical characteristics. The device performance in terms of dark current, activation energy, and spectral response is compared and discussed. Furthermore, the radiation response of the AlAsSb DA device is reported, which provides important information for constructing the platform for the integrated energy-sensitive radiation detector structure.

5.2 Material characterization

5.2.1 Sample growth

The AlAsSb alloys were grown on GaSb (001) substrates by MBE. Separate growth campaigns of DA and RA samples were conducted in order to obtain the lattice-matching composition, characterized using peak separation from the XRD measurements. The DA sample was realized by modulating the As and Sb shutter sequence while maintaining a steady Al flux during deposition, resulting in AlSb/AlAs equivalent sequence of 4.0/0.8 MLs. Additional 4.0 MLs of AlSb was used prior to the transition to GaSb cap layer. On the other hand, the RA sample was grown by keeping Al, As, and Sb shutters open simultaneously, followed by the GaSb layer without growth interruption. The two samples were kept with the identical layer structure and minimal difference in alloy composition to enable a fair comparison, as shown in Fig. 5-2. The growth detail can be found in Appendix C.

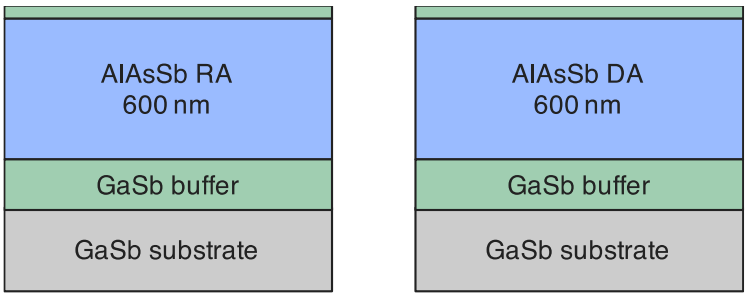

Figure 5-2 The sample structure of AlAsSb alloys for material characterization.

5.2.2 XRD measurement

The HRXRD ω-2θ scans of the AlAsSb DA and RA samples exhibit a single peak of the epitaxial layers, inseparable from the GaSb substrate peak, as shown in Fig. 5-3. The full-width-at-half-maximum (FWHM) values are 18 arcsec and 21 arcsec for the AlAsSb DA and RA sample, respectively, comparable to that of 16 arcsec for the GaSb substrate. It is clearly shown that the epitaxial layers are lattice-matched to the substrates and the compositional fluctuation is negligible.

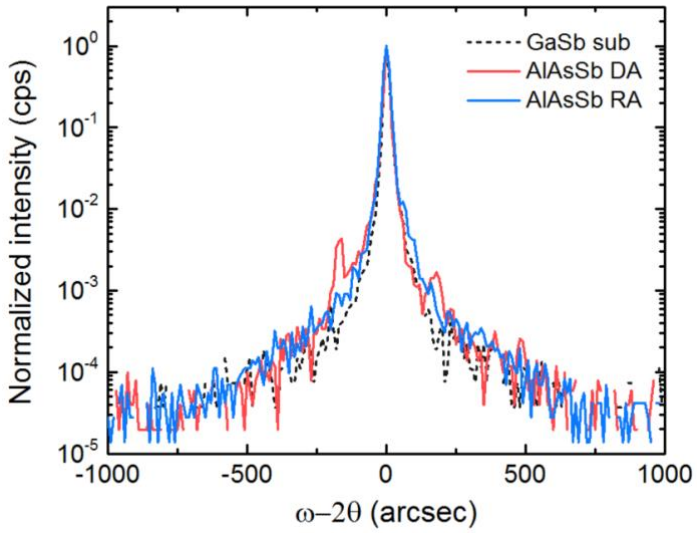

Figure 5-3 HRXRD ω-2θ scans for the DA and RA samples. The GaSb substrate reference scan is also show in dashed line.

5.2.3 Microscopic characterization

The cross-section TEM of the AlAsSb DA and RA samples are shown in Fig. 5-4. Both samples exhibit ordered phase in AlAsSb based on the presence of the satellite spots in the electron diffraction pattern. The DA sample exhibits no sign of phase separation in the AlAsSb film, as shown in Fig. 5-4(a), and the alternating shutter sequence does not produce modulated contrast as found in superlattice growth (Fig. 5-4(c)). On the other hand, the bulk part of the AlAsSb film in the RA sample is also uniform, whereas a relatively rough GaSb-AlAsSb interface is observed in comparison to the DA sample (Fig. 5-4(d)). Some bright contrast features parallel to the growth front has been found in the RA sample, likely related to the sample preparation.

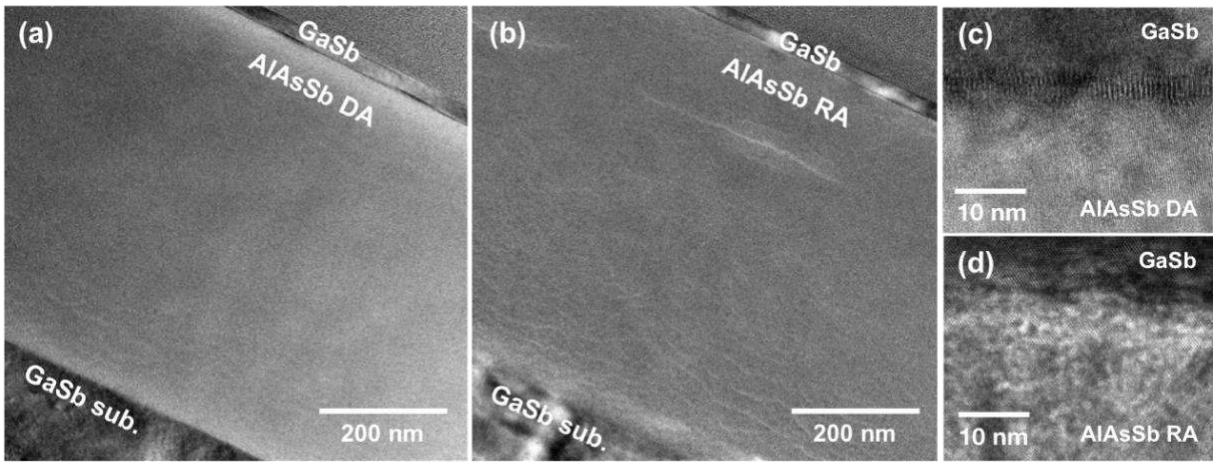

Figure 5-4 Cross-section TEM images for the AlAsSb (a) DA and (b) RA samples, and (c-d) show the HRTEM images of the GaSb-AlAsSb interfaces.

Atomic force microscopy (AFM) are commonly used to reveal surface morphology, provide feedback to epitaxial growth, and sometimes identify possible defects. Here, surface morphology of DA and RA samples both exhibit monolayer steps with small surface roughness, as shown in Fig. 5-5, indicating smooth 2-D layer growth at the substrate temperature. The surface of DA sample shows denser terraces than the RA sample, accompanied with several concentric

mounds (estimated ~2×10^6 cm^{-2}). The concentric mounds also appeared on the RA sample surface with a somewhat lower density (~1×10^6 cm^{-2}), and are considered as a result of the island-growth mode found in most of the Sb-based material epitaxy[14–16].The difference of the terrace step size may be due to slightly less Sb over pressure during the RA sample growth[17].

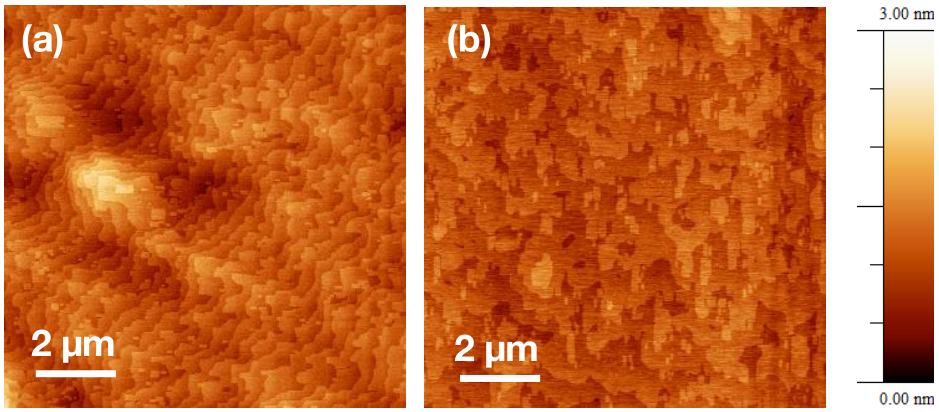

Figure 5-5 AFM 10×10 μm^2 images of the AlAsSb (a) DA and (b) RA samples with surface roughness or 0.276 nm and 0.236 nm, respectively.

5.2.4 Photoluminescence

A 532-nm solid-state laser has been used to probe and investigate the optical quality of the AlAsSb DA and RA samples. The absorption coefficient of AlAsSb can be linearly interpolated from that of AlAs[18] and AlSb[19], and the approximated absorption coefficient is 5.25×10^4 cm^{-1} which is about 10-fold smaller than that of GaSb, as shown in Table 5-1. In addition, the GaSb capping layer near front surface has been found to absorb more than 50% of incident light intensity owing to its strong absorption at the given wavelengths.

Low-temperature photoluminescence (PL) spectra of the DA and RA samples are shown in Fig. 5-6. Both spectra show similar features, including an anomalous emission around 1.29 eV (DL), a narrow peak at 1.6 eV (E^X), and a side band peaking around 1.84 eV (E^Γ) which can be seen more clearly in Fig. 5-6(b). In general, the DA sample exhibits stronger luminescence than

Material	α at 532 nm (cm^{-1})
GaSb	4.17×10^{5}
AlAs	1.17×10^{2}
AlSb	5.71×10^{4}
$AlAs_{0.08}Sb_{0.92}$	5.25×10^{4}

Table 5-1 The absorption coefficient of the GaSb, AlAs[18], AlSb[19], and AlAsSb at the excitation laser wavelength.

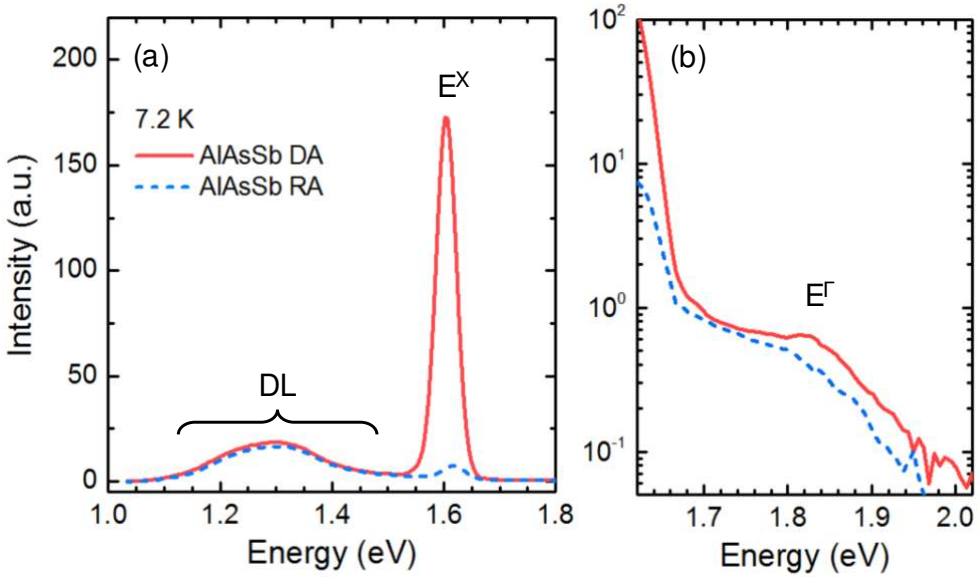

Figure 5-6 (a) Low-temperature PL spectra of the AlAsSb DA and RA samples at 7.2 K, and (b) shows the Γ-band emissions with logarithmic scale.

the RA sample with a considerable difference for the E^X peak. The PL peaks located at higher energies are most likely due to band-to-band transition. For an indirect-bandgap material, the low-temperature optical transition is known to be dominated by the indirect bands, i.e., X-band in AlAsSb. Following these rules, we identified the strong emission at 1.6 eV as the carrier recombination from the X-band, and the side band peaking at 1.84 eV is likely due to the transition

from the Γ-band. In Fig. 5-7(a), temperature-dependent E^X peak energies are fitted with a hyperbolic cotangent relation[20],

$$E_g(T) = E_g(0) - S\langle\hbar\omega\rangle\left(coth\left(\frac{\langle\hbar\omega\rangle}{2k_BT}\right) - 1\right), \tag{4.1}$$

where $E_g(0)$ is the bandgap energy at 0 K, S is the dimensionless coupling coefficient, $\langle\hbar\omega\rangle$ is the average phonon energy, and k_B is the Boltzmann constant. The fitting parameters are shown in Table 5-2. The fittings show good agreement with the experimental data, and the extracted values of $\langle\hbar\omega\rangle$ also match the calculated optical phonon energies[21]. The DA sample also exhibits a smaller bandgap energy than the RA sample, likely due to the ordering effect[22]. Similar results have been observed in other quaternary materials which DA growths exhibits relatively small bandgap within 2-3% to that of the RA growth[9,23]. On the other hand, the DL peaks display an anomalous temperature dependence with respect to the E^X peak, which will be discussed later.

Sample	$E_g(0)$	S	$\langle\hbar\omega\rangle$
AlAsSb DA	1.602 eV	4.89	38.1±3.4 meV
AlAsSb RA	1.619 eV	3.00	32.3±9.2 meV

Table 5-2 Extracted material parameters by fitting experimental data of the AlAsSb DA and RA samples.

Temperature-dependent FWHM of the E^X peak for both samples are shown in Fig. 5-7(b), and they are anticipated to be relatively large due to the involvement of multiple phonons in the indirect band transition. However, the DA sample does not exhibit broader PL emission as shown in as-grown AlGaInP system[23], suggesting no sign of defects that originated from large numbers of interfaces. The FWHM is approximately the same (40-45 meV) at low temperatures (<40 K),

whereas the DA sample has shown consistently smaller FWHM than the RA sample at elevated temperatures, suggesting a superior crystalline quality.

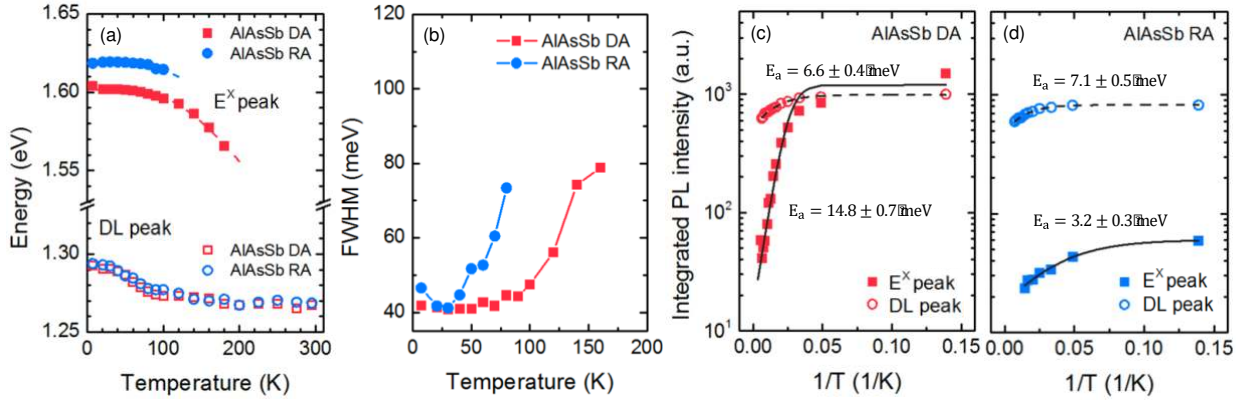

Figure 5-7 Temperature-dependent measurements of (a) photon energies, (b) peak FWHM, and (c) integrated PL intensity of the E^X peak and the DL peak for the AlAsSb samples.

Integrated PL intensities of the E^X and the DL peaks are studied and shown in Fig. 5-7(c-d). It can be seen that the E^X peak intensities drop quickly below 40 K with increasing temperature. In spite of the similar temperature-dependence of the DL peak among the DA and the RA samples, a marked difference in the E^X peak can be observed. The activation energies of the E^X peak can be extracted using Arrhenius equation[24],

$$I(T) = \frac{I_0}{1 + C_0 exp(-E_a/k_B T)} \tag{4.2}$$

where I_0 is the integrated intensity at 0 K, C_0 is the rate constant, and E_a is the activation energy. The E^X peak shows a much higher activation energy for the DA sample than the RA sample, suggesting that the carrier quenching process is much faster in the RA sample. The loss of carriers is likely due to phonon scattering assisted by crystalline disorders such as phase separation during the RA growth. In addition, the non-uniformity of alloy composition could also enhance non-

radiative recombination. On the other hands, the similar activation energies of the DL peaks indicate a common mechanism, regardless of the growth methods.

The origins of photon emission have been characterized using the power law, $I \propto P^k$, where I is the integrated PL intensity and the exponent k is a characteristic coefficient. The fitted k value depends on the radiative recombination mechanisms, where an exciton transition usually gives $1 < k < 2$ and transitions due to free-to-bound or donor-acceptor pair recombination give $k < 1$[25–27]. In Fig. 5-8(a), fitting the data to the E^X peak exhibits k = 1.22 and 1.3 for the DA and the RA samples, respectively, confirmed the transition is dominated by the band-to-band recombination as discussed earlier. On the other hand, fitting to the DL peak for both samples yield k = 0.66 and 0.71 for the DL and the RA samples, respectively, suggesting that the radiative

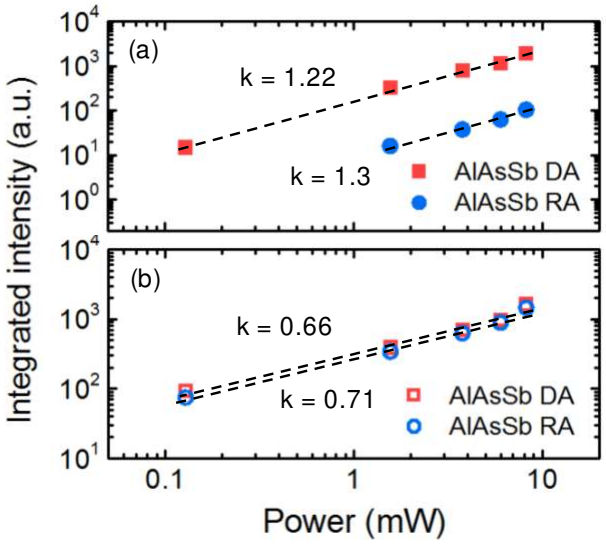

Figure 5-8 PL peak energies of (a) the E^X peak and (b) the DL peak for both the DA and the RA samples as a function of excitation optical power.

recombination involved states located within the bandgap. The appearance of the low-energy DL peak is common to both samples, regardless of the growth methods, and it is present at all temperatures studied which exhibits a relatively weak temperature dependence of the peak

energies and integrated PL intensities, as shown in Fig. 5-7. As a result, the DL peak could presumably be associated with unresolved transitions from deep level states in AlAsSb[28].

5.2.5 Time-resolved photoluminescence

Time-resolved PL (TRPL) decay from the E^X peak transition of the DA and the RA samples are measured and pumped under the same excitation power, as shown in Fig. 5-9, pumped under the same excitation power. The decay tails of both samples are best fitted using a single exponential function[29],

$$I(T) = A_0 + A_1 \exp(-t/\tau) \tag{4.3}$$

where $I(T)$ is the counted PL intensity, A_0 and A_1 are fitting parameters, and τ is the carrier lifetime. The instrument response function (IRF) is also shown as a reference for the system time

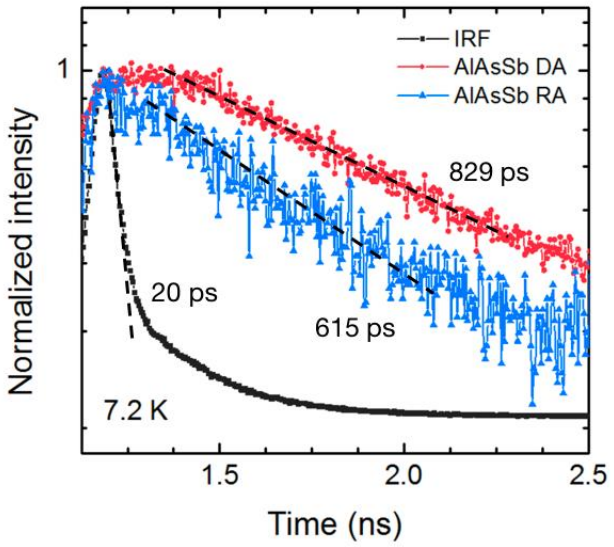

Figure 5-9 The TRPL data for the DA and RA samples of E^X transition at 7.2 K. The IRF of the measurement system is also shown in the same plot.

resolution. The DA sample shows a longer carrier lifetime in comparison to the RA sample, providing further evidence that the sample has less density of non-radiative recombination centers.

5.3 Electrical characterization

5.3.1 Device design and fabrication

Two device samples using AlAsSb DA and RA growths were developed to further understand their electrical properties. The simple PIN structure design was used (Fig. 5-10), with a 280-nm i-region sandwiched by heavily doped p- and n-type layers. The i-region is lightly doped with Be in order to ensure the desired n^+-p^--p^+ doping profile, and the metallization for both device contacts were made on the GaSb layers. The AlAsSb DA and RA device samples are fabricated using standard photolithography as conducted in the previous chapters. Since the AlAsSb alloy is known to produce an extremely reactive surface with rapid oxidization rate, different fabrication methods were studied, including mesa etching and surface passivation, in an attempt to obtain the optimized surface condition.

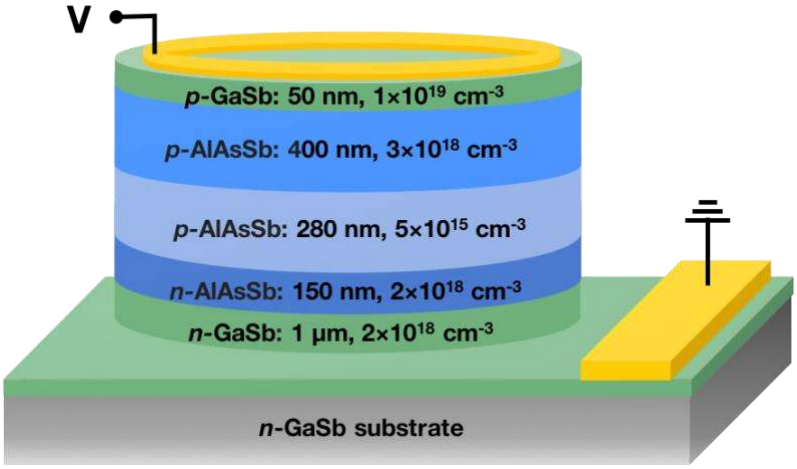

Figure 5-10 The AlAsSb PIN device structure with a 280 nm i-region.

The definition of device mesas was approached by dry-etching and wet-etching methods. Dry-etched device samples were achieved by using the inductively coupled plasma etcher (BCl_3/Ar), and wet-etched device samples were achieved by using a mixture of citric acid, H_2O_2, and HF solution (10:5:0.01). Since the electrical characteristics were not clearly revealed in the as-

fabricated devices, the dark current density curves of the device samples are compared with the $(NH_4)_2S$ passivation treatment, as shown in Fig. 5-11. The dry-etched devices in general exhibit lower dark current floor than the wet-etched devices in the entire measurement range, regardless of the growth methods. Similar result is observed even in the smallest 25-μm-diameter devices, which sidewall surface leakage has more impact in comparison to the devices with larger size. In conclusion, the dry-etching method has more beneficial effect in creating a desired sidewall surface condition.

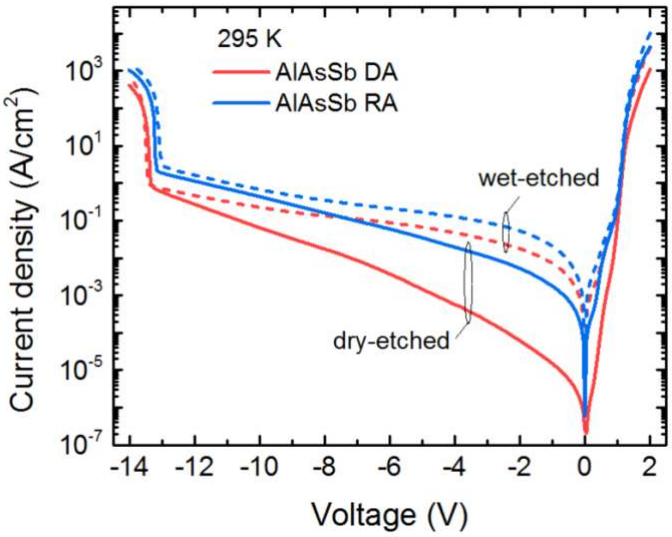

Figure 5-11 Dark current density curves of the AlAsSb DA and RA devices fabricated based on dry-etching and wet-etching methods.

5.3.2 Surface passivation

In addition to evaluating the etching chemistry, sidewall surface passivation is of high importance to devices based on antimonide materials, especially with high Al content. The optimization of surface condition is desired to minimize the leakage component and obtain the true device properties. Different passivation treatments that are commonly used for Sb-based compound or nanostructure devices, including (1) $(NH_4)_2S$ solution, (2) negative photoresist SU-

8, and (3) 200 nm SiO_2 deposited by PECVD, were investigated. The device sidewall surfaces were polished by HCl-based etchant prior to all passivation treatments. The dark current of the passivated DA devices was characterized at room-temperature and 77 K, as shown in Fig. 5-12. While the as-fabricated device shows a largely shunted current characteristic at room-temperature, all devices with passivation treatments have shown considerable improvement in dark current. Furthermore, the sulfurization treatment has resulted in the lowest dark current level, indicating that $(NH_4)_2S$ is the most effective method to eliminate the surface leakage paths created by oxides and metallic Sb on the sidewall surfaces. As a result, the $(NH_4)_2S$-passivated devices are used for the following device characterization.

It should be noted that the effect of $(NH_4)_2S$ passivation for the AlAsSb devices was also observed to degrade much rapidly over time in comparison to that of the GaSb devices. The room-temperature dark current level tended to increase by nearly two orders of magnitude and become stabilized after a few days, whereas the 77 K dark current is almost unaffected.

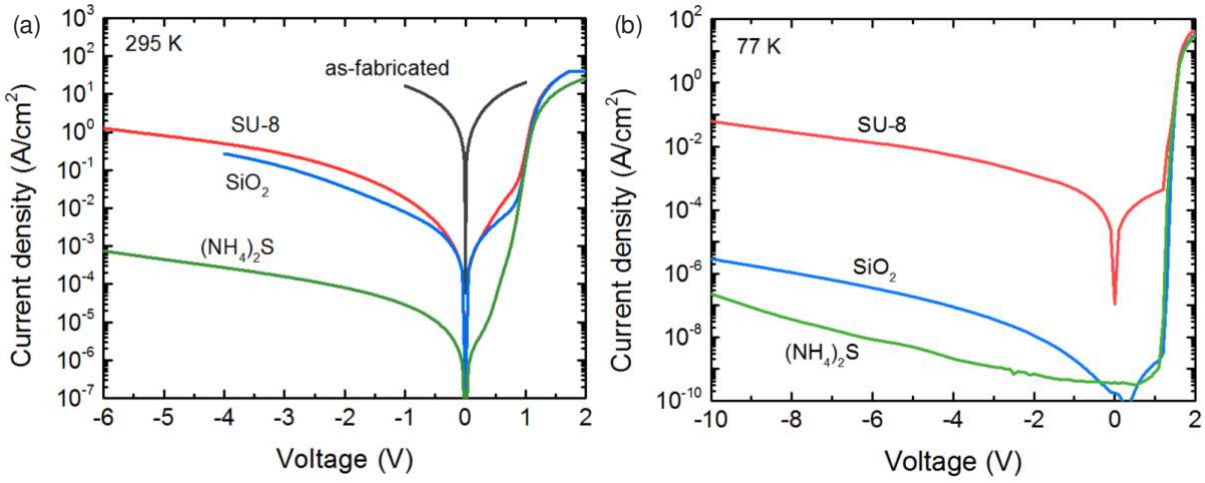

Figure 5-12 (a) Room-temperature and (b) 77K dark current density curves of the AlAsSb DA devices using passivation treatment of $(NH_4)_2S$ solution, SU-8 photoresist, and SiO_2 dielectric layer.

5.3.3 Device capacitance

The room-temperature C-V measurements are performed with both AlAsSb DA and RA device samples. The C-V curves show good agreement in the entire measurement range, as shown in Fig. 5-13. This confirms that both devices consist of nearly identical doping profile, offering a fair comparison of the device characteristics. The i-region has been fully depleted at zero bias, as indicated by the relatively unchanged device capacitance with increasing reverse bias. In addition, the doping concentration in the i-region can be extracted from the linear region of the $1/C^2$-V plot at forward bias regime, suggesting a charge density of 5.25×10^{15} cm^{-3} with a built-in voltage potential of 1 V (Table 5-3).

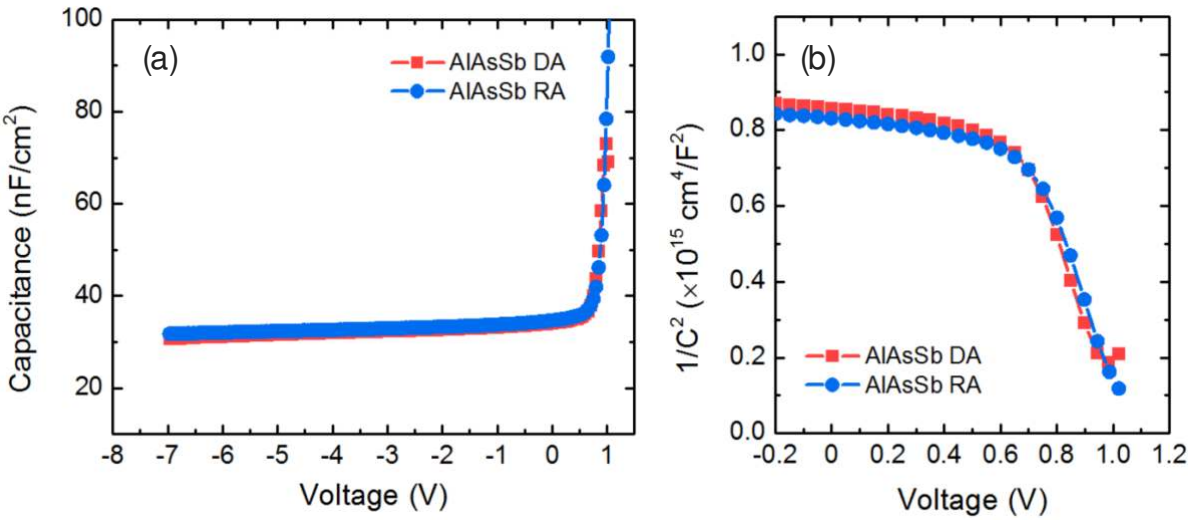

Figure 5-13 (a) C-V and (b) $1/C^2$-V plots of the AlAsSb DA and RA devices at room-temperature.

Parameter	AlAsSb DA	AlAsSb RA
i-region width (µm)	286	278
i-region doping (cm^{-3})	5.25×10^{15}	5.26×10^{15}
Built-in voltage (eV)	0.98	1.00

Table 5-3 The device parameters of the AlAsSb DA and RA device samples.

5.3.4 Dark current

The dark current measurements were performed at both room-temperature and low-temperature (Fig. 5-14). It is shown that the DA devices are limited by the sidewall surface current at room-temperature since the total current density increases with a decreasing device active area, and the devices exhibit a relatively minor effect of surface leakage at 77 K. Abrupt device breakdowns are observed for different size mesas at both high and low temperatures, and no BTBT current was observed in both AlAsSb device samples. The forward bias current is shown in Fig. 5-14(b), and some surface leakage current have presented below 0.8 V and 1.2 V at room-temperature and at 77 K, respectively. The ideality factors n of 2 is extracted at 77 K, suggesting

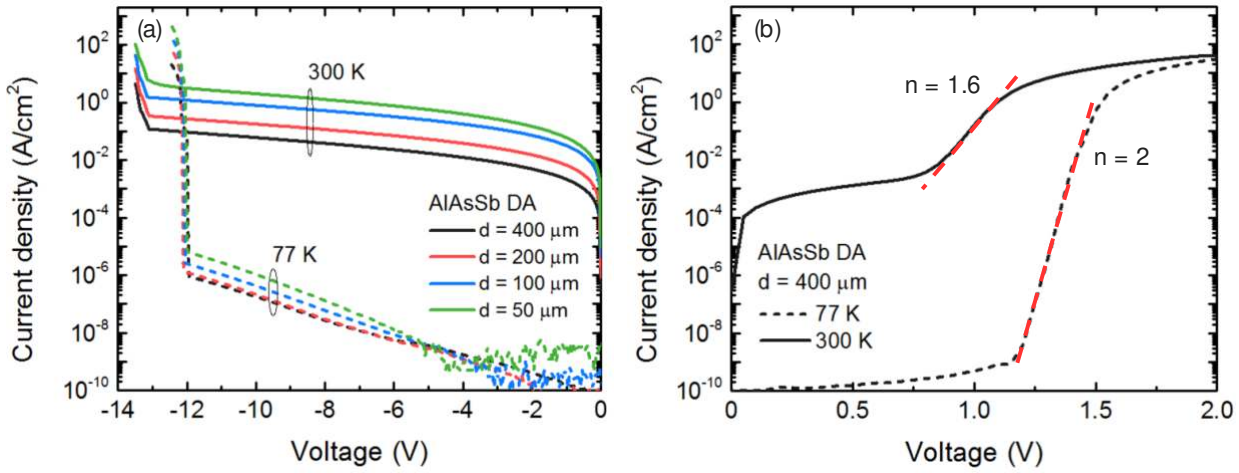

Figure 5-14 Room-temperature and 77 K (a) reverse bias and (b) forward bias dark current density curves of the AlAsSb DA devices. The red dashed lines indicate the fitting to the ideality factors.

a predominant generation-recombination current. This is understood by the significantly small intrinsic carrier concentration n_i in the large-bandgap AlAsSb at low temperature. The diffusion component is proportional to n_i^2, whereas the generation-recombination component is proportional to n_i, indicating that the diffusion current becomes essentially negligible in comparison to the generation-recombination current at 77 K.

5.3.5 Temperature-dependent measurement

The bulk and the surface components can be separated using the linear fitting with current densities and perimeter-to-area ratio at different temperatures, as suggested by Eq. 3-2. The dark currents at 50 mV are extracted for various size device mesas and the Arrhenius plots of the separated current components for the DA and the RA devices are created, as shown in Fig. 5-15. The surface components from both devices are found to exhibit similar activation energy in the range of 0.247-0.253 eV, suggesting the good accuracy of the measurement. On the other hand, it

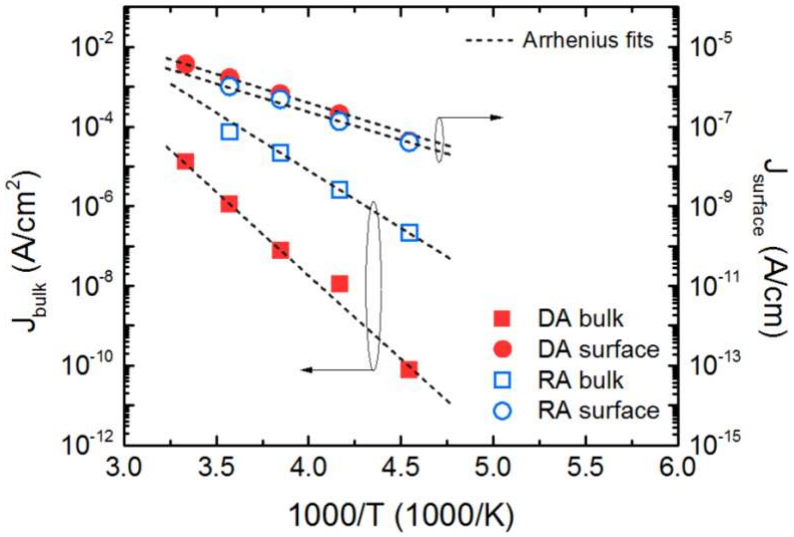

Figure 5-15 Dark current activation energies of the AlAsSb DA and RA devices. The bulk and the surface current components are extracted using P/A dependence of the total current densities at each temperature.

is shown that the extracted activation energies of the bulk components are very different. The activation energy of 0.800±0.026 eV is extracted for the DA devices, indicating that the generation-recombination centers located near mid-bandgap are likely responsible for the leakage mechanism. For the RA device, the extracted bulk activation energy is about 0.543±0.020 eV, smaller than the mid-bandgap energy. This indicates that additional defect states in the RA devices.

Fig. 5-16 shows the V_{BD} values of both DA and the RA devices as a function of temperature, which exhibits positive temperature coefficients confirming that the device breakdown is due to avalanche process instead of the field-assisted tunneling. Both devices have shown approximately the same temperature coefficient, 5.73±0.08 meV/K and 5.81±0.13 meV/K for the DA and the RA

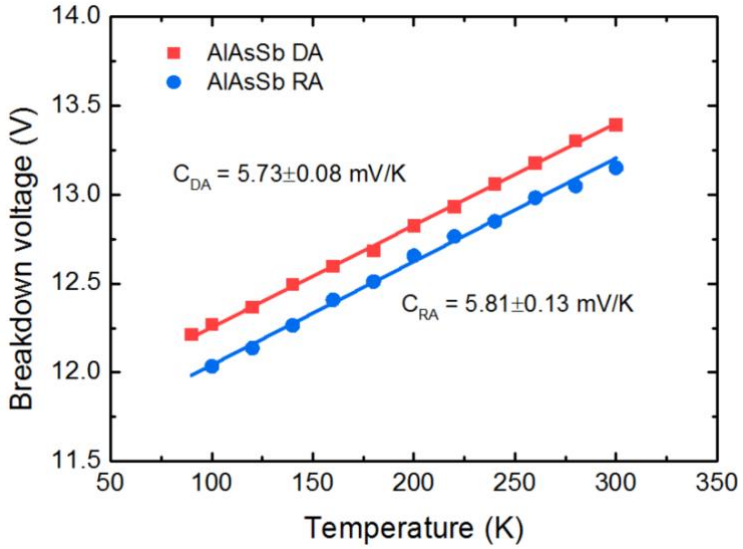

Figure 5-16 Temperature coefficient of V_{BD} for the AlAsSb DA and RA devices.

Material	Multiplication width (nm)	Temperature coefficient (mV/K)
$AlAs_{0.08}Sb_{0.92}$ (this work)	286	5.73
$AlAs_{0.56}Sb_{0.42}$[30]	230	1.47
GaAs (this work)	300	8.9
GaAs[31]	270	8.89
Si[32]	290	4.38
InP[33]	200	6.0

Table 5-4 The temperature coefficients of V_{BD} of the AlAsSb DA device and other common materials used for APDs.

devices, respectively. In addition, the temperature coefficient of AlAsSb also suggest a relatively small variation in avalanche gain statistics against temperature, likely due to the result of a larger phonon energy in comparison to that of other III-V materials. The temperature coefficient of V_{BD} and the associated multiplication width of commonly used materials are listed in Table 5-4.

5.3.6 Spectral response

The spectral response measurement allows an accurate estimation to the direct and the indirect bandgap energies of the AlAsSb devices, and the relative responsivity curves as a function of excitation photon energies obtained at zero bias are shown in Fig. 5-17(a). In the AlAsSb device structure, the 50-nm-thick GaSb capping layer absorbs a significant amount of light in the measured wavelength range, and thus, the obtained responsivity values are low and do not represent the actual responsivity values that can be obtained from the AlAsSb devices. The AlAsSb DA device exhibits an overall stronger photoresponse in comparison to the RA device, which shows good agreement to the material characterization results as discussed in the previous sections. The cut-off energy near the absorption edge is used to extract the AlAsSb bandgap energy, and the relationships between the absorption coefficient and the transition energies can be described as[34,35],

$$\alpha^{direct} \propto \left(E_{ph} - E_g^{direct}\right)^{1/2} \tag{4.4}$$

and

$$\alpha^{indirect} \propto \left(E_{ph} - E_g^{indirect} \pm \hbar\omega\right)^2 \tag{4.5}$$

where α is the absorption coefficient, E_{ph} is the incident photon energy, and $\hbar\omega$ is the phonon energy. The respective E_g can be extrapolated from the measured responsivity values since $R \propto \alpha$ when $\left(E_{ph} - E_g\right) \to 0$. As shown in Fig. 5-17(b-c), the direct bandgap E_g^{Γ} and the indirect

bandgap E_g^{X} can be obtained using the linear extrapolation of R^2 and $R^{1/2}$ near the absorption edge, respectively. The extracted bandgap energies are listed in Table 5-5. The DA device has exhibited a smaller bandgap energy than the RA device, which is also in a good agreement with the PL characterization as discussed in the previous section.

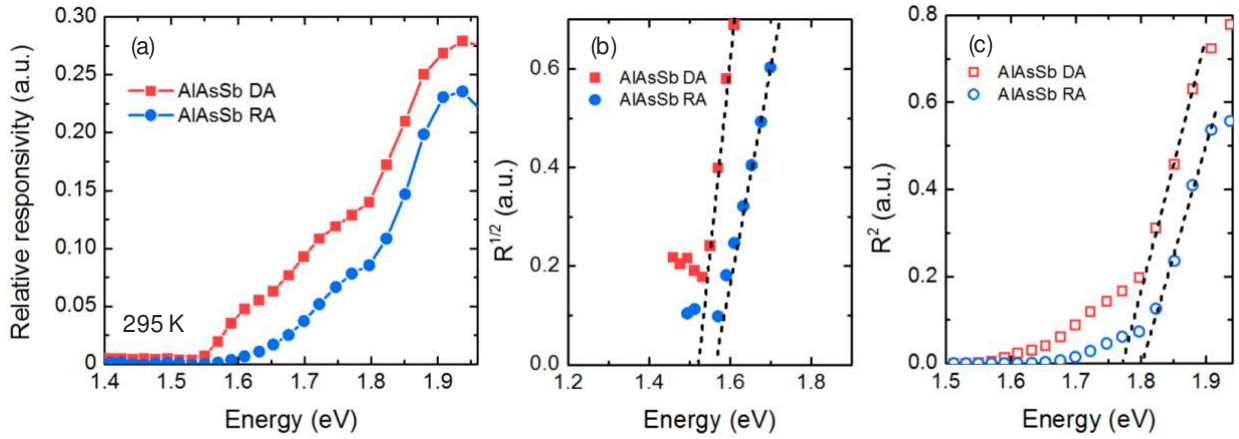

Figure 5-17 (a) Measured relative responsivity of the AlAsSb DA and RA devices; (b) root and (c) square of responsivity of the AlAsSb devices at zero bias used to estimate the indirect and direct bandgap, respectively.

Material	E_g^{Γ} (eV)	E_g^{X} (eV)
AlAsSb DA	1.770	1.522
AlAsSb RA	1.800	1.555
AlAsSb theoretical[36]	2.297	1.639

Table 5-5 The direct and indirect bandgap energies of the AlAsSb extrapolated from the spectral responsivity measurement and the theoretical values.

5.4 X-ray and gamma-ray response

5.4.1 Packaged device characteristics

Even though the AlAsSb alloy will not be used as the absorption region in the heterostructure device, it is still informative to study the radiation response of the material. The representative AlAsSb DA devices have been packaged for radiation measurement. Fig. 5-18 shows the electrical and the optical characteristics of the 400-µm-diameter device. Because of the finite surface leakage current, the packaged device was cooled down to 77 K to exhibit a sufficiently low dark current floor. In addition, a slight increase in dark current after the wire-bonding process was observed. The photocurrent plateau indicates the full carrier collection has occurred at zero bias. The extracted avalanche gain curve suggests a unity gain regime up to the

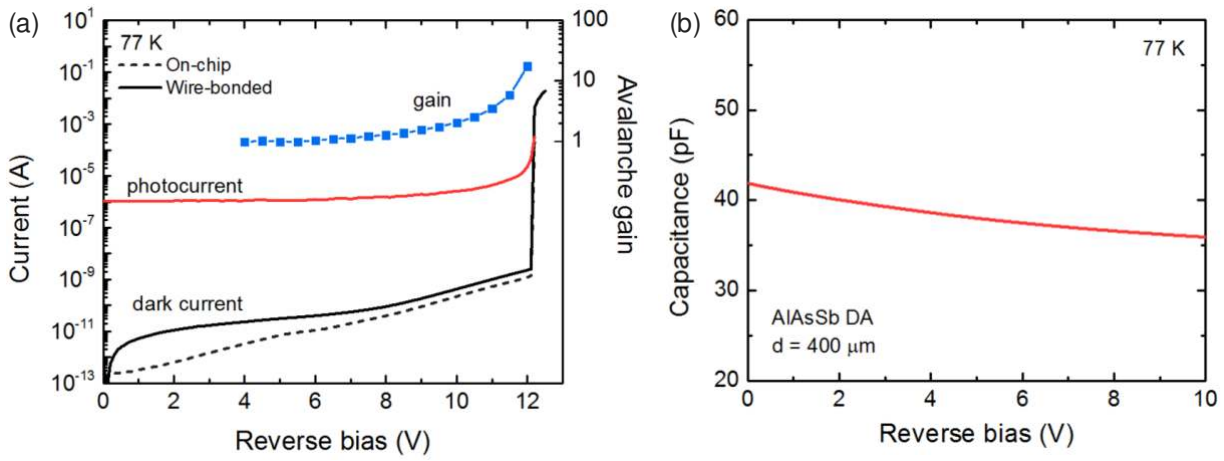

Figure 5-18 The representative electrical and optical characteristics including (a) dark current, photocurrent, avalanche gain curve, and (b) device capacitance as a function of reverse bias of a 400-µm-diameter AlAsSb DA device prepared for radiation measurement.

reverse bias of 6 V (an average electric field strength of 250 kV/cm) and a maximum gain of approximately 18 near V_{BD}. Since the i-region has already been fully depleted at zero bias, as

shown in Fig. 5-18(b), a further increase in reverse bias would extend the depletion region into heavily doped neutral regions, reducing only a limited amount of the device capacitance.

5.4.2 ^{241}Am spectrum

Prior to the measurement, the noise associated with the device and the readout electronics were calibrated and the optimum condition was determined. Fig. 5-19 shows the ^{241}Am spectrum obtained by the AlAsSb DA device at a reverse bias of 4 V with a shaping time of 3 μs. The 0.74 MBq ^{241}Am radioactive source was carefully placed about 2 mm away from the AlAsSb DA device to maximize the count rate of incident photons. The energy spectrum acquired shows clear features of the low-energy lines from the ^{241}Am source, including 13.9 keV and 17.8 keV, which can be resolved by fitting with the Gaussian distributions. By knowing the zero position of the noise peak,

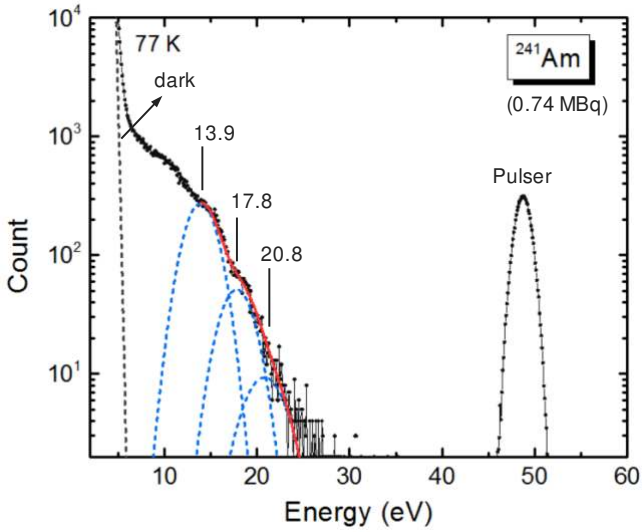

Figure 5-19 ^{241}Am energy spectrum generated by the AlAsSb device at 77 K. The pulser signal is also shown as a reference to the electronic noise, and the primary energy lines are fitted with the Gaussian distribution.

the energy scale can be calibrated. The spectrum measured without the source is also displayed in order to indicate the noise floor, and the electronic noise is measured as indicated by the pulser

FWHM of 2.04 keV. In addition to the photopeak broadening caused by the electronic noise and the Fano noise (200-230 eV), excess noise has been observed for the 13.9 keV and 17.8 keV photopeaks. The excess noise here is considered as a result of the incomplete carrier collection, primarily due to the ultra-thin absorption region and the low-Z absorbing material.

5.4.3 Pair creation energy

The pair creation energy (ε_{AlAsSb}) of AlAsSb can be estimated by using the known photopeak positions in the ^{241}Am spectra obtained by the AlAsSb DA device and the reference GaAs PIN device. The experiment details are the same as discussed in chapter 3. The ε_{AlAsSb} has been calculated as 4.309±0.072 eV using the similar formula described in Eq. 3-7. The extracted

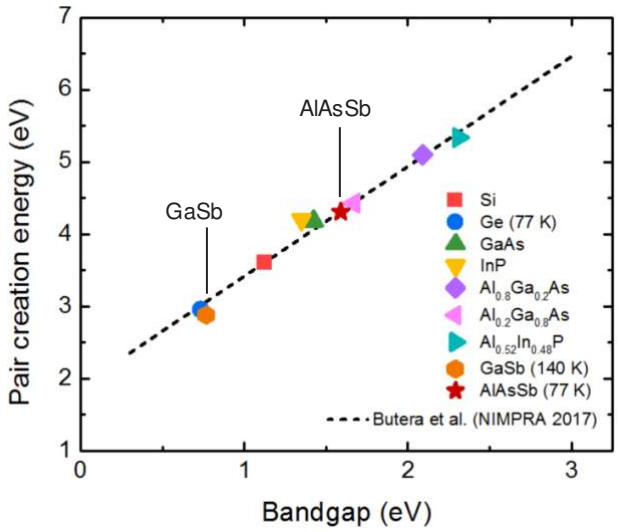

Figure 5-20 (a) The estimated PCE of AlAsSb along with that of other semiconductors reported from literature. (b) The predicted pulse height as a function of photon energy for AlAsSb and GaSb.

ε_{AlAsSb} has shown a good agreement with the empirical model[37], as depicted in Fig. 5-20. It is shown that AlAsSb has presented a much larger PCE in comparison to that of GaSb. For a given photon energy, the signal strength created by the GaSb region would be considerably greater than the AlAsSb region. As a result, the photopeaks in the energy spectra produced by the integrated

GaSb/AlAsSb device are expected to be well-separated and the probability of spurious photopeaks generated outside of the absorption region is reduced.

5.5 Discussion

In summary, this study investigated the electrical and optical characteristics of the AlAsSb alloy using DA and RA growth techniques by MBE. Two material samples lattice-matched to GaSb were developed as verified using HRXRD scans, and the microscopic characterization showed no sign of crystalline disorders such as phase separation that is commonly observed for the mixed-anion alloys. In addition, the DA sample exhibits consistently stronger PL intensities with smaller FWHM values than those of the RA sample at the elevated temperatures, suggesting the DA growth is relatively free from non-radiative recombination centers induced by crystalline defects. The electrical properties were characterized using the PIN device structure. The device fabrication including mesa etching methods and passivation treatments were investigated in order to minimize the effect of the surface leakage current. The AlAsSb DA device has exhibited a relatively low dark current level associated with an activation energy approximately at mid-bandgap, whereas the RA device shows a smaller activation energy suggesting a relatively high defect density. Radiation measurement using the ^{241}Am radioactive source was performed with the DA device. A PCE of 4.309±0.072 eV has been successfully extracted for AlAsSb at 77 K. The large difference in PCE values between GaSb and AlAsSb has effectively provided the GaSb/AlAsSb material system a great advantage as the energy-sensitive radiation detectors. The findings in this study provide direct evidence that, compared to the conventional RA growth, the DA growth could offer a more compositional uniform III-(As, Sb) alloy with enhanced material quality, better suited for device applications.

5.6 Reference

1. Xie, J., Ng, J. S. & Tan, C. H. An InGaAs/AlAsSb Avalanche Photodiode With a Small Temperature Coefficient of Breakdown. *IEEE Photonics J.* **5,** 6800706 (2013).

2. Tan, C. H., Xie, S. & Xie, J. Low Noise Avalanche Photodiodes Incorporating a 40 nm AlAsSb Avalanche Region. *IEEE J. Quantum Electron.* **48,** 36–41 (2012).

3. Xie, J., Xie, S., Tozer, R. C. & Tan, C. H. Excess Noise Characteristics of Thin AlAsSb APDs. *IEEE Trans. Electron Devices* **59,** 1475–1479 (2012).

4. Bitter, M. *et al.* InGaAs-on-Si photodetectors for high-sensitivity detection. in **5406,** 1–12 (2004).

5. Pessetto, J. R. & Stringfellow, G. B. $Al_xGa_{1-x}As_ySb_{1-y}$ phase diagram. *J. Cryst. Growth* **62,** 1–6 (1983).

6. Canedy, C. L. *et al.* Correlating growth conditions with photoluminescence and lasing properties of mid-IR antimonide type II 'W' structures. *J. Vac. Sci. Technol. B Microelectron. Nanom. Struct. Process. Meas. Phenom.* **22,** 1575–1579 (2004).

7. Zhang, Y.-H. Accurate control of As and Sb incorporation ratio during solid-source molecular-beam epitaxy. *J. Cryst. Growth* **150,** 838–843 (1995).

8. Maddox, S. J., March, S. D. & Bank, S. R. Broadly Tunable AlInAsSb Digital Alloys Grown on GaSb. *Cryst. Growth Des.* **16,** 3582–3586 (2016).

9. Kaspi, R. & Donati, G. P. Digital alloy growth in mixed As/Sb heterostructures. *J. Cryst. Growth* **251,** 515–520 (2003).

10. Woodson, M. E. *et al.* Low-noise AlInAsSb avalanche photodiode. *Appl. Phys. Lett.* **108,**

81102 (2016).

11. Kaspi, R. *et al.* High power and high brightness from an optically pumped InAs/InGaSb type-II midinfrared laser with low confinement. *Appl. Phys. Lett.* **81,** 406–408 (2002).

12. Mourad, C., Gianardi, D., Malloy, K. J. & Kaspi, R. 2 μm GaInAsSb/AlGaAsSb midinfrared laser grown digitally on GaSb by modulated-molecular beam epitaxy. *J. Appl. Phys.* **88,** 5543–5546 (2000).

13. Bennett, B. R., Ancona, M. G., Boos, J. B., Canedy, C. B. & Khan, S. A. Strained GaSb/AlAsSb quantum wells for p-channel field-effect transistors. *J. Cryst. Growth* **311,** 47–53 (2008).

14. Juang, B.-C. *et al.* GaSb thermophotovoltaic cells grown on GaAs by molecular beam epitaxy using interfacial misfit arrays. *Appl. Phys. Lett.* **106,** 111101 (2015).

15. Nosho, B. Z., Bennett, B. R., Aifer, E. H. & Goldenberg, M. Surface morphology of homoepitaxial GaSb films grown on flat and vicinal substrates. *J. Cryst. Growth* **236,** 155–164 (2002).

16. Murray, L. M. *et al.* Causes and elimination of pyramidal defects in GaSb-based epitaxial layers. *J. Vac. Sci. Technol. B* **31,** 03C108 (2013).

17. Koerperick, E. J., Murray, L. M., Norton, D. T., Boggess, T. F. & Prineas, J. P. Optimization of MBE-grown GaSb buffer layers and surface effects of antimony stabilization flux. *J. Cryst. Growth* **312,** 185–191 (2010).

18. Lorenz, M. R., Chicotka, R., Pettit, G. D. & Dean, P. J. The fundamental absorption edge of AlAs and AlP. *Solid State Commun.* **8,** 693–697 (1970).

19. Zollner, S., Lin, C., Schönherr, E., Böhringer, A. & Cardona, M. The dielectric function of

AlSb from 1.4 to 5.8 eV determined by spectroscopic ellipsometry. *J. Appl. Phys.* **66,** 383–387 (1989).

20. O'Donnell, K. P. & Chen, X. Temperature dependence of semiconductor band gaps. *Appl. Phys. Lett.* **58,** 2924–2926 (1991).

21. Sela, I., Bolognesi, C. R. & Kroemer, H. Single-mode behavior of $AlSb_{(1-x)}As_x$ alloys. *Phys. Rev. B* **46,** 16142–16143 (1992).

22. Kawamura, Y., Gomyo, A., Suzuki, T., Higashino, T. & Inoue, N. Band-Gap Change in Ordered/Disordered $GaAs_{1-y}Sb_y$ Layers Grown on (001) and (111)B InP Substrates. *Jpn. J. Appl. Phys.* **41,** L447 (2002).

23. Kwon, O., Lin, Y., Boeckl, J. & Ringel, S. A. Growth and properties of digitally-alloyed AlGaInP by solid source molecular beam epitaxy. *J. Electron. Mater.* **34,** 1301–1306 (2005).

24. As, D. J. *et al.* The near band edge photoluminescence of cubic GaN epilayers. *Appl. Phys. Lett.* **70,** 1311–1313 (1997).

25. Schmidt, T., Lischka, K. & Zulehner, W. Excitation-power dependence of the near-band-edge photoluminescence of semiconductors. *Phys. Rev. B* **45,** 8989–8994 (1992).

26. Lieten, R. R. *et al.* Photoluminescence of bulk germanium. *Phys. Rev. B* **86,** 35204 (2012).

27. Wang, G. *et al.* Comparative study of photoluminescence from $In_{0.3}Ga_{0.7}As$/GaAs surface and buried quantum dots. *Nanotechnology* **27,** 465701 (2016).

28. Ma, Y. J. *et al.* Behaviors of beryllium compensation doping in InGaAsP grown by gas source molecular beam epitaxy. *AIP Adv.* **7,** (2017).

29. Baranowski, M. *et al.* Time-resolved photoluminescence studies of annealed 1.3-μm GaInNAsSb quantum wells. *Nanoscale Res. Lett.* **9,** 81 (2014).

30. Shiyu Xie & Chee Hing Tan. AlAsSb Avalanche Photodiodes With a Sub-mV/K Temperature Coefficient of Breakdown Voltage. *IEEE J. Quantum Electron.* **47,** 1391–1395 (2011).

31. Groves, C., Ghin, R., David, J. P. R. & Rees, G. J. Temperature dependence of impact ionization in GaAs. *IEEE Trans. Electron Devices* **50,** 2027–2031 (2003).

32. Massey, D. J., David, J. P. R. & Rees, G. J. Temperature dependence of impact ionization in submicrometer silicon devices. *IEEE Trans. Electron Devices* **53,** 2328–2334 (2006).

33. Tan, L. J. J. *et al.* Temperature dependence of avalanche breakdown in InP and InAlAs. *IEEE J. Quantum Electron.* **46,** 1153–1157 (2010).

34. Sze, S. M. & Ng, K. K. *Physics of semiconductor devices*. (John Wiley & Sons, 2006).

35. Xie, S. *et al.* InGaAs/AlGaAsSb avalanche photodiode with high gain-bandwidth product. *Opt. Express* **24,** 24242–24247 (2016).

36. Vurgaftman, I., Meyer, J. R. & Ram-Mohan, L. R. Band parameters for III–V compound semiconductors and their alloys. *J. Appl. Phys.* **89,** 5815–5875 (2001).

37. Butera, S., Lioliou, G., Krysa, A. B. & Barnett, A. M. Measurement of the electron–hole pair creation energy in $Al_{0.52}In_{0.48}P$ using X-ray radiation. *Nucl. Instruments Methods Phys. Res. Sect. A Accel. Spectrometers, Detect. Assoc. Equip.* (2017).

6. GaSb/AlAsSb heterostructure devices

6.1 Background

The objective of using the integrated high-Z, small-bandgap absorber with the low-Z, large-bandgap junction region is to create a compact, low-power, energy-sensitive radiation detector that offers high energy resolution for gamma-ray detection. Previously, similar device structure using the GaAs material family has been studied as the separate absorption and multiplication regions avalanche photodiodes (SAM-APD) to provide energy-sensitive detection for X-ray photons. Lauter et al. have reported X-ray detector using GaAs/AlGaAs-based devices with a 4.5 μm absorption region with a staircase-like multiplication region[1]. The detector has established a FWHM of 2.0 keV at 13.96 keV with unity gain and an improved resolution of 0.9 keV with a gain of 4.1. In addition to X-ray detection, the detector has also shown the gamma-ray photopeak at 26.4 keV from the ^{241}Am source (Fig. 6-1(a)); however, the peak shows a much weaker relative intensity because of the low absorption efficiency of the low-Z GaAs. Gomes et al. have demonstrated the use of GaAs/$Al_{0.8}Ga_{0.2}As$ device structure for detecting the soft X-rays at 5.9 keV with a FWHM of 1.08 keV[2]. An undesired secondary peak located at an energy lower than the 5.9 keV peak is found, as shown in Fig. 6-1(b), due to the different degree of impact ionization for the electrons and holes in addition to the insufficient layer thickness ratio and PCE difference between GaAs and AlGaAs regions. Although the absorption efficiency can be generally improved by increasing the layer thickness, the intrinsic limitation of low-Z and large-PCE have prevented the use of SAM structure based on GaAs material family for gamma-ray detection.

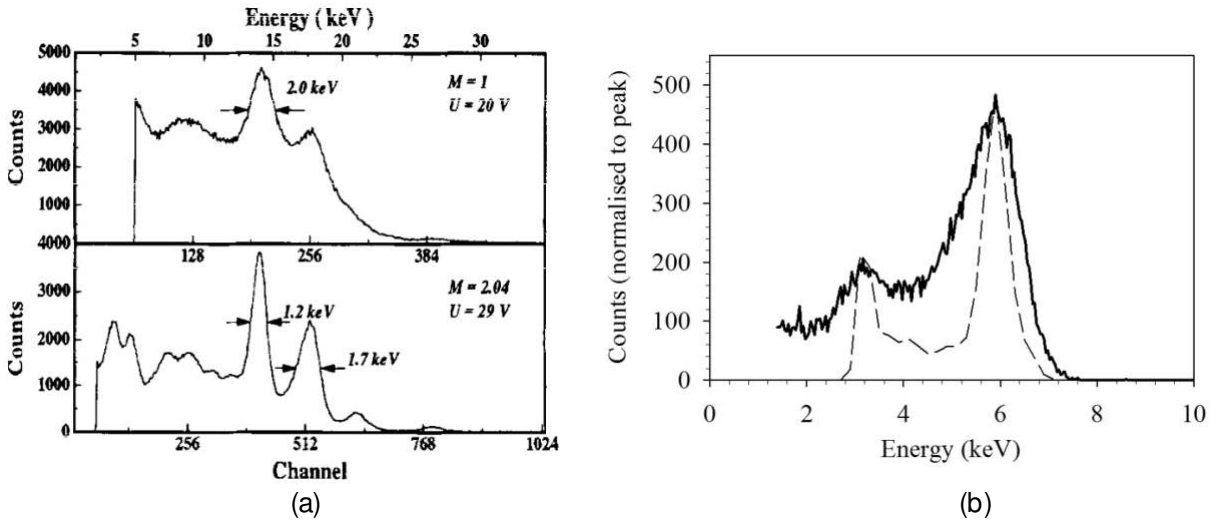

Figure 6-1 (a) ^{241}Am energy spectra obtained by the staircase-like GaAs/AlGaAs SAMAPD with a 4.5 µm GaAs absorption region[1], and (b) ^{55}Fe energy spectrum obtained by the GaAs/AlGaAs SAMAPD with a 430 nm GaAs absorption region[2]. The photopeak located around 3 keV results from the AlGaAs layer. Both figures are the reprints from the literature.

On the other hand, GaSb provides a much higher probability in stopping X-ray and gamma-ray photons at a given energy than GaAs because of its relatively high Z. The GaSb/AlAsSb material system also promises a larger difference in their PCE and absorption efficiency that can effectively suppress spurious photopeaks generated outside of the intended absorption region. This suggests that Sb-based material family could be a better candidate for detecting gamma-rays with high spectroscopic performance. In comparison to the GaSb/GaAs system as discussed in chapter 4, using a lattice-matched AlAsSb as the large-bandgap device component is expected to effectively improve the interface condition and facilitate carrier transport. The AlAsSb material optimization and characterization has been discussed in the previous chapter, which digital-alloy (DA) technique is determined as the optimum growth method for the junction region together with the GaSb absorption region in the integrated device architecture.

6.2 Device design

The device structure is illustrated in Fig. 6-2. The p-n junction is comprised of AlAsSb DA, followed by a 2 µm GaSb absorption layer. A 50 nm $Al_{0.4}Ga_{0.6}Sb$ (hereafter AlGaSb) window layer was added after the GaSb absorption layer in order to eliminate the carrier loss due to front surface recombination. The absorption layer thickness is chosen to match the previous GaSb PIN devices for a fair comparison of their performance metrics. In the designed structure, the vast majority of the electric field would be confined within the AlAsSb region, whereas the electric field strength is maintained in a sufficiently low magnitude in the GaSb region to minimize the effect of field-assisted current components, such as field-enhanced SRH process and band- to-band tunneling (BTBT) process. A field-control (FC) layer is inserted between the AlAsSb junction region and the GaSb absorption region to provide an extra control in the electric field. Different

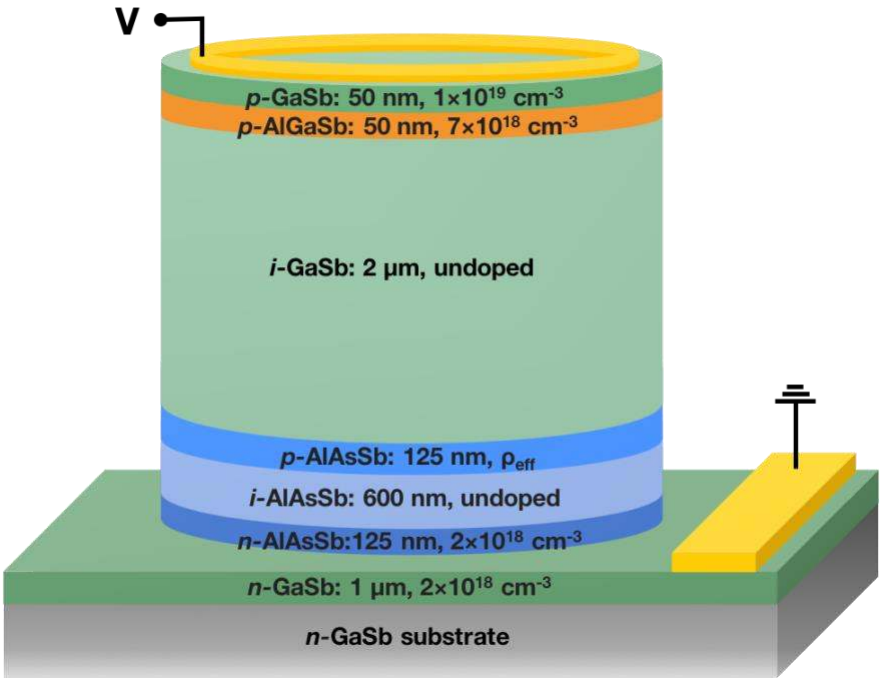

Figure 6-2 The GaSb/AlAsSb detector structure with a 2 µm GaSb absorption region.

charge densities of the FC layer are used in order to optimize the electric field distribution. The nominal charge density ρ_{eff} used in this study includes 6.25×10^{11} cm^{-2}, 1.25×10^{12} cm^{-2}, and 3.75×10^{12} cm^{-2} that are achieved by varying the Be doping concentrations in the AlAsSb FC layers while keeping a constant layer thickness.

6.3 Electrical characterization

6.3.1 Device capacitance

The C-V measurement can provide useful information about the electric field distribution and the depletion region of the device as a function of reverse bias. The devices were cooled to 77 K to maintain low dark current. In Fig. 6-3(a), the relatively flat C-V curves at low bias range indicate that the *i*-AlAsSb layer has been fully depleted for all devices at zero bias. In addition, the $1/C^2$-V analysis at forward bias (not shown) suggests a background doping of approximately 6×10^{14} cm^{-3} in the *i*-AlAsSb layer. With increasing reverse bias, the C-V curves begin to show different features, reflecting the effect of FC layer on the device electric field profile, i.e., depletion region. The change from flat to steep slopes in the C-V curves are identified as the edge of the depletion region has reached the GaSb region, which transition point is labeled as V_{reach}, namely the minimum bias voltage required to initiate the depletion within the GaSb absorption region (Fig. 6-3(b)). It is shown that V_{reach} tends to increase with the FC charge density, which takes place at 5 V and 7.5 V for the 6.25×10^{11} cm^{-2} and the 1.25×10^{12} cm^{-2} devices, respectively. On the other hand, there is no sign of such transition for the 3.75×10^{12} cm^{-2} device, which capacitance is relatively unchanged with increasing reverse bias. This suggests that the edge of the depletion region is located within the FC layer, and the electric field is fully confined to the AlAsSb region.

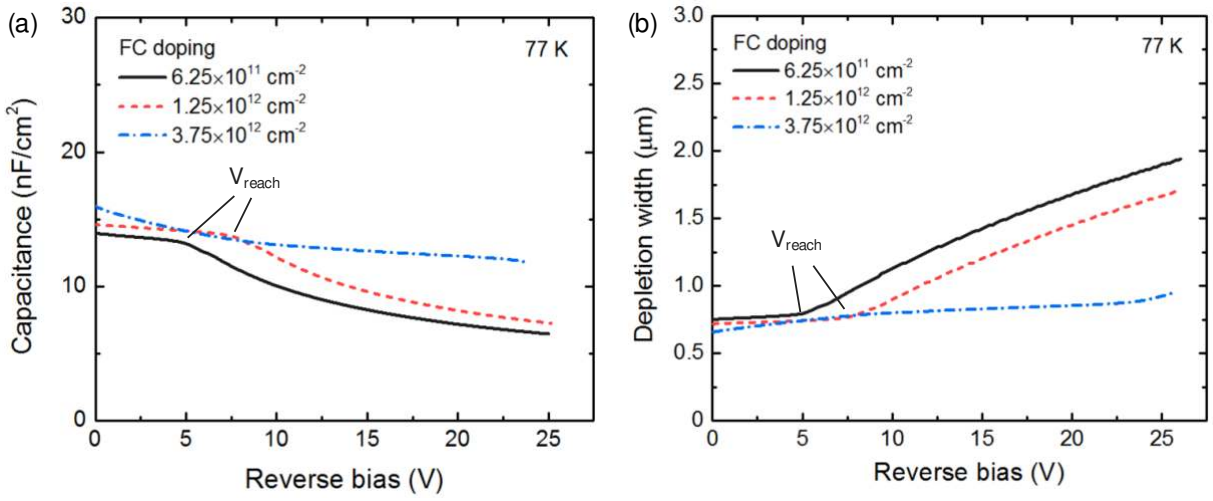

Figure 6-3 (a) C-V curves and (b) depletion region widths of the GaSb/AlAsSb devices with different FC charge densities.

6.3.2 Dark current

At room-temperature, it is found that the dark current floor of the GaSb/AlAsSb devices has been limited by the surface leakage current as suggested by the large current density (~100 mA/cm^2) and the trend of increasing current density with decreasing mesa size. This is similar to the case of the AlAsSb PIN devices as discussed in chapter 5. Similarly, the dark current of the GaSb/AlAsSb devices is observed to decrease significantly with decreasing temperature. Fig. 6-4 shows the dark current measurements of the devices with different size mesas at 77 K. It is shown that, regardless of the FC charge density, the dark current increases monotonically with reverse bias and exhibits an abrupt breakdown. Interestingly, the I-V characteristics are held in common even for the 6.25×10^{11} cm^{-2} and the 1.25×10^{12} cm^{-2} devices, whose GaSb region becomes active after V_{reach}. There is no sign of additional dark current resulted from the GaSb region after V_{reach} for both devices, suggesting that the dark current components, especially the BTBT process, form the GaSb region are not the dominant mechanism. Furthermore, the minor surface current

component is present in the entire measurement range followed by a well-defined breakdown, indicating the BTBT current is not present in the AlAsSb region either. The attainable dark current floor can be further improved if the surface leakage current is removed.

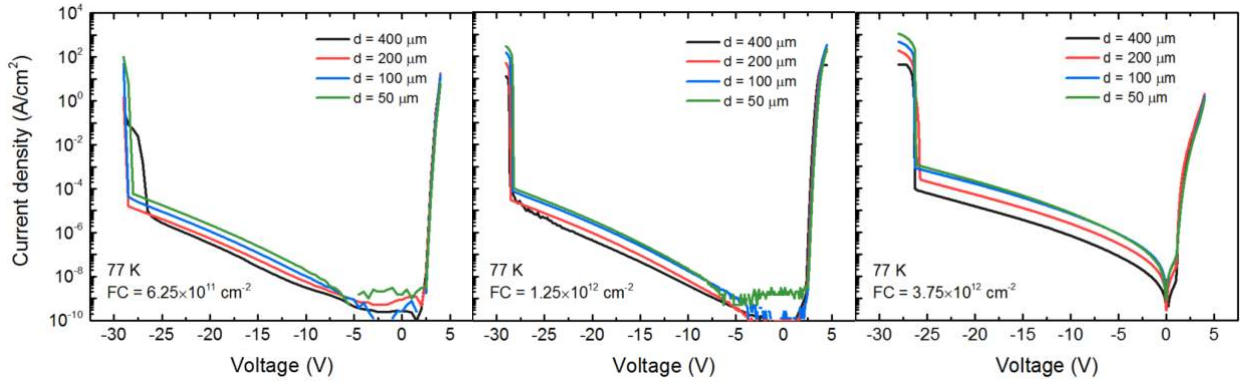

Figure 6-4 Dark I-V measurements of the GaSb/AlAsSb devices with different size mesas and different FC charge densities at 77 K.

6.3.3 Temperature-dependent dark current

The temperature-dependent measurements were performed to investigate the dark current characteristics of the GaSb/AlAsSb devices. It is shown in Fig. 6-5 that the GaSb/AlAsSb devices in general exhibit a strong temperature-dependent dark current in the entire reverse bias range before V_{BD}, supporting that the BTBT process is negligible in both the AlAsSb and the GaSb regions and are independent of the FC charge density used here. In addition, all devices exhibit an increased V_{BD} value with increasing temperature, indicating the breakdown mechanism is dominated by the avalanche process. As discussed in chapter 3, a considerable BTBT current component is expected to become dominant prior to the avalanche breakdown in GaSb; however, this is not the case here. As a result, we can conclude that the avalanche breakdown is originated from the AlAsSb region for all devices, and a reduced V_{BD} value is observed with increasing FC charge density. The activation energies extracted from all devices at the reverse bias of 5 V and 20

V all show a coherent value of 260-270 meV, supporting the observation that the dark current has primarily been dominated by the sidewall surface leakage component.

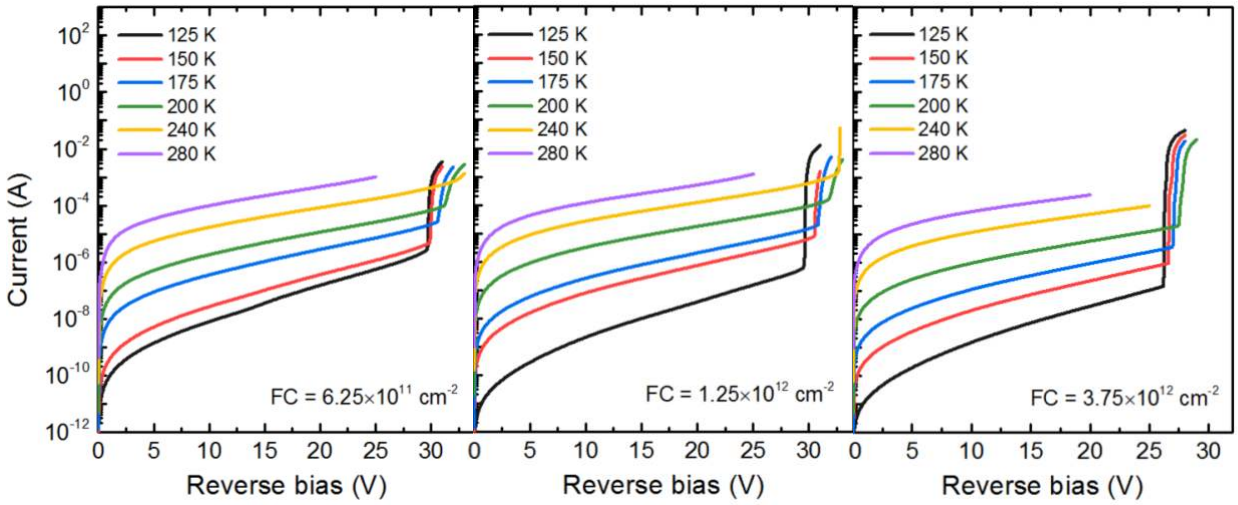

Figure 6-5 Temperature-dependent I-V measurement of the 200-µm-diameter GaSb/AlAsSb devices with different FC charge densities.

6.4 Optical characterization

6.4.1 Photocurrent

A continuous-wave (CW) laser emitted at 1310 nm is used for optical excitation in order to investigate the carrier transport properties by only allowing electron-hole pairs generation in the GaSb region. The photocurrent measurements of the GaSb/AlAsSb devices are shown in Fig. 6-6. At the low bias regime, there is little photoresponse for all devices since the GaSb region is not active. The photocurrent rises abruptly at reverse bias of 5 V and 7.5 V for the 6.25×10^{11} cm^{-2} and the 1.25×10^{12} cm^{-2} devices, respectively, corresponding to their V_{reach} as extracted from the C-V measurements. At reverse bias beyond V_{reach}, the depletion region has extended into the GaSb region, and the electric field begins to build up in favor of collecting carriers across the GaSb-

AlAsSb interface. The initial rise of photocurrent at V_{reach} can be considered as the onset of collection for carriers generated in the GaSb region. A significant increase in photocurrent takes place shortly after V_{reach} with increasing reverse bias, followed by an apparent plateau indicating the regime of full carrier collection at unity gain. The bias voltage V_{col} is assigned as the transitions where the full collection of the carriers has occurred. Furthermore, the comparable magnitude of primary photocurrent of the 6.25×10^{11} cm^{-2} and the 1.25×10^{12} cm^{-2} devices suggests an identical absorption profile, namely the GaSb absorber thicknesses are approximately the same. On the other hand, the device with highest FC charge density maintains a limited photocurrent in the entire reverse bias range, indicating an ineffective carrier collection. This can be explained by the excess

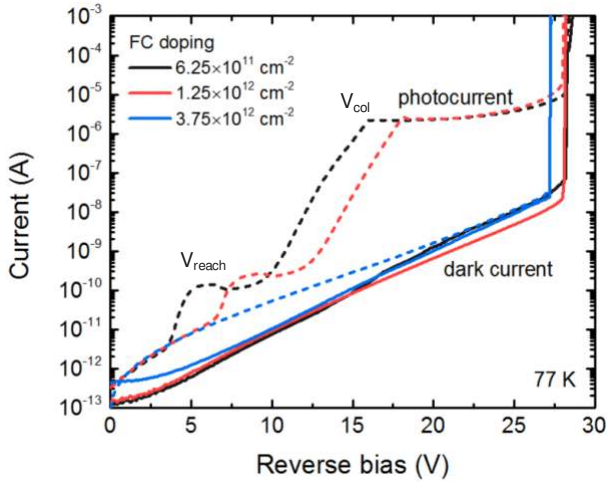

Figure 6-6 Dark current and photocurrent of the GaSb/AlAsSb devices with different FC charge densities at 77 K.

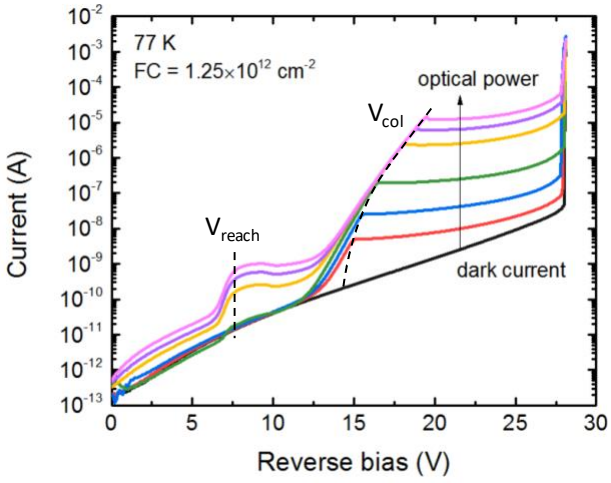

Figure 6-7 Photocurrent measurements of the 1.25×10^{12} cm^{-2} GaSb/AlAsSb device using different optical powers.

amount of charges in the FC layer that has effectively stopped the depletion and, thus, prevented the collection of carriers generated in the GaSb absorption region. For the 3.75×10^{12} cm^{-2} device, the GaSb region is not working as an active region in the device for the entire reverse bias range.

The rise of photocurrent between V_{reach} and V_{col} has been observed for the devices with light and medium FC charge densities. However, the feature cannot be correlated to the characteristic observed in C-V or I-V measurements of the devices. Fig. 6-7 shows the total current densities with different optical power. The value of V_{reach} does not show dependence with the optical power, indicating the electric field profile has been maintained the same regardless of the optical power. On the other hand, the value of V_{col} increases with the increasing optical power. The trend of V_{col} values can be well-described by an empirical model (Fig. 6-8),

$$V_{col} = V_{col}^{0} + aN_{ph}^{b} \ , \tag{6.1}$$

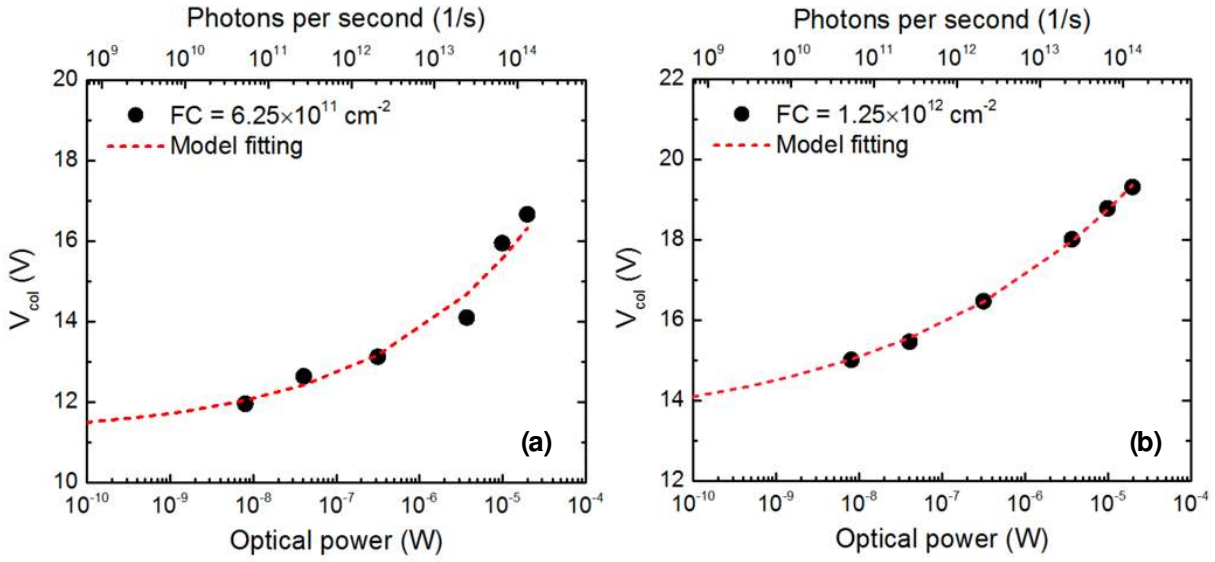

Figure 6-8 Extracted V_{col} values of (a) the 6.25×10^{11} cm^{-2} and (b) the 1.25×10^{12} cm^{-2} devices plotted as a function of optical power and number of incident photons per second.

where N_{ph} is the number of photons available to create electron-hole pairs, and a and b are fitting parameters. V_{col}^{0} represents the voltage of full collection when the number of carriers generated in the GaSb region is approaching a very small value, which are extracted to be 11.13 V and 13.16 V for the 6.25×10^{11} cm^{-2} and the 1.25×10^{12} cm^{-2} devices, respectively. In X-ray or gamma-ray

detection, each photon in the energy range of interest will create a relatively small average number of electron-hole pairs, on the order of 10^3-10^5, in comparison to that generated by the optical wavelength. As a result, a reverse bias near V_{col}^0 is expected for the GaSb/AlAsSb devices to obtain the condition of full carrier collection under exposure to X-ray and gamma-ray radiations. For example, a 59.5 keV photon creates approximately 2×10^4 electron-hole pairs in GaSb, resulting in a V_{col} value of approximately 13.3 V.

The origin of the rise of photocurrent is likely relevant to the GaSb-AlAsSb heterointerface property. It is shown as a common feature for both heterostructure devices, but it cannot be correlated to the PIN devices based on either GaSb or AlAsSb as discussed in the previous chapters. The effect of hole trapping is well known for the InGaAs/InP SAM structure at the heterointerface, due to the valence band discontinuities[3–6], which requires additional applied voltage to achieve an improved collection and speed of response. In our case, it is possible that majority of the electrons created in the GaSb region are "stored" at the GaSb-AlAsSb interface due to the conduction band discontinuities. Indeed, with increasing reverse bias, the strength of electric field in the vicinity of the interface begins to increase and the probability of trapping decreases as suggested by the significantly increased photocurrent. Once the certain electric field strength is established, the likelihood of electrons stored at the GaSb-AlAsSb interface is minimized since the carriers can now obtain a sufficient kinetic energy to travel through the interface. The temperature-dependent photocurrent measurement of the device illuminated by a constant optical power has been used to extract the equivalent barrier height. The emission current of trapped electrons can be related to thermionic behavior at a heterojunction barrier due to the band discontinuity, and the relationship is given by[3,5,6]

$$I_e \propto 1/\tau_e = B \cdot \exp\left(-\frac{q\phi_B}{k_B T}\right), \tag{6.2}$$

where $1/\tau_e$ is the rate of carrier emission, B is a constant, and ϕ_B is the equivalent barrier height at the heterointerface. The fitted barrier height as a function of reverse bias is shown in Fig. 6-9. It is shown that the equivalent barrier blocking the electrons is lowered with increasing reverse bias. The relationship can be approximated using a linear model, and the calculated effective barrier height is 242 meV at V_{reach}. It is expected that the effect of band discontinuity on carrier transport could be mitigated by adding the compositional graded layer between the absorption region and the junction region, as demonstrated in the InGaAs/InP material system[4,7–9].

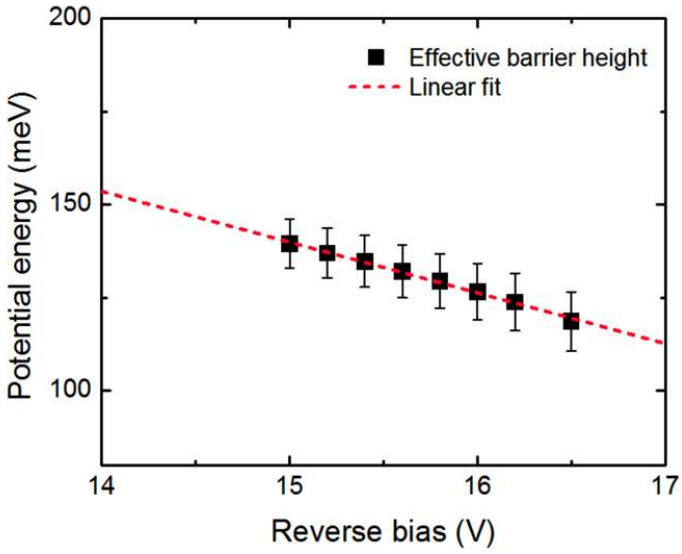

Figure 6-9 Calculated equivalent barrier height at the GaSb-AlAsSb interface due to the conduction band discontinuities.

6.4.2 Quantum efficiency and avalanche gain

The device responsivity has been characterized using the 1310 nm laser, as shown in Fig. 6-7. The active area of the devices has been carefully aligned to underfill with the coupled light spot from the fiber. The GaSb/AlAsSb devices exhibit a responsivity of 0.625 A/W as calibrated

using the primary photocurrent at V_{col}, which is higher than 0.578 A/W of the GaSb PIN devices measured at 77 K. The enhanced responsivity can be attributed to the help of top AlGaSb window layer, which has effectively eliminated the carrier loss via surface recombination. A reflectance of 37.8% is measured using FTIR and Continuum FTIR microscope and a transmittance T of 3% is calculated. As a result, an IQE value >99% has been estimated for the devices based on Eq. 3.6. It is worth to mention that despite the C-V measurement shows that the GaSb absorption region is not fully depleted in the devices (due to the unintentional background doping of GaSb), the long carrier lifetime and high carrier mobilities of GaSb have effectively facilitated the carrier transports.

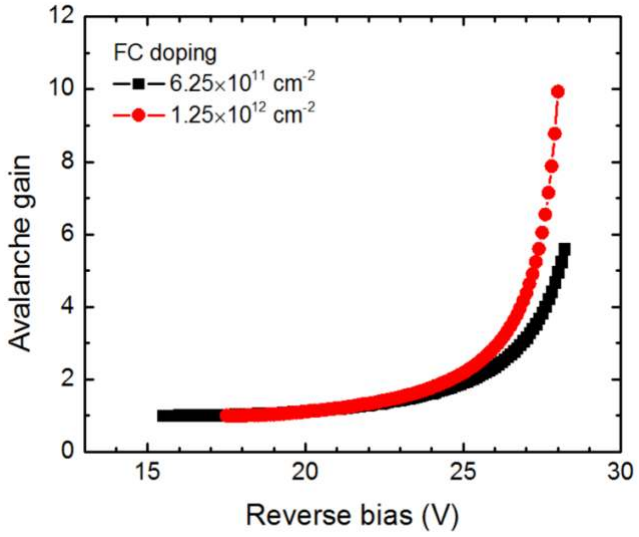

Figure 6-10 Avalanche gain curves of the 6.25×10^{11} cm^{-2} and the 1.25×10^{12} cm^{-2} GaSb/AlAsSb devices extracted using an optical power of 300 nW.

The representative avalanche gain curves of the devices are shown in Fig. 6-10, extracted from the photocurrent measurement using an optical power of 0.23 μW. In order to extract the multiplication factor from the low photocurrent level, the phase-sensitive gain measurement using lock-in amplifier were used and showed good agreement with the values calculated based on direct conversion method. It is shown that the avalanche gain in the 1.25×10^{12} cm^{-2} device is larger than

the 6.25×10^{11} cm^{-2} device at a given reverse bias, suggesting a higher electric field in the AlAsSb region. The dark current performance of the GaSb/AlAsSb devices can also be evaluated by comparing the current level at a given gain and the required reverse bias. For instance, at an avalanche gain of 5 under the same optical power, the 6.25×10^{11} cm^{-2} device exhibits a dark current density of 59.3 nA at 28 V. On the other hand, the 1.25×10^{12} cm^{-2} device shows a nearly five-fold lower dark current density of 12.5 nA at 27.2 V, suggesting an improved electric field management and a reduced noise level for the radiation measurement.

6.4.3 Temporal response

The GaSb/AlAsSb devices have exhibited a nearly ideal IQE, suggesting a minimal level of carrier loss during the collection process. However, it is also shown in the C-V measurement that the GaSb absorption region is partially depleted before V_{BD}. This suggests the carrier transport will likely rely on a combination of drift and diffusion components depending on the location where those carriers are created in the GaSb region. The diffusion component is normally a much slower process than the drift component. The signals composed of both slow and fast components could potentially lead to distortions in the time domain. As a result, the temporal response of the GaSb/AlAsSb devices is studied to further investigate the impact of the carrier transport on the generated signal shapes.

The temporal response measurement was conducted by illuminating the 200-μm-diameter GaSb/AlAsSb device with a 1310 nm laser pulse using supercontinuum white light source coupled to an acousto-optic tunable filter. The pulse width is estimated to be approximately 20 ps with a 13 MHz repetition rate. Transient pulse characteristics were measured with a microwave probe and a 20 GHz oscilloscope (50 GS/s). A microwave bias-T was used to apply bias to the device while transmitting the AC signal to the oscilloscope. Fig 6-11 shows the temporal response of the

devices using an optical pulse with an average power of 4.3 μW. For both devices, the pulse signals were observed when the respective V_{col} were applied, and the changes of pulse amplitude showed good agreement with avalanche gain curves with increasing reverse bias.

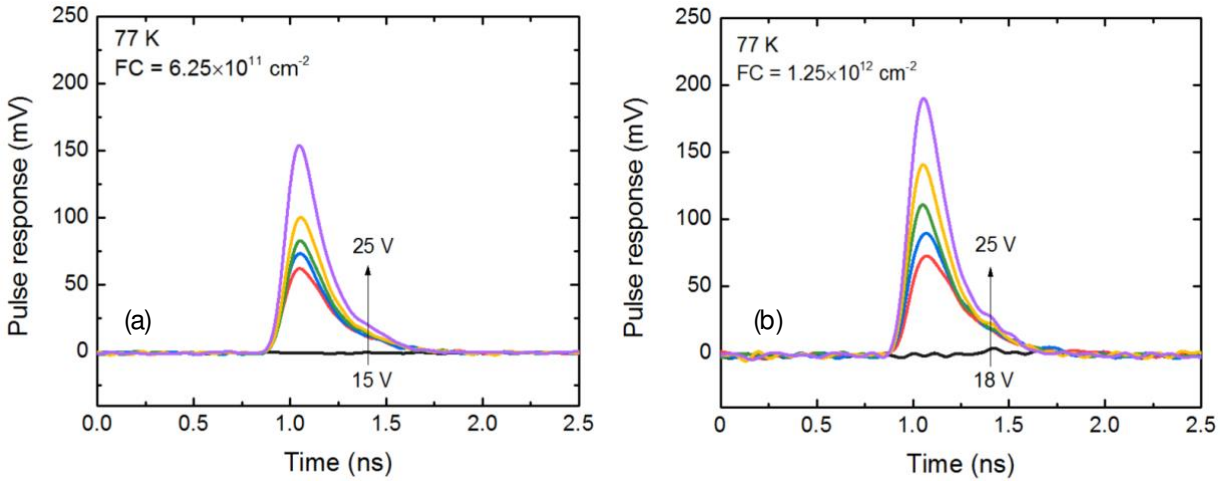

Figure 6-11 Temporal response of the GaSb/AlAsSb devices with FC charge density of 6.25×10^{11} cm^{-2} and 1.25×10^{12} cm^{-2}.

The pulse rise time is measured from 10% to 90% of the pulse amplitude, which maintains approximately 100-110 ps for both devices with increasing reverse bias (Fig. 6-12). In a photodetector, the important processes that can limit the response time include: (1) drift component of carriers generated in the depletion region; (2) diffusion component of carriers generated outside of the depletion region; (3) the effect of the RC circuit; (4) avalanche build-up time if the carriers were experiencing impact ionization. The rise time is found unaffected by the excitation optical power and the reverse bias, suggesting that the avalanche build-up time is not limiting the device response. In addition, because the GaSb absorption region is partially depleted, the drift component is not expected to be the limiting factor. The diffusion time of electrons traveling from the generated location to the edge of the depletion region is given by $\tau_{diff} = \frac{4x^2}{\pi^2 D_e}$[10], where x is the diffusion distance and D_e is the diffusion coefficient of electrons in GaSb[11]. The diffusion time is

a strong function of diffusion distance which decreases continuously with increasing reverse bias. However, the measured rise time is nearly constant with the increasing reverse bias, suggesting that the response of the device is not determined by the diffusion component. As a result, the effect of the RC circuit is concluded as the dominant factor that limits the response time of the GaSb/AlAsSb devices, as shown in Fig. 6-12. Devices with smaller size suffer less from the RC-limited response as they have smaller capacitance, but, unfortunately, their temporal response measurements are not allowed on this device mask for further investigation.

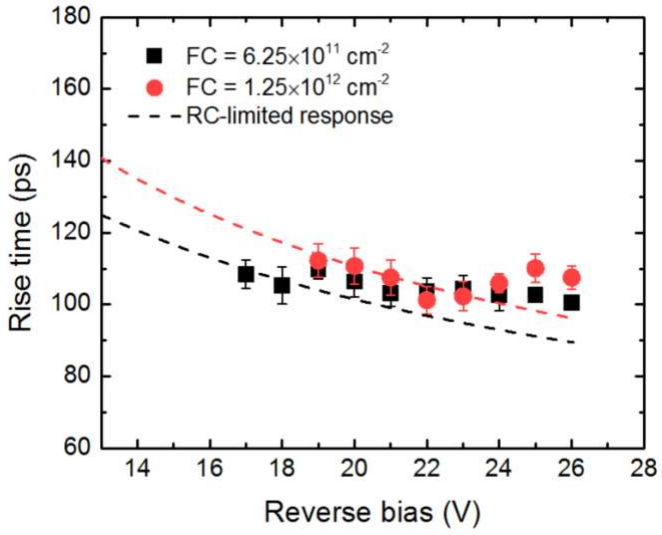

Figure 6-12 Measured pulse rise time of the GaSb/AlAsSb devices as a function of reverse bias at 77 K.

6.5 X-ray and gamma-ray response

6.5.1 Packaged device characteristics

It is shown that the GaSb/AlAsSb devices with the FC charge density of 1.25×10^{12} cm^{-2} have a lower dark current floor and a preferred electric field distribution in comparison to the other device samples. As a result, the best performing 1.25×10^{12} cm^{-2} devices are selected and prepared for the radiation measurements. Fig. 6-13 shows the representative dark I-V curves of the 200-µm-

diameter GaSb/AlAsSb devices. The packaged devices have generally shown an increased dark current level by about 25-fold difference than the on-chip device. This is likely due to the degradation caused by the packaging process (e.g. epoxy curing and wire-bonding). The optimum shaping time of 1 μs was chosen, determined by the lowest attainable pulser FWHM, for all the spectroscopy measurement discussed later if not mentioned otherwise.

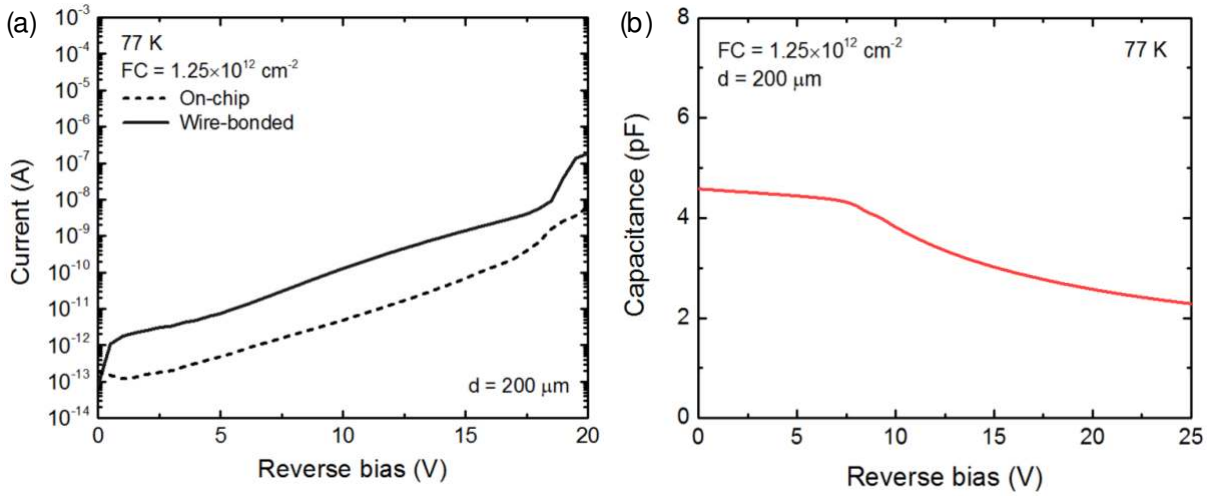

Figure 6-13 (a) Dark I-V curves before (dashed) and after (solid) wire-bonding and (b) the C-V curve of the 1.25×10^{12} cm^{-2} GaSb/AlAsSb device.

6.5.2 ^{241}Am spectra and carrier collection

The packaged 1.25×10^{12} cm^{-2} GaSb/AlAsSb devices are tested with the 0.74 MBq ^{241}Am radioactive source at 77 K, and the spectra obtained under different reverse biases are shown in Fig. 6-14. Different stages of carrier collection can be observed by the progression of obtained photopeaks in MCA channels with increasing reverse bias, and the pulser signals are used as the reference. It is shown that the photopeaks are registered at approximately identical MCA channels when the devices are biased below V_{reach} (i.e. 7.5 V), suggesting that the edge of depletion region is confined within the AlAsSb region. As a result, only carriers generated in the AlAsSb region are collected at the device output, as shown in Fig. 6-14. With increasing reverse bias beyond

V_{reach}, the electric field has depleted through the GaSb-AlAsSb interface and extended into the GaSb region. Photopeak signals registered at larger channel numbers start to take place with increasing counts, indicating the carriers generated in the GaSb region are now "observed." When

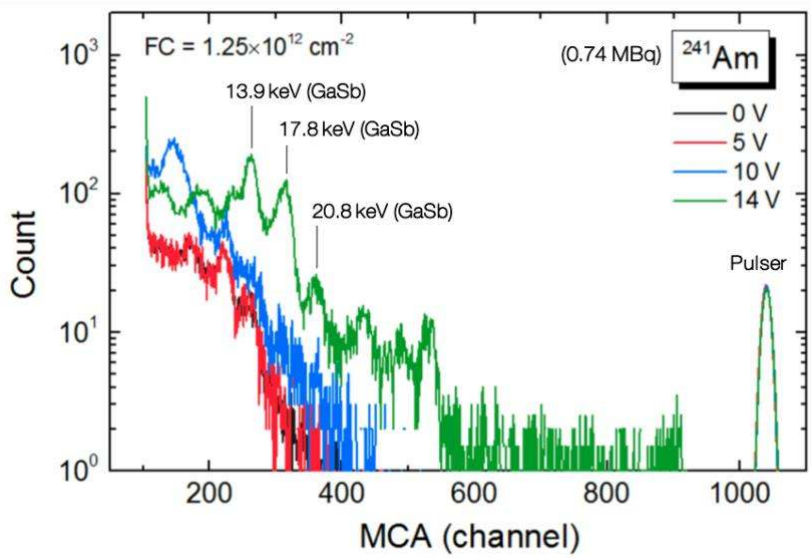

Figure 6-14 0.74 MBq ^{241}Am spectra obtained by the GaSb/AlAsSb device at difference reverse biases. The pulser peaks are also shown as the reference to observe the progression of photopeaks.

the effective electric field strength within the GaSb region achieves a sufficient level, e.g., at a reverse bias of 14 V beyond V_{col}^{0}, the carriers can be efficiently collected and result in well-defined photopeaks of all signature energy lines, i.e. 13.9 keV (GaSb), 17.8 keV (GaSb), and 20.8 keV (GaSb), in the obtained energy spectrum.

Fig. 6-15 shows a detailed comparison of the ^{241}Am obtained by the device at the reverse bias of 0 V and 14 V. At zero bias, the GaSb region is not active, and the observed photopeaks are generated by the AlAsSb region. On the other hand, the photopeaks from the carriers generated by the GaSb region become dominant at 14 V. The AlAsSb and GaSb PCE values at 77 K have been extracted as discussed in the previous chapters, and the relationships of the relative photopeak

channels created by the same energy lines between two materials can be used to evaluate the carrier collection efficiency. Indeed, the anticipated photopeak channels calculated based on the ratio of their PCE values agree with the measured photopeak channels at the corresponding energy lines with an error of 4%, indicating a high degree of carrier collection efficiency of the device.

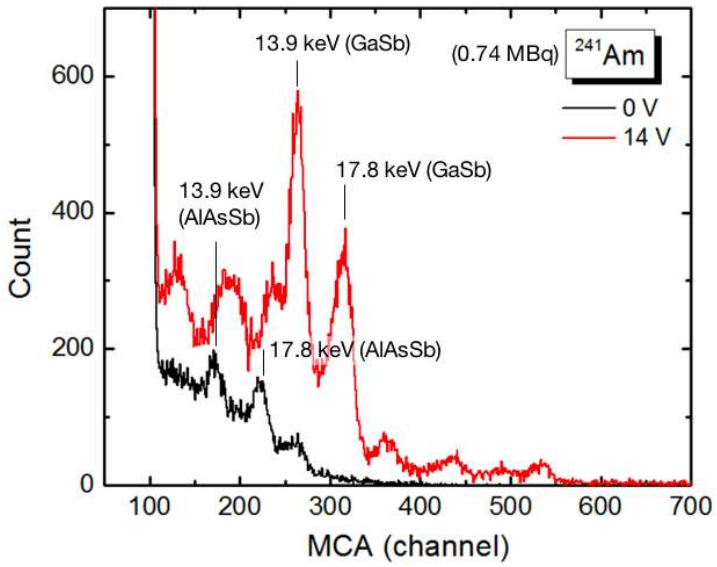

Figure 6-15 ^{241}Am spectra obtained by the GaSb/AlAsSb device at 0 V and 14 V, which photopeaks of the same energy lines are registered at different channel numbers.

6.5.3 Energy resolution at 59.5 keV

The gamma-ray response at 59.5 keV is also measured by using the 1.55 GBq ^{241}Am radioactive source to obtain better statistics. The GaSb/AlAsSb device exhibits a noise floor at approximately 2.8 keV, and the energy line at 59.5 keV can be clearly resolved, as shown in Fig. 6-16(a). The minimum FWHM of 1.283±0.082 keV at 59.5 keV is obtained when the device is reverse biased at 14 V. The obtained energy resolution shows a substantial improvement in comparison to that of the GaSb PIN device as depicted in Fig. 6-16(b). Besides the energy line at 59.5 keV, other photopeaks obtained in the energy spectrum can be clearly identified and are similar to those observed in the spectra created by the GaSb PIN device[12], including the Ga Kα

escape peak at 50.3 keV, Sb Kα escape peak at 33.2 keV, Sb Kβ escape peak at 29.8 keV, Sb Kα characteristic X-ray peak at 26.3 keV, Ga Kα escape peak at 17.1 keV, and Ga Kα characteristic

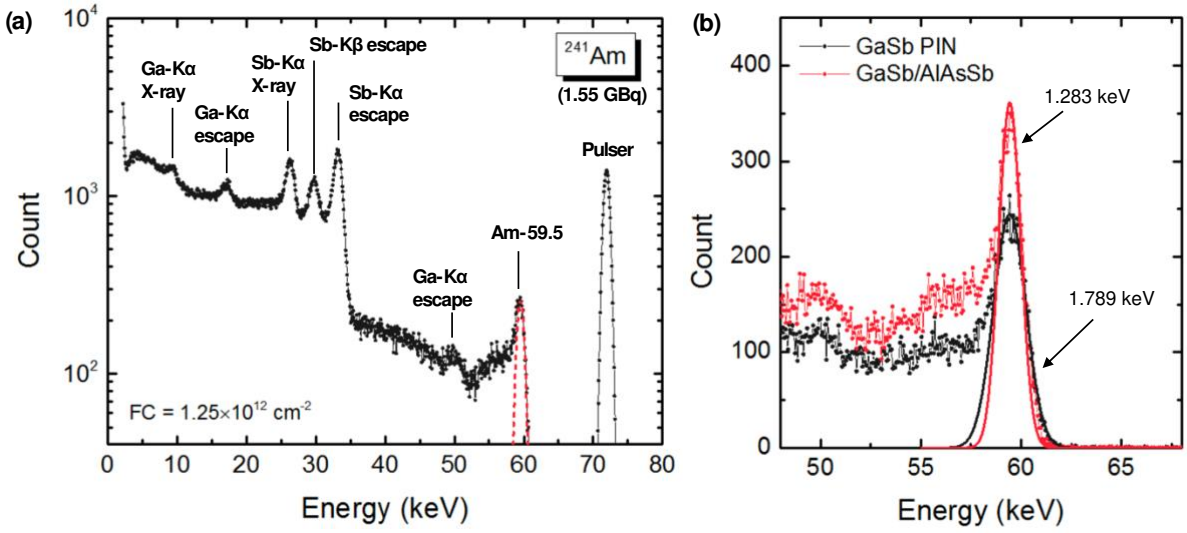

Figure 6-16 (a) 1.55 GBq ^{241}Am spectrum obtained by the GaSb/AlAsSb device at reverse bias of 14 V at 77 K. The FWHM of 59.5 keV and pulser peaks are 1.283±0.082 keV and 1.125±0.003 keV, respectively. (b) The comparison of 59.5 keV photopeaks obtained by the GaSb PIN device and the GaSb/AlAsSb heterostructure device with the same photon counts.

X-ray peak at 9.3 keV. Interestingly, the photopeaks from the AlAsSb region are not observed in the obtained spectrum, and they are likely "buried" under the signals generated by the GaSb region once the reverse bias is beyond V_{col}. This suggests that the large difference in absorption efficiency and PCE between AlAsSb and GaSb have effectively minimized the probability of spurious photopeaks generated outside of the intended absorption region and greatly reduced the complexity of the obtained energy spectra.

6.5.4 Detection linearity

The detection linearity of the GaSb/AlAsSb device has been characterized using different energy lines from both ^{241}Am radioactive sources. The shaped pulse heights show good agreement

with corresponding photon energies, as shown in Fig. 6-17. A good detection linearity is established by utilizing linear fitting with the coefficient of determination $R^2 = 0.9999$.

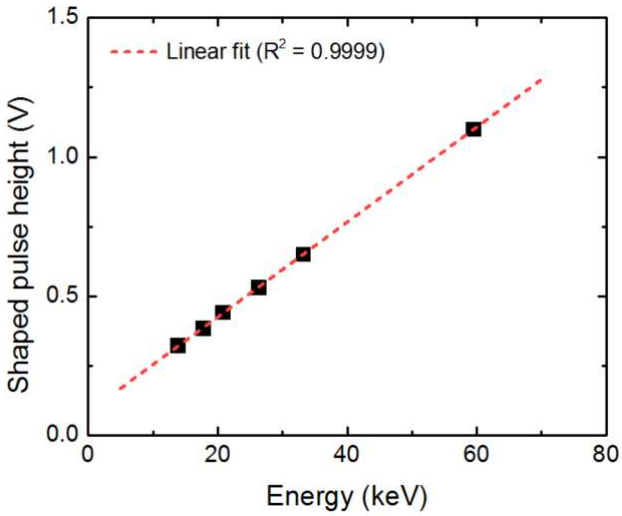

Figure 6-17 Measured shaped pulse height with the corresponding photon energies from 13.9 keV to 59.5 keV obtained by the GaSb/AlAsSb device at 77 K.

6.5.5 Noise analysis and device performance

The measured 59.5 keV energy resolution is observed to continue improving with increasing reverse bias, and the photopeak FWHM has reached a minimum at 14 V, as shown in Fig. 6-18. With a further increased reverse bias, the measured photopeak FWHM begins to gradually broaden again. The device noise characteristics have also been studied by decoupling the noise components as a function of reverse bias, as shown in Fig. 6-19. The device shows a nearly unchanged electronic noise component from the reverse bias of 14 V to 17 V, suggesting that the electronic noise is primarily limited by the dark current of input FET and the stray capacitance in the system rather than the noise components from the device. The extracted excess noise has shown to minimized around 13-15 V. This can be understood as the result of a high degree of carrier collection. For this reason, the relatively large excess noise presented at the low

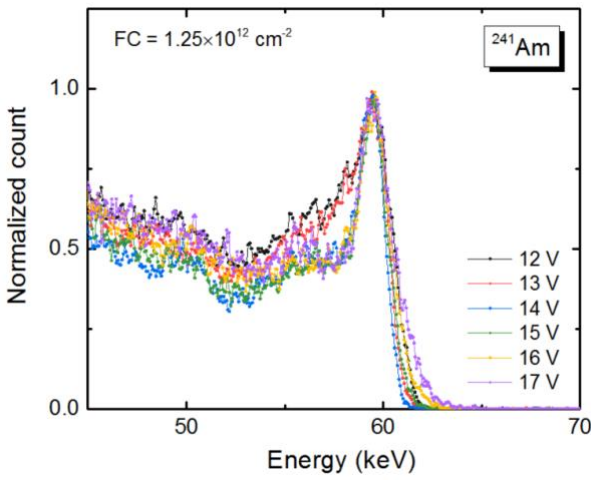

Figure 6-18 Photopeak FWHM at 59.5 keV as a function of reverse bias obtained by the GaSb/AlAsSb device.

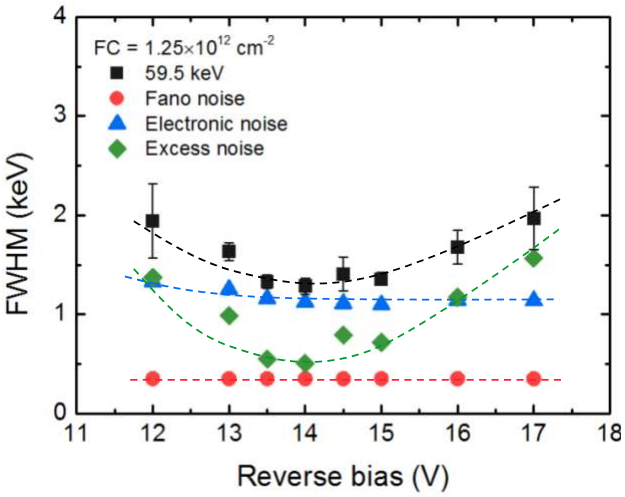

Figure 6-19 Contribution of each noise component as a function of reverse bias for the GaSb/AlAsSb device.

bias range is considered as the result of incomplete carrier collection while electric field in the GaSb region has not reached the level to provide sufficient kinetic energy for efficient carrier transport. The excess noise begins to increase from 15 V with increasing reverse bias. However, the similar trend is not observed for 33.2 keV photopeak, whose excess noise component (1.13±0.05 keV) maintains relatively unaffected up to 17 V. This suggests that the increase of the 59.5 keV is not likely due to the avalanche process in the GaSb region.

The improved energy resolution at 59.5 keV is mainly attributed to the reduced excess noise. A minimum excess noise of 508 eV is achieved at 14 V, which is significantly smaller than the 1245 eV obtained by the GaSb PIN device at 2 V. Fig. 6-20 shows the simulated electric field distributions in the GaSb/AlAsSb device and the GaSb PIN device under the aforementioned bias conditions. It is shown that the heterostructure device architecture has effectively minimized the electric field strength in the GaSb region, which suppressed the field-assisted process and thus the

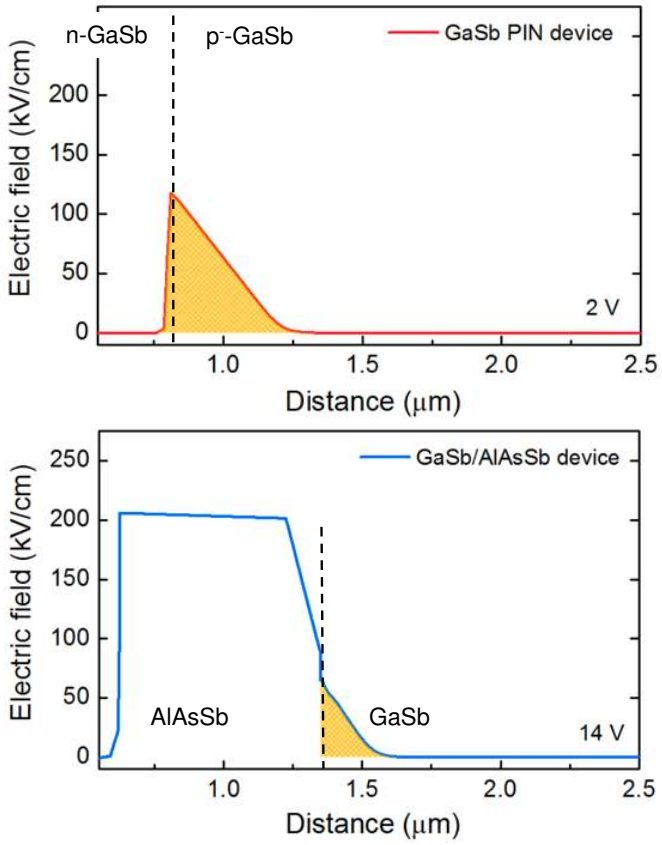

Figure 6-20 Electric field distributions of the GaSb/AlAsSb device at reverse bias of 14 V and the GaSb PIN device at 2 V. The shaded area indicates the GaSb region.

excess noise. Although the device signal-to-noise ratio (SNR) is limited by the surface leakage current in the GaSb/AlAsSb device, the intrinsic SNR of carriers generated in the GaSb region is expected to increase since the effect of field-enhanced SRH and BTBT process are both reduced with the improved electric field distribution. Furthermore, there is no apparent energy dependence on excess noise. This suggests that incomplete carrier collection is not the limiting factor, and the AlGaSb window layer has effectively suppressed the carrier loss via surface recombination, as shown in Fig. 6-21. The relatively large excess noise at low-energy range is likely due to the disturbance from the background signals generated within the AlAsSb region.

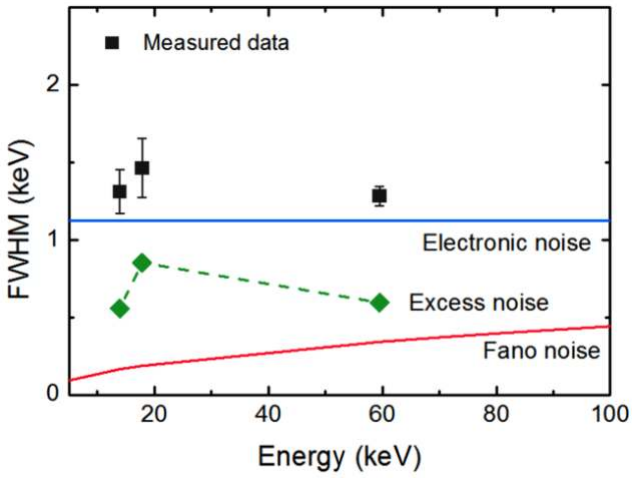

Figure 6-21 Energy dependence of the measured photopeak FWHM and the separated noise contributions obtained by the GaSb/AlAsSb device at 14 V.

The measured pulser FWHM of 1.125±0.003 keV (163 electron rms) indicates the electronic noise present during the radiation measurement. The pulser FWHM is relatively unchanged against reverse bias, suggesting that this level of electronic noise is essentially the minimum limit attainable by the readout electronics and the major noise sources are generated by the charge-sensitive amplifier. If the electronic noise can be further minimized, e.g. to the level of <20 electron rms as achieved by Bertuccio et al.[13,14], an estimated photopeak FWHM as narrow as 627 eV could be obtained at 59.5 keV by the GaSb/AlAsSb devices.

6.6 Discussion

In summary, we have demonstrated the proof-of-concept device by using the heterostructure architecture based on the high-Z GaSb absorber and the low-Z, large-bandgap AlAsSb junction region for energy-sensitive X-ray and gamma-ray detection. Previously, X-ray energy spectra using the SAM device structure based on GaAs/AlGaAs material systems have been developed; however, only the photopeaks with energies lower than 26.4 keV have been

reported. This work has presented the first attempt to perform the direct gamma-ray detection at 59.5 keV, and the ^{241}Am energy spectra with a well-defined photopeak at 59.5 keV have been demonstrated and characterized. By changing the reverse bias (i.e. electric field distribution), photopeaks generated by different stages in the device can be observed, indicating that the GaSb/AlAsSb material system has effectively overcome the carrier collection issue found in the GaSb/GaAs material system. In addition, the noise analysis also shows a minimum excess noise of 508 eV is obtained at the optimum bias condition, much smaller than the 1245 eV obtained by the GaSb PIN device structure, suggesting an effective improvement in energy resolution. The GaSb/AlAsSb device has exhibited a minimum photopeak FWHM of 1.283±0.082 keV at 59.5 keV, and further improvement is possible since the performance is found primarily limited by the readout electronics.

6.7 Reference

1. Lauter, J., Protić, D., Förster, A. & Lüth, H. AlGaAs/GaAs SAM-avalanche photodiode: An X-ray detector for low energy photons. *Nucl. Instruments Methods Phys. Res. Sect. A Accel. Spectrometers, Detect. Assoc. Equip.* **356,** 324–329 (1995).

2. Gomes, R. B., Tan, C. H., Meng, X., David, J. P. R. & Ng, J. S. GaAs/$Al_{0.8}Ga_{0.2}As$ avalanche photodiodes for soft X-ray spectroscopy. *J. Instrum.* **9,** P03014 (2014).

3. Forrest, S. R., Kim, O. K. & Smith, R. G. Optical response time of $In_{0.53}Ga_{0.47}As$/InP avalanche photodiodes. *Appl. Phys. Lett.* **41,** 95–98 (1982).

4. Campbell, J. C., Dentai, A. G., Holden, W. S. & Kasper, B. L. High-performance avalanche photodiode with separate absorption 'grading' and multiplication regions. *Electron. Lett.* **19,** 818–820 (1983).

5. Dutta, A. K., Dutta, N. K. & Fujiwara, M. *WDM technologies: Passive optical components*. **1,** (Academic press, 2003).

6. Bowers, J. E. & Wey, Y. G. High-speed photodetectors. *Handb. Opt.* **1,** 11–17 (1995).

7. Forrest, S., Smith, R. & Kim, O. Performance of $In_{0.53}Ga_{0.47}As$/InP avalanche photodiodes. *IEEE J. Quantum Electron.* **18,** 2040–2048 (1982).

8. Matsushima, Y. *et al.* High-speed-response InGaAs/InP heterostructure avalanche photodiode with InGaAsP buffer layers. *Electron. Lett.* **18,** 945–946 (1982).

9. Campbell, J. C., Tsang, W. T., Qua, G. J. & Bowers, J. E. InP/InGaAsP/InGaAs avalanche photodiodes with 70 GHz gain-bandwidth product. *Appl. Phys. Lett.* **51,** 1454–1456 (1987).

10. Sze, S. M. & Ng, K. K. *Physics of semiconductor devices*. (John Wiley & Sons, 2006).

11. Institute, I. Gallium Antimonide. Available at: http://www.ioffe.ru/SVA/NSM/Semicond/GaSb/index.html.

12. Bor-Chau, J., David, L. P., Baolai, L., Arion, F. C. & Diana, L. H. Characterization of GaSb photodiode for gamma-ray detection. *Appl. Phys. Express* **9,** 86401 (2016).

13. Bertuccio, G., Rehak, P. & Xi, D. A novel charge sensitive preamplifier without the feedback resistor. *Nucl. Instruments Methods Phys. Res. Sect. A Accel. Spectrometers, Detect. Assoc. Equip.* **326,** 71–76 (1993).

14. Bertuccio, G. *et al.* Noise analysis of gallium arsenide pixel X-ray detectors coupled to ultra-low noise electronics. *IEEE Trans. Nucl. Sci.* **50,** 723–728 (2003).

7. Conclusions and future work

7.1 Conclusions

This dissertation has demonstrated the potential and the possibility of using heterostructure device architecture to achieve the energy-sensitive radiation detectors for X-ray and gamma-ray spectrometry. In comparison to the conventional homojunction semiconductor detectors, which spectroscopic performance is limited by the intrinsic properties of the detector material, the proposed device architecture is shown to bypass intrinsic limitations of the GaSb. The device concept of integrating high-Z, small-bandgap absorption region and low-Z, large-bandgap junction region is realized using the GaSb/AlAsSb material system. The integration of the large-bandgap AlAsSb material has effectively improved the energy resolution by eliminating the excess noise

introduced by the surface recombination and the field-assisted process in the small-bandgap GaSb. The direct detection of gamma-ray energy up to 59.5 keV with a well-defined photopeak has been demonstrated at 77 K. While the finite surface leakage current is the dominant factor that limits the device dark current floor, it is shown that the signal-to-noise ratio is not limited by the GaSb absorber and a further improvement in spectroscopic performance is possible.

7.2 Suggestions for future work

The GaSb/AlAsSb device has exhibited an energy resolution of 1.283 keV FWHM at 59.5 keV, and the photopeak broadening is primarily limited by the electronic noise of the readout circuit (1.125keV, 163electron rms). The projected energy resolution of 627 eV FWHM at 59.5 keV could be obtained if the electronic noise was reduced to the state-of-the-art level (< 20 electron rms), as discussed in chapter 6. To achieve an electronic noise as low as such, the preamplifier stage (i.e. charge-sensitive amplifier) is as essential as the detector stage. The current and voltage noise components generated by the preamplifier strongly affects the overall SNR and commonly act as dominant noise sources in the spectroscopic measurements. Several groups have developed preamplifiers which rely on methods other than feedback resistors to discharge the charge-integrating capacitor, resulting in a significantly improved electronic noise. In addition, guidelines and criteria for constructing a low-noise preamplifier have been reported[1–3]. The development of the preamplifier is outside the scope of this work, but we recognize that employing a preamplifier with the optimized design will offer a great advantage of achieving high energy resolution spectroscopy.

In chapter 6, the measurement temperature of the GaSb/AlAsSb devices has been limited to 77 K to obtaining a sufficiently low dark current, mainly due to the existence of surface leakage current. It is well-known that Sb-based devices suffer from leakage current flowing through sidewall surfaces. Different methods were investigated to reduce the surface leakage current, and the most commonly used techniques are through optimizing etching chemistry or passivation treatment. The device fabrication adopted in this work utilizes dry-etching method based on BCl_3/Ar chemistry followed by the aqueous $(NH_4)_2S$ passivation, which has shown effective reduction in the surface leakage component. However, further optimization is still required to remove the surface leakage current in the Sb-based heterostructure devices to allow a higher working temperature. Besides the approach based on device fabrication, the surface leakage current could potentially be improved by incorporating a small amount of Ga content in the AlAsSb alloy[4]. The experimental results reported recently by Zhou et al. has shown that adding 10% of Ga in the quaternary AlGaAsSb alloy has effectively reduced the dark current by nearly two orders of magnitude, whereas the material bandgap only decreases by 3%[5]. This introduces an intrinsic solution to improve the material's susceptibility to oxidization, leading to an increased device working temperature and a more reliable device fabrication.

Furthermore, the large-bandgap, low-Z material in the heterostructure device can not only accommodate the substantial part of the electric field to eliminate the field-assisted current components in GaSb but also offer avalanche gain to further increase the magnitude of detected signals at the device output. The enhanced signal strength is expected to reduce the influence of the baseline fluctuation from the readout electronics and loosen the stringent requirements on the charge sensitive preamplifier, i.e., selection and working condition of the input FET. To enable this study, a higher FC charge density (but lower than 3.75×10^{12} cm^{-2}) will be required to promote

avalanche gain in the AlAsSb region with a reverse bias near V_{col}^{0}. On the other hand, it is possible to incorporate a compositional grading layer to connect the small-bandgap absorption region and the large-bandgap junction region to improve carrier transport across the heterointerface[6–9]. This could effectively decrease the value of V_{col}^{0} and provide enhanced flexibility in the field-control design. With an optimal electric field distribution, an improved spectroscopic performance is possible with the Sb-based devices operating in the APD mode[10–12]. It should be noted that the APD excess noise is also known to influence the device's spectroscopic performance[13], and quantifying these complicated trade-offs will require more experimental observations.

Finally, the device structures adopted in this work consist of a relatively thin absorption region intended for device research. The energy lines up to 59.5 keV were obtained thanks to the high Z of GaSb. It is also desirable to increase the X-ray and gamma-ray absorption efficiency to reduce the effective measurement time and extend the detector sensitivity towards a higher photon energy. The absorption efficiency can always be increased by adding the absorber volume, but it could also increase the probability of incomplete carrier collection such as hole-tailing effect reported in Cd(Zn)Te detectors[14,15]. Long carrier diffusion time also increases the risk of charge trapping and recombination, resulting in an increased excess noise and thus a degraded energy resolution. Since the carrier collection of the Sb-based devices would rely on a combination of diffusion and drift components, the carrier diffusion length (~60 μm) of GaSb could potentially become a limiting factor to the largest attainable absorber thickness. Nevertheless, for an energy-sensitive radiation detector, the energy resolution is of greater interest for detection of radioactive decay signatures, and all the factors must be taken in to account for designing the Sb-based heterostructure devices with an increased absorption region thickness.

7.3 Reference

1. Bertuccio, G., Rehak, P. & Xi, D. A novel charge sensitive preamplifier without the feedback resistor. *Nucl. Instruments Methods Phys. Res. Sect. A Accel. Spectrometers, Detect. Assoc. Equip.* **326,** 71–76 (1993).

2. Bertuccio, G., Pullia, A. & De Geronimo, G. Criteria of choice of the front-end transistor for low-noise preamplification of detector signals at sub-microsecond shaping times for X- and γ-ray spectroscopy. *Nucl. Instruments Methods Phys. Res. Sect. A Accel. Spectrometers, Detect. Assoc. Equip.* **380,** 301–307 (1996).

3. Lioliou, G. & Barnett, A. M. Electronic noise in charge sensitive preamplifiers for X-ray spectroscopy and the benefits of a SiC input JFET. *Nucl. Instruments Methods Phys. Res. Sect. A Accel. Spectrometers, Detect. Assoc. Equip.* **801,** 63–72 (2015).

4. Reddy, M. H. M. *et al.* $Al_{0.95}Ga_{0.05}As_{0.56}Sb_{0.44}$ for lateral oxide-confinement layer in InP-based devices. *Appl. Phys. Lett.* **82,** 1329–1331 (2003).

5. Zhou, X., Zhang, S., David, J. P. R., Ng, J. S. & Tan, C. H. Avalanche Breakdown Characteristics of $Al_{1-x}Ga_xAs_{0.56}Sb_{0.44}$ Quaternary Alloys. *IEEE Photonics Technology Letters* **28,** 2495–2498 (2016).

6. Campbell, J. C., Dentai, A. G., Holden, W. S. & Kasper, B. L. High-speed InP/InGaAsP/InGaAs avalanche photodiodes. in *1983 International Electron Devices Meeting* **29,** 464–467 (1983).

7. Matsushima, Y., Sakai, K. & Noda, Y. New type InGaAs/InP heterostructure avalanche photodiode with buffer layer. *IEEE Electron Device Lett.* **2,** 179–181 (1981).

8. Forrest, S. R., Kim, O. K. & Smith, R. G. Optical response time of $In_{0.53}Ga_{0.47}As$/InP

avalanche photodiodes. *Appl. Phys. Lett.* **41,** 95–98 (1982).

9. Pellegrini, S. *et al.* Design and performance of an InGaAs-InP single-photon avalanche diode detector. *IEEE J. Quantum Electron.* **42,** 397–403 (2006).

10. Lauter, J., Protić, D., Förster, A. & Lüth, H. AlGaAs/GaAs SAM-avalanche photodiode: An X-ray detector for low energy photons. *Nucl. Instruments Methods Phys. Res. Sect. A Accel. Spectrometers, Detect. Assoc. Equip.* **356,** 324–329 (1995).

11. Meng, X. *et al.* InAs avalanche photodiodes as X-ray detectors. *J. Instrum.* **10,** P10030 (2015).

12. Chee Hing Tan *et al.* Avalanche Gain and Energy Resolution of Semiconductor X-ray Detectors. *IEEE Trans. Electron Devices* **58,** 1696–1701 (2011).

13. Gomes, R. B., Tan, C. H., Meng, X., David, J. P. R. & Ng, J. S. GaAs/$Al_{0.8}Ga_{0.2}As$ avalanche photodiodes for soft X-ray spectroscopy. *J. Instrum.* **9,** P03014 (2014).

14. Takahashi, T. & Watanabe, S. Recent progress in CdTe and CdZnTe detectors. *Nucl. Sci. IEEE Trans.* **48,** 950–959 (2001).

15. Schlesinger, T. E. *et al.* Cadmium zinc telluride and its use as a nuclear radiation detector material. *Mater. Sci. Eng. R Reports* **32,** 103–189 (2001).

Appendix A. Device fabrication

1. Rinse the device sample with acetone, methanol, and isopropanol for degreasing every time prior to photolithography, and blow dry with nitrogen spray gun.
2. Pattern the device sample with mesa mask using AZ-5214E photoresist[a].
3. Etch the device sample using BCl_3/Ar (50:10 sccm, RF power = 800W) recipe in the Unaxis SLR 770 etcher to the desired device layer. Measure the etched depth of the device sample using the Dektak profiler[b].
4. Pattern the device sample with the contact mask for n-type GaSb layer using AZ-5214E positive photoresist.
5. Bottom contact deposition Ni/Ge/Au (100:550:1500 Å) using e-beam evaporator[c]. Lift-off with acetone.
6. Anneal the device sample at 280-300ºC for 30 seconds to improve the contact resistance. Check the I-V curves to ensure the contact exhibits ohmic behavior and perform TLM measurement to extract the contact resistivity (typically $<5\times10^{-4}$ $\Omega\cdot cm^2$).
7. Pattern the device sample with the contact mask for p-type GaSb layer using AZ-5214E positive photoresist.
8. Top contact deposition Ti/Pt/Au (500:500:1000 Å) using e-beam evaporator. Lift-off with acetone. Check the I-V curves to ensure the contact exhibits ohmic behavior and perform TLM measurement to extract the contact resistivity (typically $<6\times10^{-6}$ $\Omega\cdot cm^2$).
9. Pattern the device sample with the passivation mask for p-type GaSb layer using AZ-5214E photoresist.

10. Prepare $HCl:H_2O:H_2O_2$ (100:100:1) etchant and $(NH_4)_2S:H_2O$ (1:4) solution, and wait at least 15 minutes for the etchants to settle down.
11. Dip the device sample in the HCl etchant for 30 seconds, wash the sample in deionized water for 5 seconds, then place the sample in the $(NH_4)_2S$ bath for 15 minutes.
12. Remove the device sample from the $(NH_4)_2S$ bath, and blow dry with nitrogen.
13. Rinse the device sample with acetone and isopropanol, and blow dry with nitrogen.

[a] After patterning, it is recommended to perform the descum process using oxygen plasma to remove residual photoresist in the developed area.

[b] After every process, it is recommended to perform plasma stripping process (at 200ºC) to ensure the complete removal of photoresist on the device sample.

[c] 30 seconds $HCl:H_2O$ (1:1) etch is used for oxide removal before loading the device sample into the evaporator.

Appendix B. Radiation measurement

B.1 Measurement system setup

In the X-ray and gamma-ray measurement, current pulses are produced at the detector output with varying amplitudes depending on the incident photon energy. The pulses are then amplified and transformed via the readout electronics to a series of voltage pulses to facilitate the signal digitalization and extraction of the energy information. The signal processing chain includes a charge-sensitive amplifier (Amptek A250CF), a spectroscopy amplifier (ORTEC 673) performing semi-Gaussian pulse-shaping, and a multi-channel analyzer (Amptek MCA-8000D). A pulse generator (Berkeley Nucleonics Model BH-1) is also used prior and during the measurement to provide a direct measure to the contribution of electronic noise. The diagram of the measurement system is shown in Fig. B-1.

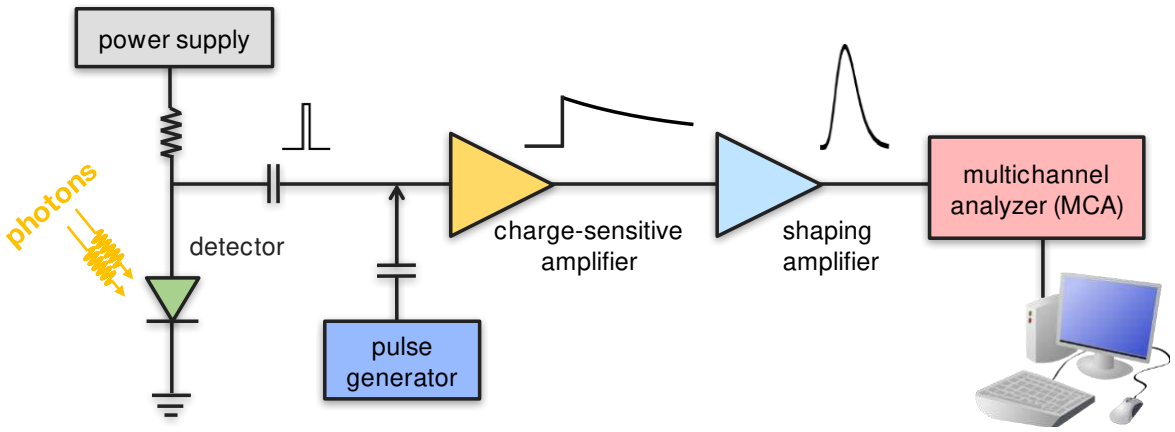

Figure B-1 The radiation measurement system, including a power supply, a charge-sensitive amplifier, a pulse-shaping amplifier, a multichannel analyzer, and a computer. The pulse generator is also used to produce a test pulse fed into the test input of the preamplifier in order to provide a measure of the electronic noise presents in the system.

B.1.1 Radioactive sources

In this work, two primary radioactive sources, ^{55}Fe and ^{241}Am, were used for X-ray and gamma-ray measurement, respectively. A ^{55}Fe source with radioactivity of 44 kBq (~1.18 μCi, calibrated in 2015), which the active aperture has a diameter of 1 cm, is used for low-energy X-ray spectroscopy. The ^{55}Fe decays to ^{55}Mn with a half-life of 2.7 years. The signature emissions of the source include Mn Kα X-ray at 5.9 keV (probability: 25.4%), and Mn Kβ X-ray at 6.49 keV (probability: 3.4%)[1]. On the other hand, a 0.74 MBq (~20 μCi, calibrated in 2006) ^{241}Am source is used for high-energy X-ray and gamma-ray measurement. The signature emission from the ^{241}Am include Np Lα X-ray at 13.9 keV (probability: 9.6%), Np Lβ X-ray at 17.8 keV (probability: 7.1%), Np Lγ X-ray at 20.8 keV (probability: 1.39%), and primary gamma decays of 26.3 keV (probability: 2.4%) and 59.5 keV (probability: 35.9%). In addition, another ^{241}Am source with stronger activity of 1.55 GBq (~42 mCi, calibrated in 2006) has also been used to increase the counting statistics of 59.5 keV gamma-rays, whereas the low-energy emissions are effectively scattered or attenuated through the source packaging.

B.1.2 Charge-sensitive amplifier

The primary function of the charge-sensitive amplifier (hereafter preamplifier) is to extract the signal from the detector and provide the first stage amplification for subsequent signal processing. When a given quantity of charges are produce by the detector, the preamplifier performed charge integration through its feedback capacitor C_f (Fig. B-2) and generate a voltage pulse at the output. A feedback resistor R_f is often used to discharge the capacitor to return the output voltage to the original baseline. The gain of the preamplifier is determined by the inverse of the feedback capacitor, and the amplitude of the output signal is proportional to the total

integrated charge, as long as the duration of the input pulse is significantly shorter than the decay time constant $R_f C_f$.

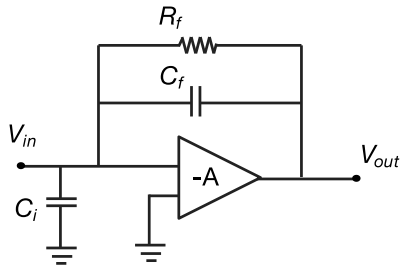

Figure B-2 Example of a simplified charge-sensitive amplifier.

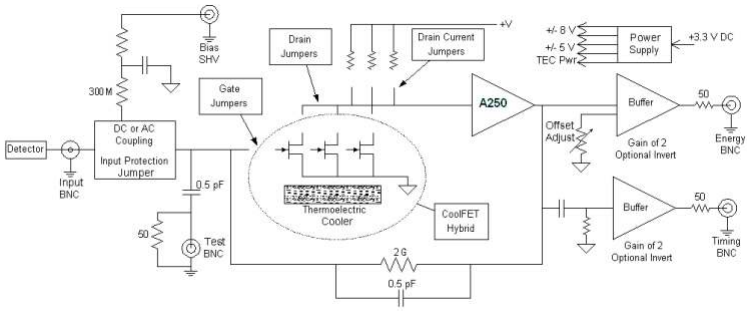

Figure B-3 Block diagram of the charge-sensitive amplifier (A250CF, Amptek Inc.) used in the measurement system[2].

The block diagram of the preamplifer used in this work is shown in Fig. B-3, which includes front-end field-effect transistors (FET), a feedback capacitor C_f $(= 0.5\,pF)$, and a feedback resistor R_f $(= 1G\Omega)$. The signal of the detector is fed to an input FET of the preamplifier, whose noise also plays an important role in the total electronic noise in addition to intrinsic noise form the detector. The maximize signal-to-noise ratio (SNR) can be achieved by having a detector capacitance comparable with input capacitance of the FET[3]. This is because the transconductance of the FET, which is proportional to the capacitance of the FET, is desired to be as high as possible to reduce the noise of preamplifier. However, a high FET capacitance also increased the total input capacitance and thus the electronic noise. The trade-off will reach an optimal point where the detector capacitance is equal to the FET input capacitance. As shown in Fig. B-3, Amptek A250CF preamplifier has three FETs to allow matching to detectors with different capacitances. FET 1 and 2 have a low capacitance of 8 pF and FET 3 has a high capacitance of 30 pF. Since the devices used in this work are generally below 15 pF at the bias voltages, FET 1 was chosen unless otherwise noted. The noise performance of the FETs is also improved by reducing its leakage

current and increasing the transconductance through the thermoelectric cooling provided by the original packaging.

Besides the noises from leakage current and input capacitance of the FET, a small R_f value can lead to significant Johnson noise contributed to the electronic noise. However, a large R_f value in turns results in a long decay time constant. The long pulse tail increases the risk of the subsequent pulses piling up on top of each other, especially at a high count rate, leading to signal distortion (Fig. B-4). An alternative approach is to build the preamplifier without R_f[4,5]. The elimination of the feedback resistor permits a significantly lower noise contribution compared with conventional resistive feedback preamplifiers.

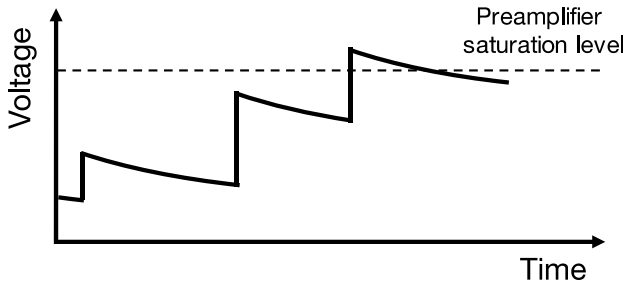

Figure B-4 Example of the pulse pile-up at the output of preamplifier. The pulse is truncated when it exceeds the preamplifier saturation level, leading to a wrongful pulse information.

B.1.3 Pulse-shaping amplifier

The primary function of a shaping amplifier (or spectroscopy amplifier) is to amplify the amplitude of pulses at the preamplifier output to the range accepted by the MCA. This could facilitate an accurate pulse-height measurement with efficient digitization. In addition, the amplifier performs semi-Gaussian pulse-shaping to the pulses to produce an improved signal-to-noise ratio while keeping the pulse height information (Fig. B-5). General configuration of a

shaping amplifier employs the CR-$(RC)^n$ circuit to reduce the bandwidth of the signal, and thus reduce the background white noise which is independent with frequency and proportional with the bandwidth. The first stage CR circuit functions as a high-pass filter (or differentiator) to effectively cut off the long pulse tail by attenuating the low-frequency components. The second stage contains

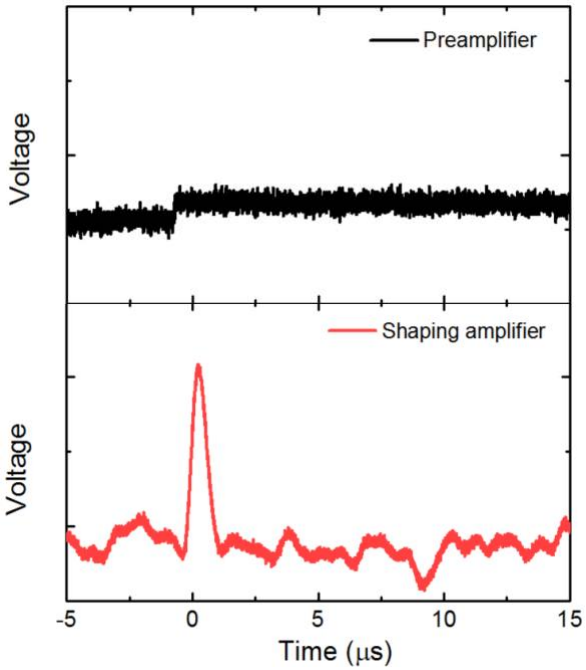

Figure C-5 Example of the output signal of preamplifier and shaping amplifier recorded by oscilloscope.

a series of RC circuits acting as low-pass filter (or integrator). The RC circuits effectively attenuate the high frequency components of the pulse, which contain excessive noise, and increase the rise time of the shaped pulse to allow the MCA to extract pulse-high information more easily. For the shaping amplifier used in this work, a more complicated active filter network is incorporated into the second stage integrator to perform a so-called "semi-Gaussian" pulse shaping[6]. This design can not only further improve the SNR, but also reduce the output pulse width closed to the baseline resulting in a reduced dead time at high counting rates.

The time constants of the high-pass and low-pass filters are typically set the same, which is the referred to shaping time constant. Choice of shaping time constant is extremely critical to achieve high energy resolution in X-ray and gamma-ray spectroscopy. The electronic noise at the preamplifier input has a great impact on the energy resolution as well as the minimum attainable energy. Since most of the electronic noise components are dependent on the shaping time (e.g., series noise and parallel noise), they can be adjusted to a minimum level by choosing an appropriate shaping time constant for the spectroscopy.

B.1.4 Multichannel analyzer

Generally speaking, MCA is an analog-to-digital converter (ADC) that provides a reliable way for pulse amplitude discrimination with counting statistics. The basic function of the MCA is to sense the arrival of an input pulse, hold the pulse-height information for digitalization, and registered the information into corresponding memory unit. The number of memory units is normally made with power of 2, and the MCA used in this work has a total number of 8192 channels. Each channel represents an addressable location in the memory units, corresponding to the different pulse amplitudes. The acceptable maximum voltage of input pulse used here is 10 V (with another option of 1 V), which is subdivided by the total channel numbers. When an input pulse is sensed, the ADC performs a linear conversion to a digital-scale output based on its maximum amplitude. The output is then registered to the address of respective channel number with incremental counts. The total counts registered in the MCA channels is equal to the total number of pulse sensed, provided that the interval between pulses is not shorter than the processing time of the ADC and the memory storage time during the entire measurement.

When the channel spectrum is generated by a detector with characterized radioactive sources, i.e., emissions with known photon energies, the energy scale can be calibrated from the

photopeaks and their corresponding channel numbers. For a good detector material, the relationship between the photopeaks and corresponding channel numbers should establish a good agreement with the linear model, $y = Ax + B$, where A and B are fitting parameters.

B.2 Electronic noise calibration

The electronic noise is defined as the fluctuation in noise charge contributed by components in the electronic chain of the measurement system. It can be attributed to various leakage current and capacitance sources present at the vicinity of the input of preamplifier stage. During the electronic noise measurement, the detector must be connected to the input of preamplifier to include the noise contribution from both its dark current and capacitance. A long tail pulse signal (e.g., time constant = 100 μs) from the pulse generator was sent to the test input of the preamplifier, and coupled to the main input of the preamplifier through a test capacitor of 0.5 pF. The variation of the pulser voltage is measured in terms of peak FWHM recorded by MCA, which can be translated into energy scale once the channel-energy relationship is determined. The equivalent noise charge (ENC) can be calculated based on the formula

$$FWHM_{elec}\ (eV) = 2.355 \cdot \varepsilon \cdot ENC_{elec}\ (electron)\ , \tag{C.1}$$

where ε is the pair creation energy of the detector material. The noise component can be further decoupled using the dependence of ENC on shaping time τ_{sh}[3,7,8,9],

$$ENC_{elec}^2 = ENC_p^2 \cdot \tau_{sh} + ENC_s^2 \cdot \frac{1}{\tau_{sh}} + (ENC_{1/f}^2 + ENC_{die}^2)\ , \tag{C.2}$$

ENC_p is the parallel noise, mainly attributed to the shot noise of leakage current originated from the detector and the FET at the preamplifier input. Another source of the parallel noise is the

preamplifier's feedback resistor. ENC_s is the series noise, attributed to the thermal noise from the current running through the channel of the FET at preamplifier input, and is proportional to the total capacitance C_{tot} at preamplifier input. C_{tot} includes the detector capacitance C_{det}, the FET capacitance C_{FET}, the feedback capacitance C_f, the test capacitance, C_t, and the stray capacitance C_s. $ENC_{1/f}$ is the flickr noise, attributed to the flickr noise from the drain current in the FET at preamplifier input. ENC_{die} is the dielectric noise, attributed to the charge noise generated by the polarization of the lossy dielectrics at the vicinity of the preamplifier input. By investigating the shaping time dependence of ENC, further understanding of the root cause of the measured electronic noise can be obtained (Fig. B-6).

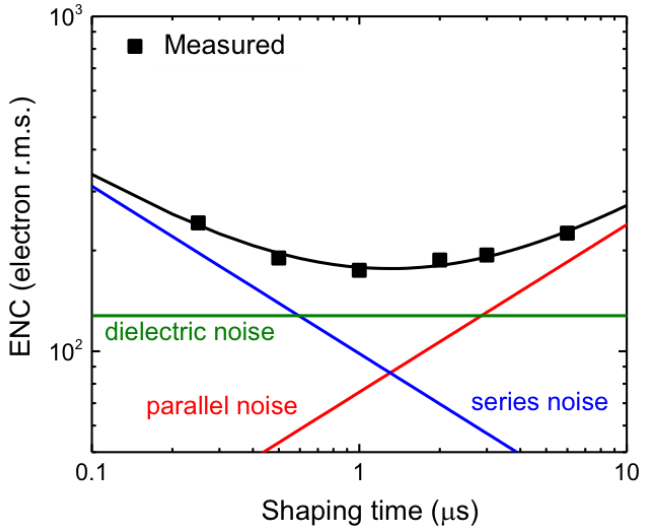

Figure B-6 Variation of the contribution of noise sources as a function of shaping time.

Baseline fluctuation contributed from the readout electronics can be calibrated by feeding the pulser signal into the preamplifier. The subsequent signal paths includes the shaping amplifier and the MCA, and the shaped output amplitude distributions provide information of the electronic noise level present in the system. The electronic noise calibration is recommended prior to the

spectroscopy measurement in order to determine the optimal shaping time. The system noise can be characterized primarily based on two cases, (1) input of the preamplifier is enclosed by a protective cap, and (2) input of the preamplifier is connected to a 2.5-inch-long coaxial cable into the cryostat chamber (as used for low-temperature measurement). The measured noise has been estimated using the FWHM values in channel numbers, as shown in Fig. B-7. In case (1), the trend of the pulser FWHM values suggests a minimum at shaping time of 1 μs. The broadening of the FWHM value is limited by current noise and voltage noise at longer and shorter shaping times, respectively. A commercial silicon PIN detector was also used to calibrate the electronic noise contributed from the A250CF preamplifier, and the result is fairly close to that provided

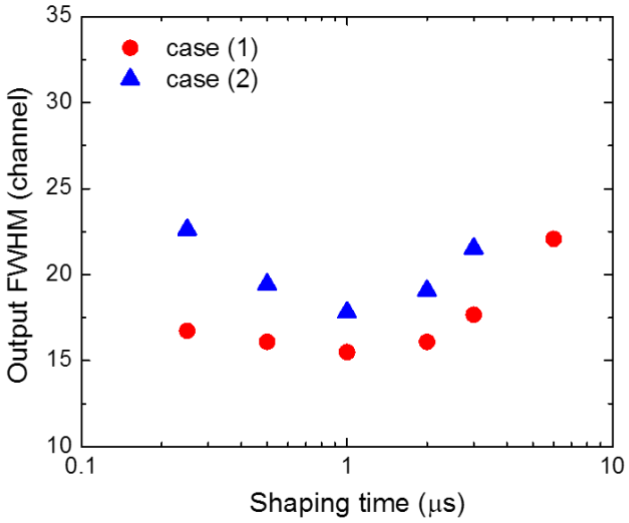

Figure B-7 FWHM values of the test pulses as a function of shaping times under different conditions.

in the specification. In case (2), the increased FWHM values at different shaping times can be attributed to the additional capacitance carried by the coaxial cable. This is evident in the larger slope in the voltage noise-limited regime, indicating the extra noise due to the increase in total capacitance. The minimum FWHM value is about 17.9 channels obtained at 1 μs. This value

suggests the minimum attainable noise floor in our setup used for spectroscopy measurement, assuming the noise contribution from the device is negligible. In practice, the electronic noise is likely to increase when the detector is connected, because the device dark current and capacitance will give rise to additional noise contributions that can also alter the optimum shaping time.

B.3 Reference

1. S.Y.F. Chu, L. P. E. and R. B. F. WWW Table of Radioactive Isotopes, database version 1999-02-28. *http://nucleardata.nuclear.lu.se/nucleardata/toi/*

2. Amptek. http://amptek.com/products/a250cf-coolfet-charge-sensitive-preamplifier/.

3. Bertuccio, G., Pullia, A. & De Geronimo, G. Criteria of choice of the front-end transistor for low-noise preamplification of detector signals at sub-microsecond shaping times for X- and γ-ray spectroscopy. *Nucl. Instruments Methods Phys. Res. Sect. A Accel. Spectrometers, Detect. Assoc. Equip.* **380,** 301–307 (1996).

4. Bertuccio, G. & Pullia, A. A method for the determination of the noise parameters in preamplifying systems for semiconductor radiation detectors. *Rev. Sci. Instrum.* **64,** 3294–3298 (1993).

5. Owens, A. *et al.* High resolution x-ray spectroscopy using GaAs arrays. *J. Appl. Phys.* **90,** 5376–5381 (2001).

6. AMETEK ORTEC. http://www.ortec-online.com/-/media/ametekortec/other/amplifier-introduction.pdf?la=en.

7. Spieler, H. *Semiconductor detector systems*. (Oxford University Press, 2008).

8. Lioliou, G. & Barnett, A. M. Electronic noise in charge sensitive preamplifiers for X-ray spectroscopy and the benefits of a SiC input JFET. *Nucl. Instruments Methods Phys. Res. Sect. A Accel. Spectrometers, Detect. Assoc. Equip.* **801,** 63–72 (2015).

9. Knoll, G. F. *Radiation detection and measurement*. (John Wiley & Sons, 2010).

Appendix C. AlAsSb DA and RA growths

The AlAsSb alloys were deposited on GaSb (001) substrates using a Veeco Gen930 solid-source MBE reactor (Fig. C-1). Prior to the material growth, the GaSb substrate temperature was raised to 535ºC for 20 minutes under a Sb_2 over pressure to desorb surface oxide. After oxide removal, the substrate was cooled to 510ºC to grow an unintentionally-doped GaSb buffer. A nominal 600 nm-thick AlAsSb layer is then grown at the same substrate temperature, followed by a 20 nm GaSb cap layer to prevent it from rapid oxidation in air. The DA sample was realized by periodically alternating the As and Sb shutter while maintaining a steady Al flux (growth rate at 0.4 ML/s) during deposition, resulting in AlSb/AlAs equivalent sequence of 4.0/0.8 MLs. Additional 4.0 MLs of AlSb was used prior to the transition to GaSb capping layer. On the other hand, the RA sample was grown by keeping Al, As, and Sb shutters open simultaneously, followed by the GaSb layer without growth interruption. The schematics of the sample structure as well as

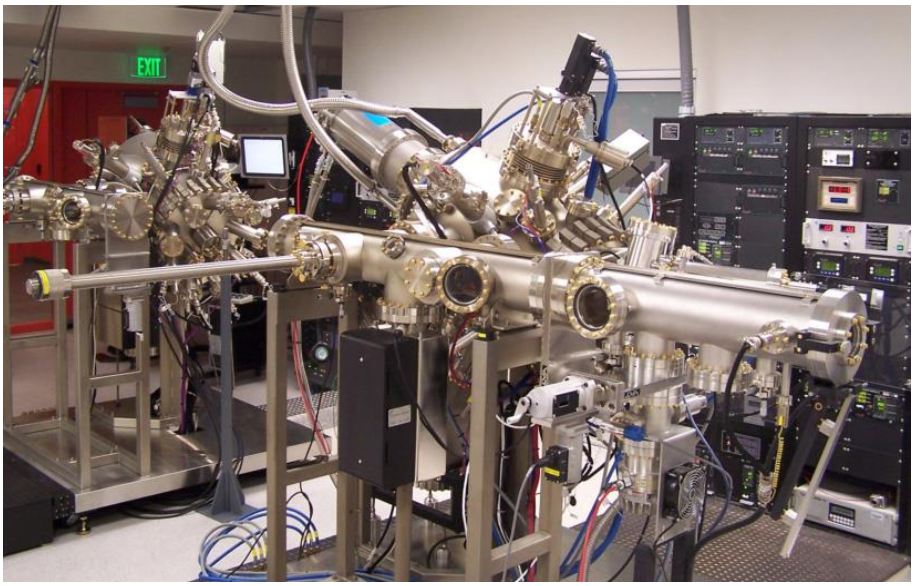

Figure C-1 The Veeco Gen930 solid-source MBE reactor for III-V materials at UCLA.

the shutter sequences are shown in Fig. C-2. The substrate temperature was monitored by an optical pyrometer and calibrated by the change in the surface reconstruction of GaSb from (1×3) to (1×5) using reflection high-energy electron diffraction (RHEED) equipped with the MBE reactor.

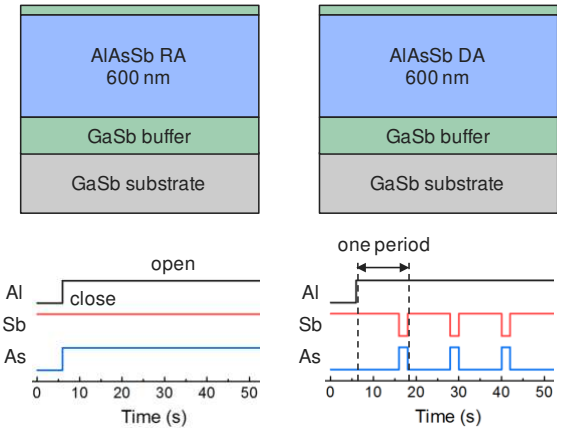

Figure C-2 The AlAsSb DA and RA sample structures with the corresponding shutter sequence of Al, As, and Sb sources.

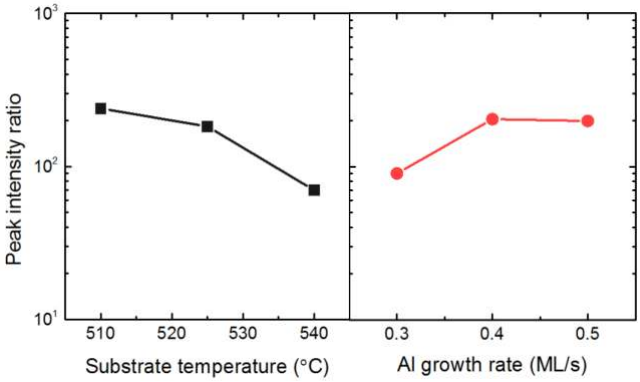

Figure C-3 PL intensity ratio of the E^X peak to the DL peak emissions under different growth conditions for the AlAsSb DA and RA samples.

The growth condition of the AlAsSb DA has been developed and evaluated using low-temperature photoluminescence (PL) measurement. All samples show similar features in the PL spectra as discussed in chapter 5. The optical quality of the material is judged by the PL intensity ratio of the E^X peak to the DL peak emissions, as shown in Fig. C-3, and the sample with a greater difference between two peaks suggests a lower density of deep level states. It is shown that the intensity ratio tends to increase with decreasing temperature and increasing growth rate, and the sample with the growth temperature of 510ºC at the growth rate of 0.4 ML/s gives the optimum material quality.